ABSTRACT

Title of Dissertation: THE TURBULENT BOUNDARY LAYER ON A SMALL DIAMETER FLEXIBLE CYLINDER IN THE WAKE OF A STREAMLINED TOWING APPARATUS

Deborah Ann Furey, Doctor of Philosophy, 2005

Dissertation directed by: Professor James Duncan
Department of Mechanical Engineering

Long thin flexible cylinders instrumented with acoustic sensors are used by the Navy for surveillance and detection. Acoustic transducers are mounted in a long linear array surrounded by an insulated jacketing material resulting in a long flexible array of sensors with a smooth outer surface. These cylinders, called towed arrays, are towed behind ships and submarines. As a result of the towing speed, a turbulent boundary layer develops along the outer boundary of the flexible cylinder which generates noise in the near field. Flow noise is critical to the measured acoustic signatures and therefore, to system performance. By understanding the nature of turbulent boundary layers on long, thin flexible cylinders, the performance of towed acoustic sensors used for surveillance and tactical operations can be improved.

Towed array detection performance is a function of several factors including ambient acoustics, array gain, flow noise, and signal processing. To advance existing systems, the primary goal is to increase the system gain by introducing longer apertures, i.e. longer arrays. Longer arrays of conventional design lead to additional stowage

requirements that are difficult to implement. The development of very small diameter towed array technology is required. Therefore, the results of this research will directly contribute to the work being done on small diameter arrays and multi-line array systems.

This is an experimental study to evaluate the development of the boundary layer thickness, δ, and momentum thickness, θ, along long thin flexible cylinders ($L/a=1.5*10^5$ and $3.0*10^5$ where $\delta/a>>1$, a=radius). The experiments use conventional test methods in conjunction with Stereo Particle Image Velocimetry (SPIV) measurement techniques to evaluate the flow in the boundary region of a small diameter flexible cylinder towed in the high speed towing basin at the Naval Surface Warfare Center Carderock Division (NSWCCD). The flexible cylinders are approximately neutrally buoyant and have an initial length of 152 m and radii of 0.45 mm and 1.25 mm. The first objective for this experiment is to evaluate the streamwise development of wall shear stress (τ_w) and momentum thickness (θ) in axisymmetric turbulent boundary layers using drag measurements at 3.1, 5.2, 9.3 and 14.4 m/s for comparison to existing data. The second and primary objective for this experiment is to determine the streamwise development of the axisymmetric boundary layer flow and to evaluate relevant boundary layer parameters at 3.8, 7.7, 12.9 and 15.4 m/sec using SPIV images acquired over the entire length of the cylinders. Drag measurements reveal that the wall shear stress is large and that the momentum thickness grows slowly when compared to flat plate boundary layers. The velocity field data shows that the boundary flow remains turbulent over the entire length of the flexible cylinder and that the turbulent profile is different from that of flat plate boundary layers.

THE TURBULENT BOUNDARY LAYER
ON A SMALL DIAMETER FLEXIBLE CYLINDER
IN THE WAKE OF
A STREAMLINED TOWING APPARATUS

By

Deborah Ann Furey

Dissertation submitted to the Faculty of the Graduate School of the
University of Maryland, College Park in partial fulfillment
of the requirements for the degree of
Doctor of Philosophy
2005

Advisory Committee:

Professor James Duncan, Chair
Professor John Anderson
Dr. Paisan Atsavapranee
Dr. Kimberly Cipolla
Professor Ken Kiger
Professor James Wallace

Dedicated to:

My friends. You have given so much… and I can't begin to thank you for what you have brought to my life.
My family. You have been my strength and my sanity … and I am grateful for your love, support and unending understanding through 'it all'
And especially my father. You have been my inspiration…and I miss you every day.

Requiem for Valentines Day

Waves ever rise, reminding me
How brief was the time that went on
Since I realized what was meant to be
My very first hero is gone.

Memories of problems, so long ago,
Wane with the tide of his storm.
With him went an important part of me
That's the part that kept me warm.

Days, months, years, please let my heart
Heal itself as hearts can give,
That I should find there, instead of a hole,
A place he always will live.

Written By   D. Walker

Acknowledgements

Where to begin.

First and foremost, I would like to thank my advisor Dr. Jim Duncan. Jim, you have the patience of a saint (12 years!). You have continued to support me over so many changes in my life and I can't begin to tell you how much I appreciate all of your commitment, time, guidance and, of course, your phenomenal editing abilities!!! You always had the ability to make things clear to me, when I felt like things just didn't make sense. I am so lucky to have been your student.

Dr. Kim 'Kimba' Cipolla, I know this project never would have happened without you. You have been an extraordinary support, friend and advisor and I hope that we continue to do great projects together.

Dr. Paisan "Pie' Atsavapranee, can I please know ½ of what you know? I can't begin to tell you how much your guidance and teaching has meant to me. You are a great friend and I hope we get to do many more cool measurements!!

I would like to thank the other members of my committee, Dr. John Anderson, Dr. Ken Kiger and Dr. Jim Wallace for their insights and suggestions in this very very cool project.

I would like to thank NSWCCD and so many people there. Bruce Webster and the support of the Extended Term Training program, I never would have been able to find the time. Dr. John Barkyoumb, this project would not have been possible without the support of the ILIR program. Bob Pellegrini, his expertise provided us the 'lift' that we needed. Dimitri Govotsos, his driving skills consistently got us that …last…20…feet! Dave Newborn, for all the help with Matlab (syntax!!). And all the 'Toads', always supportive and interested.

I would also like to thank NUWC and the support from there. Dick Phillips and the continued support from the ILIR program from Newport. Dr. Bill Keith, he was always available and helping me with various pressure spectra 'issues', regardless of the fact that I'm sure he would prefer to be out having a beer… Dave Hart…the mix master!

I would like to thank my mother, my sisters and my brother, for all their support and encouragement through the years.

Last, but definitely not least, Al Morisato. I want to thank you for your patience and tolerance…and your willingness to have 'take out' more nights than any of us cared to. I never would have been able to do this without your love and your understanding of my …not so understandable self.

Table of Contents

List of Tables

List of Figures

List of Symbols

a	Cylinder radius
a^+	Frictional Reynolds number $a^+ = \frac{au_\tau}{\upsilon}$
Re_a	Reynolds number based on radius $\mathrm{Re}_a = \frac{aU_\infty}{\upsilon}$
d	cylinder diameter
δ	Boundary layer thickness
δ^*	Displacement thickness
δ^T	Turbulent thickness
Re_θ	Reynolds number based on momentum thickness $\mathrm{Re}_\theta = \frac{\theta U_\infty}{\upsilon}$
θ	Momentum thickness
X,Y	Coordinates of cylinder located the Field of View data plane, transverse to the towing direction
y	Distance from the boundary
u^+	$u^+ = \frac{u}{u_\tau}$
y^+	$y^+ = \frac{yu_\tau}{\upsilon}$
τ	Shear
τ_w	Shear on the wall
r	Radial coordinate
ρ, ρ_f, ρ_p	Density, Density of fluid, Density of particle

k	von Karmon constant, 0.418
U_{∞}, U_o	Free stream velocity, towing velocity
u_τ	$u_\tau = \sqrt{\frac{\tau_w}{\rho}}$; Friction velocity.
u’	Fluctuation velocity
ū	mean velocity
U	instantaneous velocity, U=ū+u’
υ	Kinematic viscosity
A_s	$A_s = 2\pi a L$; Surface area of cylinder
D	Drag
C_d	Tangential Drag coefficient, $C_d = \dfrac{D}{\frac{1}{2}\rho U_\infty^2 A_s}$
l	Half width of wake
L	Cylinder length
l^+	$l^+ = \nu/u_\tau$, viscous length A
$\phi(\omega)$	pressure amplitude
ω	frequency
μ	viscosity
Λ	macroscale for turbulent boundary layer
λ	microscale for turbulent boundary layer
f(r)	Correlation function
s	distance cylinder moves in field of view

s^+	nondimensional distance s/l^+

CHAPTER 1: INTRODUCTION

Boundary layer flows have been studied extensively over the past 100 years. The mean and fluctuating stresses that these flows impart to the bounding surface are of great practical importance. The majority of this research has addressed flat plate boundary layers More recently attention has been given to boundary layers in axial flow over bodies with transverse curvature. Examples of this geometry include missiles, torpedoes ship hulls and towed arrays of sonar sensors.

A towed array is a long flexible cylindrically shaped acoustic device used by Navy vessels. These arrays are typically hundreds of feet in length, 2-6 inches in diameter, and are deployed trailing behind a towing vessel. Navy towed array systems require extensive handling hardware to accommodate the required linear array footage as well as complicated towing configurations. Figure 1 illustrates the elements in a towed array system for a submarine. There are several components internal to the submarine which do not effect the hydrodynamics of the array itself. The external elements include the towpoint, the towcable, and the array itself. The towpoint is the shipside forward most attachment point. A towcable, also called a leaderline, is used to separate the array spatially from the towing vessel. This separation ensures that the sonar system does not pick up noise from the ship's propellers or onboard machinery. The array contains vibration isolation modules, sensing modules and drogue modules. All modules have the same diameter and external character to ensure that the array is uniform and hydrodynamically smooth along the entire length.

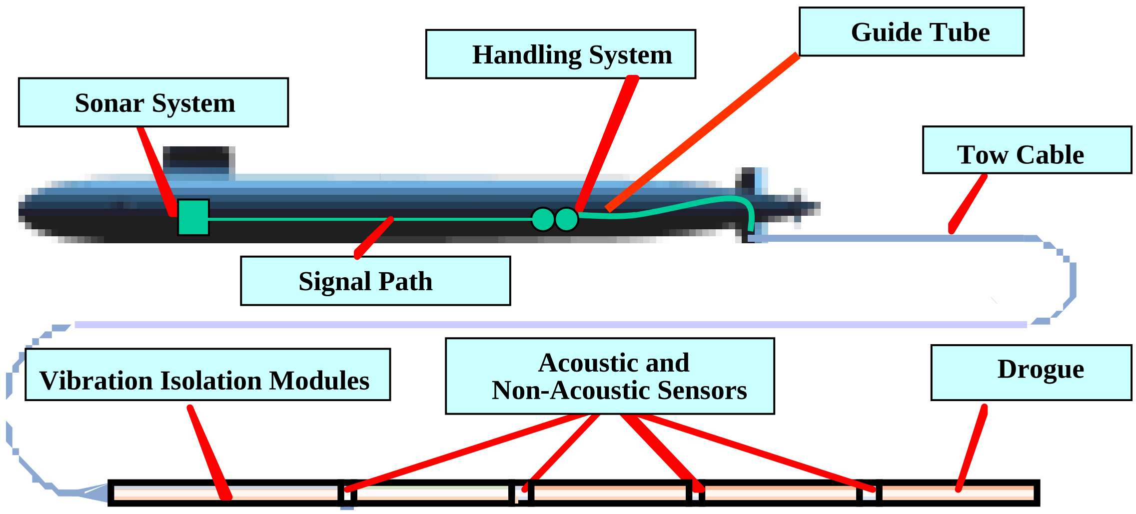

Figure 1: Navy Towed Array System. A Navy towed array system is comprised of several components, internal and external to the ship or submarine. The external components include the mechanical and electrical hardware to sense and deliver acoustic signals to the sonar system. This includes the towpoint to attach the tow cable to the towing vessel, the vibration isolation modules, the sensor modules, and the drogue.

A handling system, or winching system (see Figure 2), is required for paying out the array through hull penetrations and to monitor payout loads to ensure no damage is done to the equipment. When operating, the towed array data is transmitted through the electro-mechanical connectors back to the onboard processing units. The resulting acoustic signals detected by the towed array are analyzed for identification and localization of potential targets and threats.

Figure 2: Array handling system. An electronically controlled winch is used for paying out Navy towed array systems.

Acoustic array performance is influenced by several factors including ambient noise, array gain, flow noise, and signal processing. Improvements in performance can be achieved through signal processing advancements as well as the implementation of systems with higher array gain. Higher array gain can be achieved through longer arrays (longer aperture) or through volumetric configurations (several parallel arrays). Both implementations require more linear feet of acoustic array. In either case, using conventional arrays requires additional stowage volume which is difficult and sometimes impossible to obtain. Therefore, the development of very small diameter towed arrays is essential. Microfilament optical fiber towed arrays are being developed with diameters less than 2.54 cm (1 in) and aspect ratios on the order of 12,000 and longer to achieve improved system performance.

Given that acoustic arrays sense pressure variations in the ocean, the inherent pressure fluctuations in a turbulent boundary layer flow can have a significant adverse impact on system performance. The characterization of pressure fluctuations in a boundary layer flow is necessary to determine the contribution of the turbulent flow to the measured acoustic signal. Near-wall pressure spectra are frequently reported in terms of the localized boundary layer parameters. Inner and outer scaling laws have been investigated (see

Figure 3 Keith et. al. 1992) in efforts to determine the dominant flow characteristics influencing the noise generation. Thus, by understanding the nature of turbulent boundary layers the operation of these acoustic sensors can be improved.

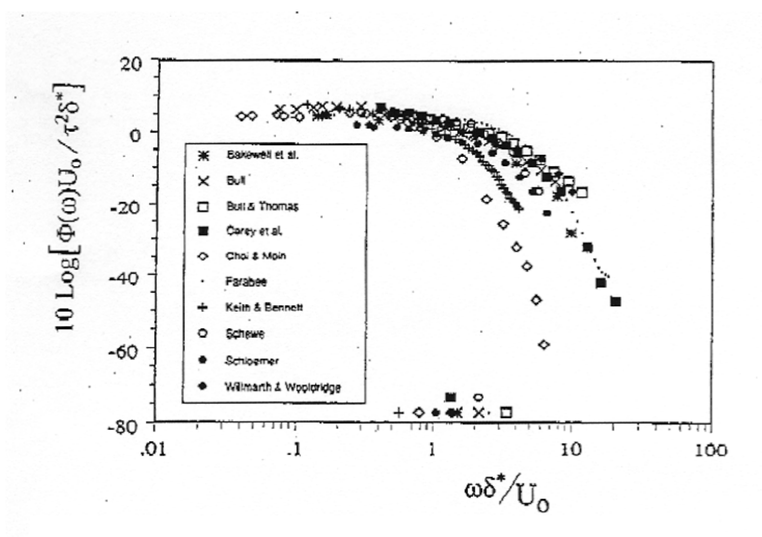

Figure 3: Non-dimensionalized near wall pressure spectra in flat plate boundary layers and pipes. Near wall pressure spectra can be non-dimensionalized with inner, outer or mixed boundary layer parameters. Reprinted from Keith et. al. 1992 (27).

Axisymmetric boundary layer flow deviates from the flat plate solution for cases where the boundary layer thickness is on the order of or larger than the radius of the cylinder. Consider a flat plate of length L and width w and a small-diameter cylinder of length L and diameter 2a. The ratio of the boundary flow volume, V_w, to bounding surface area, A_s, for the flat plate, is:

$$\frac{V_e}{A_s} = \frac{Lw\delta}{Lw} = \delta$$

Equation 1

where δ is the boundary layer thickness at the downstream location L. This ratio reduces to a value equivalent to the boundary layer thickness, δ. For a cylindrical boundary layer, this ratio can be expressed (refer to Figure 4):

$$\frac{V_e}{A_s} = \frac{L\pi\left[(\delta + a)^2 - a^2\right]}{L\pi 2a} = \delta(1 + \frac{\delta}{2a})$$

Equation 2

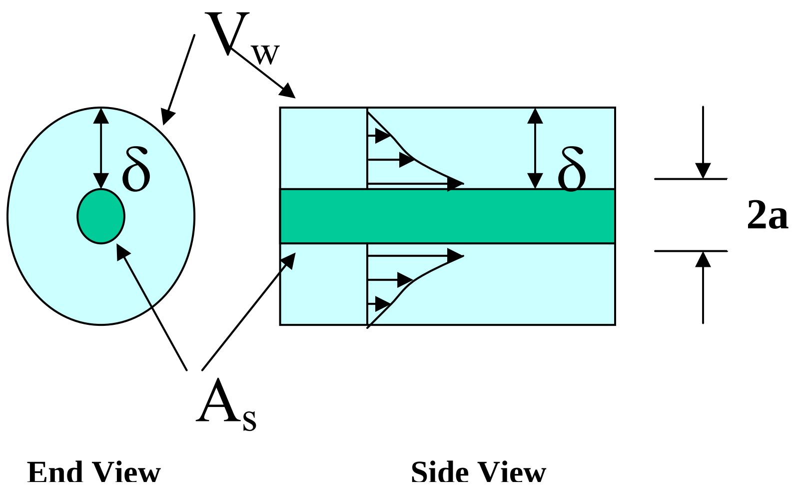

Figure 4: Schematic of boundary layer geometry for towed cylinder.

This ratio reduces to the boundary layer thickness plus a term equivalent to the boundary layer thickness multiplied by the thickness ratio δ/2a, the boundary layer thickness to diameter ratio. For cases where δ/a>>1, the volume to area ratio for the cylindrical boundary layer is substantially larger than that for the flat plate.

This thesis will investigate the turbulent boundary layer development along high-aspect-ratio flexible cylinders ($L/a= 1.5*10^5$ and $3*10^5$) being towed behind a vertical strut. Boundary flow measurements in this range of aspect ratio have never been performed on flexible cylinders.

The remainder of this thesis is divided into nine chapters. Chapter 2 reviews previous research on thick axisymmetric boundary layers on rigid cylinders and boundary layers on high-aspect-ratio flexible cylinders. Chapter 3 describes the experimental design, hardware and techniques used in this study. Measurements of the drag on the models are presented in Chapter 4. Fluid velocity fields are measured with a Stereo Particle Image Velocimetry (SPIV) technique which is described in Chapter 5 . Measurements of the mean and fluctuating components of the boundary layer flow are present in Chapters 6 and 7, respectively. The analysis and characterization of the transverse motion of the flexible cylindrical models are presented in Section 8 and a discussion of preliminary modeling of the experimental data is given in Chapter 9. Lastly, the conclusions and future work are discussed in Chapter 10. Also note, throughout this thesis, the flexible cylindrical models will be referred to simply as a cylinder or a filament.

CHAPTER 2: REVIEW OF PREVIOUS WORK

Initial boundary layer research largely concentrated on investigating the development of two-dimensional rigid planar turbulent boundary layers. However, while the axisymmetric boundary layer on a rigid cylinder is also two dimensional, it is more complicated due to the additional effect of the transverse curvature of the surface. Experiments have been designed to determine the relevant parameters for scaling this flow. However, the range of flow parameters interrogated in these experiments is limited and thereby limits the physical model and scaling laws that can be formulated based on experimental data. To date, there is no model that has been developed to include the practical range of transverse curvatures found in naval engineering practice.

Experiments designed to investigate the effects of transverse curvature on the development of turbulent boundary layers are constrained by the test facility and apparatus being used. Therefore, each investigation interrogates only a finite range of Reynolds numbers and boundary layer thickness ratios. Over all of these studies,on rigid cylinders, values of $Re_a=U_\infty a/\nu$ between 100 and 10^6 and δ/a between 0.1 and 100 have been examined. The boundary layers on flexible cylinders have also been examined, but less extensively.

2.1 Boundary Layers on Fixed Cylinders

2.1.1 Mean Velocity Profiles

Velocity profiles have been measured for a wide range of cylinder diameters at low to moderate Reynolds numbers ($Re_\theta \approx 10^3$). Mean velocity profiles in turbulent cylindrical boundary layers have been compared to the well known two-dimensional flat-plate boundary layer profiles. Results for boundary layer profiles with mild curvature do not differ dramatically from the flat plate results. However, as is discussed below, as the transverse curvature increases, results begin to show departure from the planar results.

For all published cases with transverse curvature, velocity measurements in the inner portion of the viscous sublayer of the turbulent boundary layer have been shown to follow the classic form, i.e. scale linearly with distance from the boundary [4,14] as in the flat plate case:

$$u^+ = y^+$$

Equation 3

where u^+ is the local mean velocity divided by the wall shear velocity, $\bar{u}/u_\tau$, and y^+ is the distance from the boundary multiplied by the shear velocity and divided by the kinematic viscosity, ($y\, u_\tau/\nu$). In other words, near the wall, the boundary layer does not feel the curvature and the boundary "looks like" a flat plate. The extent of the linear region depends on the transverse curvature. For mild curvature ($\delta/a<1$) the linear region extends out to y^+ values of 5 to 10 [14]. As curvature increases, the extent of the linear portion decreases. Rao [1] offers an alternate expression for the flow very close to the wall. Assuming no pressure gradient, small streamwise gradients and small radial velocities, a cylindrical control volume of radius r centered on the cylinder results in the following shear balance expression [1,12] :

$$\tau r = \tau_w a$$

Equation 4

where τ is the shear stress on the outer surface of the control volume. From this shear balance and using substitution and integration, Rao [1] develops the following expression which scales with both cylinder radius and the wall shear:

$$u^+ = a^+ \ln\left(\frac{r}{a}\right) \quad where \quad r = y + a$$

Equation 5

This expression reduces to the linear relationship $u^+=y^+$ when a is large. Rao's data suggest that as the surface curvature becomes more severe, viscous effects penetrate further into the flow than for the 2-dimensional flat plate case. Several experiments [1,3,5,11] have shown that for cases where $\delta/a>1$, u^+ scales with a dependence on the cylinder radius and distance from the boundary in the viscous layer, as suggested in Equation 5.

Outside the inner viscous sublayer but still in the inner region, the measurements indicate that the influence of the wall is still important. However, in this region the turbulent shear dominates and the profile follows a logarithmic relationship. Results [12] show that for values of $\delta/a<1$, the boundary layer profile follows the 2-dimensional law of the wall in this region. For values of $\delta/a>1$, the inner viscous sublayer region generally is extended, the log region falls below the 2-d profile and the outer region becomes wake-like when plotting u^+ against y^+ [5,11,12]. As the curvature increases, the transition between the inner layer and the wake like outer flow occurs at a smaller y^+. It is expected that for δ/a>>1 (very long cylinders), the profile would depart from the law of the wall even in the inner sublayer as a^+ approaches 1.

In the logarithmic and outer regions, data for various values of parameters do not collapse using classic variables u+ and y+. In addition, results to date do not reveal clear trends with δ/a, due to relatively small variations in the value of this parameter in published experiments. However, Youssef et. al found that within a limited range of δ/a (0.67-1.84), changes in Re_θ have a significant effect on the mean velocity profile. Lueptow et. al. [11] obtained data for larger values of δ/a (13.4-34.5) by varying the streamwise measurement location. A general trend of decreasing slope of the log region with increasing δ/a was observed. Willmarth et. al. [5] reported a similar trend from measurements in which δ/a was varied from 1.8 to 37.5 by changing the cylinder diameter. For $\delta/a \geq 16$ and $4.4\times10^3 \leq Re_\theta \leq 10^4$, the slope of the log region decreased as δ/a increased. The departure from the flat plate profile led Lueptow et al. to propose a mixed scaling log law:

$$u^+ = \frac{1}{m}\ln y^+ + n$$

Equation 6

where m and n are functions of δ/a.

From the characteristics of the streamwise boundary layer development, there is evidence that even the outer flow is affected by the transverse curvature of the boundary [12]. For cylindrical boundary layers, the outer portion of the boundary layer becomes fuller than the 2-D case with the effect increasing with increasing δ/a [5,12]. The mean velocity distribution in this region can be expressed in terms of a velocity defect scaled with the friction velocity and incorporating a transverse curvature parameter as shown:

$$\frac{U_o - \overline{u}}{u_\tau} = f\left(\frac{y}{\delta(x)}, \frac{\delta}{a}\right)$$

Equation 7

However, the defect law is not universal and likely depends on the parameters δ/a and a+ [4].

The effect of leading edge geometry and cylinder alignment on mean flow quantities was investigated. Tests conducted on cylinders with different leading edge shapes, one ogive nose and one spherical, show that for values of x/a > 5000 the boundary layer becomes independent of upstream conditions and therefore independent of the leading edge geometry [10]. Other experiments investigated the effect of cylinder alignment with respect to the freestream velocity to quantify the effect of asymmetry on the development of the boundary layer along long thin cylinders [6, 9, 34]. The results showed that for yaw angles larger than 5 degrees, vortical structures are shed from the cylinder. The boundary layer for the yaw condition below 5 degrees can be considered primarily an axial boundary layer flow with increased surface shear due to cross flow components [6, 9, 34]. Therefore, the implication for long flexible thin cylinders is that provided the local angle of attack remains within the range of 0 to 5 degrees the boundary flow develops primarily in an axial manner.

Lastly, studies investigated the question of relaminarization [2]. The velocity profile for a boundary layer with a favorable pressure gradient and the boundary layer with transverse curvature effects both result in fuller velocity profiles and a reduction in turbulence intensities. It was suggested that since the favorable pressure gradient causes the turbulent boundary layer to relaminarize that the effect of transverse curvature would also cause relaminarization. The relationship of wall shear to the boundary layer development suggested that relaminarization would occur for thick boundary layers with values of Re_a less than 15000 and small values of a+ [1, 3]. However, as stated by Willmarth [6], the fuller profiles are caused by different phenomena in the two cases. The fuller profile is caused by the acceleration of the outer flow for the favorable pressure gradient condition and is caused by surface geometry for the case with transverse curvature. Further, data for large δ/a and small a^+ show no evidence that the boundary layer relaminarized for any test conditions [3, 5, 6, 10].

Overall, previous investigations have shown that the transverse curvature of a boundary significantly affects the development of the adjacent boundary layer flow. The magnitude of the curvature and the relative thickness of the boundary layer determine the extent of effects on the profile. These effects include a deviation from the 2-dimensional planar profile in the log region, fuller velocity profiles and an increase in friction coefficient with decreasing cylinder radius. Little data has been published showing how the boundary layer changes as a function of axial location for thick axisymmetric boundary layers. This type of data would provide local parameter changes in a^+ and δ/a independent of Re_a. Therefore, the explicit relationship between the transverse length scale and the velocity profile is not yet known.

2.1.2 Turbulent Quantities

Measurements evaluating the unsteady velocities in the thick axisymetric boundary layers provide information about the composition of the profiles in terms of the turbulence generation and the structure and motion of turbulent eddies. However, in cases with transverse curvature only limited measurements exist.

Velocity fluctuation profiles indicate how turbulent energy is distributed throughout the boundary layer. The outer edge of the turbulent region is indicated by the onset of intermittency in the velocity measurements. For $\delta/a=7$, intermittency has been measured to occur at $\frac{y}{\delta}=1.0$ for the cylindrical case where it occurs at $\frac{y}{\delta}=0.8$ for the planar case [11]. This suggests that the motion of eddies in the turbulent region is less influenced by the boundary in the cylindrical geometry. Also, the location in the profile where the maximum streamwise velocity fluctuation occurs is a significant characteristic for turbulent boundary layers. For a flat plate turbulent boundary layer, the maximum streamwise velocity fluctuation occurs at a y^+ of about 15. For profiles with mild transverse curvature, measurements show that the maximum streamwise velocity fluctuations occur at a y+ value of 11 to 15, slightly closer to the boundary than the flat plate [12]. Data shows that for increasing transverse curvature, the location of the maximum velocity fluctuation moves closer to the wall. This peak location corresponds closely to the maximum in turbulent kinetic energy occurring in the profile. Also, the Reynolds stress and turbulence production is enhanced in this region due to the large turbulent velocities. Further outside the peak, the Reynolds stress is found to drop off with increasing distance from the boundary more quickly than the flat plate case [4,11]. This is attributed to the cylindrical geometry of the boundary layer region. Considering the shear moment balance discussed previously (Equation 4), there is a geometric influence on Reynolds stress near the wall [11]:

$$\mu \frac{\partial \overline{u}}{\partial r} - \rho \overline{uv} = \tau_w \frac{a}{r}$$

Equation 8

For δ/a≈O(1), Reynolds stress $\frac{\overline{uv}}{u'v'} \approx 0.5$ throughout most of the boundary layer except near the wall and at the outer edge. These measurements show that the distribution of turbulent energy through a turbulent boundary layer is affected when the boundary has significant transverse curvature (δ/a>2), though the parameter range covered by published data is limited [11, 12, 14].

For the very long small diameter cylinders where δ/a>>1, the filament has been referred to as “a small vorticity and turbulence producing disturbance”[12]. As the transverse curvature increases, the boundary layer profiles become full, and the wall shear and friction coefficient become large compared to the flat plate equivalent. The increased wall shear relative to a flat plate boundary layer indicates that the cylinder is more effective in converting mean flow kinetic energy into turbulent kinetic energy. Also, the production of turbulent energy is a result of extracting energy from the mean flow through the axial gradients and resulting Reynolds stresses [12].

The mechanics of turbulence generation is believed to be similar for all wall bounded flows. However, for cases with transverse curvature, the data suggests that the outer flow affects the generation of turbulence more strongly [12,14]. Because the boundary layer is thick, ($\frac{\delta}{a}$ is large) turbulent eddies are considerably larger than the cylinder diameter and they are no longer bounded by the wall geometry. Therefore, eddies are free to move from one side of the filament to the other with virtually no wall constraint. These unconstrained motions of the turbulent structures cause an increase in Reynolds stress production and wall shear due to the interaction of the eddy with the cylinder. Also, this effectively allows the distribution of turbulence to extend further into the boundary layer and establishes a rationalization for intermittency occurring further from the boundary. Therefore, this behavior causes the transport of the turbulent kinetic energy and the kinematics of the eddies to be significantly different from flat plate boundary layers.

Eddies occurring in thick cylindrical boundary layers are smaller in the transverse (azimuthal) direction when compared to those in a flat-plate boundary layer due to the finite transverse dimension but can be large compared to the diameter of the cylinder [5,14]. The reduced surface area relative to the eddy sizes causes a reduction in pressure strain transfer to radial and azimuthal normal stresses. [12, 14, 15].

Burst detection measurements in cylindrical boundary layers show results similar to planar turbulent boundary layers [5, 6, 11, 12]. The periodic occurrence of bursts is from the motion of the large eddies passing over the sublayer in both cylindrical and flat plate boundary layers. However, the scale of turbulence at a given distance from the wall in the cylindrical case is reduced due to the fullness of the profiles increasing the convection speed of the structures close to the boundary. This suggests that the mechanism for generating turbulence is similar for all wall bounded flows while the transport and production is dependent on flow geometry [5,6,11,12].

For turbulent boundary layers with transverse curvature effects, the turbulent region extends further into the flow when compared to the 2-dimensional flat plate case, eddies move relative to the surface enhancing surface friction, the turbulence intensity increases with reduced cylinder diameter, and burst detection results indicate the mechanism for turbulence generation is similar for all wall bounded flows.

2.1.3 Theoretical and Numerical Models

Models developed for cylindrical turbulent boundary layer profiles assume similarity with flat plate boundary layers and incorporate parameters to include transverse curvature effects. The innermost region of the viscous layer is linear, as discussed previously. At distances further from the boundary for cases with transverse curvature, the profiles take on different forms and incorporate different parameters.

A Law of the Wall for axisymmetric turbulent boundary layers developed by Rao [1] for Re_a = 90 to 15000 incorporates the transverse curvature length scale (Equation 9).

$$\frac{\overline{u}}{u_\tau} = \frac{u_\tau a}{\upsilon} \log\left(1 + \frac{y}{a}\right)$$

Equation 9

This result suggests that the axisymmetric turbulent boundary layer exhibits the same fundamental characteristics as a planar boundary layer when scaled using the radius and friction Reynolds number for cases of mild curvature.

Another logarithmic formulation was developed by Patel using a mixing length model for Re_a values of 100 to 130000 [2]. The model relates the Reynolds stress as influenced by the wall curvature to the local mean velocity. The resulting formulation (Equation 10) is similar to the 2-D law of the wall formulation which incorporates the frictional Reynolds number, a^+.

$$u^+ = \frac{1}{k}\ln(4a^+ \frac{((1+\frac{y^+}{a^+})^{\frac{1}{2}} - 1)}{((1+\frac{y^+}{a^+})^{\frac{1}{2}} + 1)}) + B(a^+)$$

Equation 10

Alternatively, a logarithmic mixing length model was developed by Denli et. al. [7] for thick axisymmetric turbulent boundary layers on long cylinders (δ/a=9 to 16 and L/a=1700 to 3500) that incorporates the frictional Reynolds number a^+ and the transverse curvature term:

$$u^+ = A\ln\left(a^+\sqrt{\frac{r}{a}}\ln\left(\frac{r}{a}\right)\right) + B(a^+)$$

Equation 11

This expression for the profile results in a log region which extends to larger values of y^+ as a^+ increases and with the wake portion of the boundary layer increasing as δ/a becomes larger. This result was shown to agree well with experimental data [17] and indicates that the radius of curvature is a relevant inner parameter

The outer layer, as mentioned, follows the wake defect law. For cases with mild curvature a relationship which includes both inner and outer scaling parameters was developed by Yu as shown;

$$\frac{U_o - \bar{u}}{u_\tau} = C\,\ln\left(\frac{y}{L}\right) + D$$

Equation 12

For cases with more severe transverse curvature, the outer layer defect law is considered to require several other parameters.

$$\frac{U_o - \bar{u}}{u_\tau} = f\left(\frac{x}{a}, \frac{y}{\delta}, \mathrm{Re}_a\right)$$

However, additional data is necessary to further develop the outer region velocity defect law.

Direct Numerical Simulations by Neves et. al. investigating the effects of transverse curvature (5<δ/a<11) on wall bounded turbulent flows agreed with the findings for the near wall region from the collected data [13]. DNS results show that, as the curvature of the boundary increases, skin friction increases and the slope of the log region decreases. In addition, the results show that the turbulence is more anisotropic than planar flow with a large percentage of the turbulent kinetic energy in the streamwise velocity fluctuations.

Models of the turbulent boundary layer with transverse curvature effects suggest that the regions in the flow are effected by both inner and outer flow parameters. Low Reynolds number DNS results show similar trends with experimental data but a general model that satisfies a large range of parameters is still undeveloped.

2.2 Boundary Layers on Towed Cylinders

2.2.1 Drag Measurements and Momentum Thickness Determination

Considerable work has been conducted by the Naval Undersea Warfare Center, NUWC, investigating the development of the boundary layer flow on small diameter flexible cylinders at moderate to high Reynolds numbers with applications to towed array performance. Cipolla et. al. [16, 17, 18] use a volumetric analysis to extract momentum thickness information from drag values spatially and temporally averaged over flexible cylinders where $L/a = 10^5$ and δ/a approaches values of 50 to 100. The analysis technique and the findings are detailed below because of their relevance and application in the present experiment.

The total drag was directly measured for several speeds on a flexible cylinder with $L/a=10^5$. The cylinder was incrementally reduced in length by Δx and the drag determined for each new cylinder length. The drag coefficient was calculated for each increment of length based on the following relationship.

$$C_{d\,i} = \frac{\Delta D_i}{\frac{1}{2}\rho U_\infty^2 A_s}$$

Equation 13

where A_s is the surface area of a cylinder of length Δx. The resultant data shows that the drag coefficient is on the order of 3 times larger for the cylindrical boundary layer than the equivalent flat plate conditions.

A volumetric analysis results in a deterministic expression for the momentum thickness based on the drag coefficient [17, 31]. A cylindrical control volume is defined that encloses the boundary layer flow around an axial cylinder but that excludes the cylinder itself (see Figure 5).

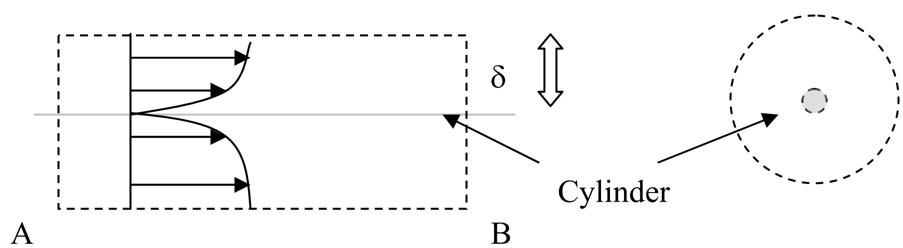

Figure 5: Control volume for an axisymmetric boundary layer analysis. The control volume for an axisymmetric boundary layer is defined by a cylindrical volume with an outer radius equivalent to the boundary layer thickness, δ, occurring at the end of the cylinder minus the volume of the inner cylinder itself.

There is a reduction in the mass flow rate and momentum flux through planes A and B of the control volume (shown in the above figure) as a result of the drag that the cylinder exerts on the flow. The drag on the inner surface of the control volume can be related to the wall shear and to the momentum loss in the flow using the following expression:

$$\frac{\tau_w}{\rho U_\infty^2} = \frac{1}{L}\int_a^{a+\delta} \frac{\overline{u}(r)}{U_\infty}\left(1 - \frac{\overline{u}(r)}{U_\infty}\right)\frac{r}{a}\, dr = \frac{1}{2}C_d$$

Equation 14

The resulting momentum thickness can also be related to a similar integral involving the velocity profile for a cylindrical boundary layer:

$$\theta^2 + 2a\theta = 2\int_a^{a+\delta} \frac{\overline{u}(r)}{U_\infty}\left(1 - \frac{\overline{u}(r)}{U_\infty}\right) r\, dr$$

Equation 15

Combining Equation 14 and Equation 15 results in the following expression between the drag coefficient and momentum thickness. [17]

$$\theta^2 + 2a\theta - aLC_d = 0$$

Equation 16

This relationship was used to evaluate the variation of momentum thickness over the length for cylinders where $L/a = 3.4*10^4$ to $3.4*10^5$ and $Re_\theta = 10^4$ to 10^5. The results show that for a fixed diameter cylinder and towing speed, the momentum thickness at the end of the cylinder increases with increasing length and that the momentum thickness in an axisymmetric boundary layer grows more slowly than that of a flat plate (See Figure 6).

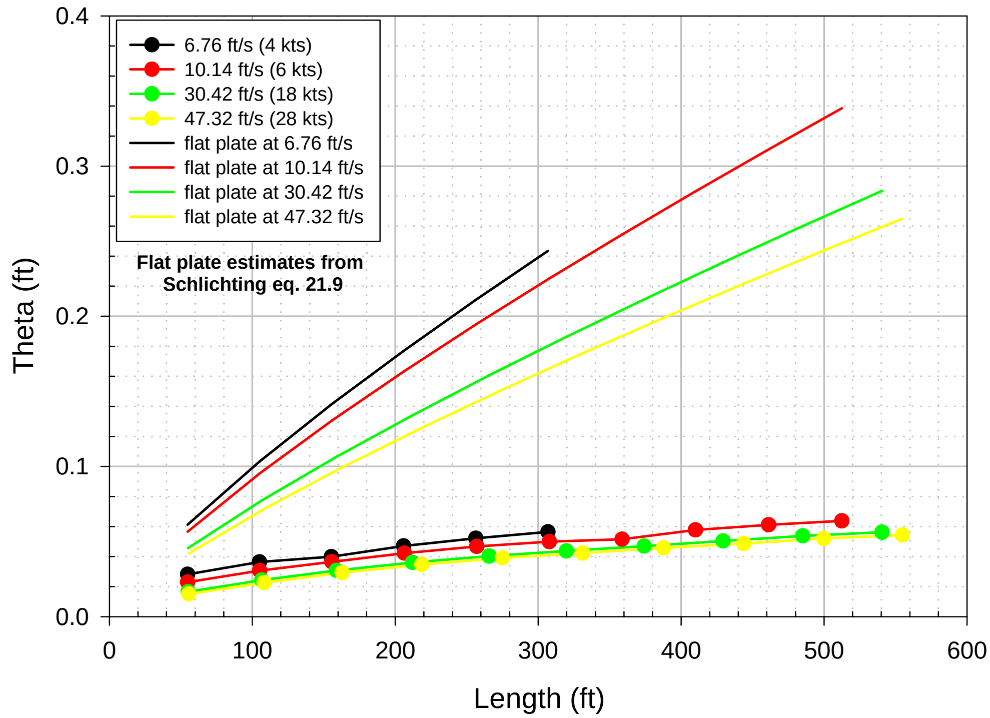

Figure 6: Momentum Thickness Measurements of thick Axisymmetric Boundary Layer versus Flat Plate Predictions. Reprinted from Cipolla et. al. 2002. The momentum thickness on thick axisymmetric boundary layers grows much more slowly than that on a flat plate.

Also, the drag measurements agree with previous findings showing there to be an increase in the coefficient of friction with an increase in transverse curvature. In addition, the findings supported the results from Luxton [10] stating that the upstream conditions become insignificant on the development of the boundary flow far downstream.

In conclusion, previous work shows that the transverse curvature of a boundary effects the development of turbulent boundary layers. However, for geometries and Reynolds numbers relevant to towed array operations, the data is limited in its application and illustrates the need for additional work to characterize boundary flow parameters for very thick boundary layers with particular relevance to acoustic modeling.

CHAPTER 3: EXPERIMENTAL DESCRIPTION AND PROCEDURE

The experiment was designed to make direct measurements of the total drag and the three-dimensional velocity distribution in the boundary layer of a flexible high-aspect-ratio cylinder in axial flow. Models with a length to radius ratio, $\frac{L}{a}$, of 150000 to 300000 were tested. The boundary layer thickness to radius ratio, $\frac{\delta}{a}$, and the momentum thickness Reynolds number, Re_θ, in these tests were expected to be on the order of 300 to 400 and 10^4 to 10^6, respectively.

In this chapter, the experimental details and procedures are presented in 5 subsections. The rationale for the experimental design will be discussed in Section 3.1. This is followed by a detailed description of the towing configuration and hardware in Section 3.2. In order to establish a reference for the effects of the towing hardware on the cylinder flow, a discussion of the wake development behind the towing strut is also included. In Section 3.3, the hardware used for the drag measurements and data acquisition will be described. The general SPIV technique as well as the resulting SPIV parameters for this experiment are described in Section 3.4. This is followed by a discussion of the relationship between the experimental design and the data analysis methods in Section 3.5. Lastly, the testing procedure is described in Section 3.6.

3.1 Experimental Design Considerations

The experiment is designed to reproduce the elements in the towed array system. The experiment includes the towpoint hardware, the leaderline to spatially separate the flexible cylinder from the towpoint, and the flexible cylinder to simulate the towed array. To achieve a relevant range of test parameters, a cylinder of 1 mm diameter must be on the order of 100 m in length. Considering these dimensions, this experiment required a test facility which would accommodate exceptionally long models. Therefore, the experiment was conducted in a towing tank.

A towing tank is a long stationary pool of water through which test models are towed by a carriage. The carriage rides along the top of the tank and operates along the full length. A streamlined towstrut is mounted to the carriage and test models are attached to a submerged towpoint located on the botton of the towstrut. First, the leaderline is secured to the towpoint to spatially separate the towpoint from the test model. The test cylinder is then attached to a snap swivel at the tail of the leaderline. The entire assembly is towed at different speeds through a stationary measurement plane. As with a real array, the cylinder is free to move in the flow field. This was taken into account in the design and selection of the measurement hardware as well as the data analysis procedures. The models diameters, lengths and speeds were chosen to be consistent with the experiments of Cipolla and Keith (2002). The resulting test matrix is shown in Table 1.

Table 1: Test Matrix

Diameter mm (in.)	Length m (ft)	Speed m/s (kts)	No. of Runs	Measurement
0.89 (0.04)	152 (500)	3.8 (7.5)	3	SPIV/DRAG
0.89 (0.04)	152 (500)	7.7 (15)	5	SPIV/DRAG
0.89 (0.04)	152 (500)	12.8 (25)	8	SPIV/DRAG
0.89 (0.04)	152 (500)	15.4 (30)	10	SPIV/DRAG
0.89 (0.04)	145 (475)	3,5,7,14.4 (6,10,14,28)	4	DRAG
0.89 (0.04)	130 (425)	3,5,7,14.4 (6,10,14,28)	4	DRAG
0.89 (0.04)	114 (375)	3,5,7,14.4 (6,10,14,28)	4	DRAG
0.89 (0.04)	99 (325)	3,5,7,14.4 (6,10,14,28)	4	DRAG
0.89 (0.04)	84 (275)	3,5,7,14.4 (6,10,14,28)	4	DRAG
0.89 (0.04)	69 (225)	3,5,7,14.4 (6,10,14,28)	4	DRAG
0.89 (0.04)	53 (175)	3,5,7,14.4 (6,10,14,28)	4	DRAG
0.89 (0.04)	38 (125)	3,5,7,14.4 (6,10,14,28)	4	DRAG
0.89 (0.04)	23 (75)	3,5,7,14.4 (6,10,14,28)	4	DRAG
2.5 (0.1)	152 (500)	3.8 (7.5)	3	SPIV/DRAG
2.5 (0.1)	152 (500)	7.7 (15)	5	SPIV/DRAG
2.5 (0.1)	152 (500)	12.8 (25)	8	SPIV/DRAG
2.5 (0.1)	122 (400)	3,5,7,14.4 (6,10,14,28)	4	DRAG
2.5 (0.1)	90 (300)	3,5,7,14.4 (6,10,14,28)	4	DRAG
2.5 (0.1)	61 (200)	3,5,7,14.4 (6,10,14,28)	4	DRAG
2.5 (0.1)	30 (100)	3,5,7,14.4 (6,10,14,28)	4	DRAG
TARE RUNS				
Strut Only	N/A	3.8, 7.7, 12.8, 14.4 (7.5, 15, 25, 30)	28	SPIV
Leader Line	15 (50)	3,5,7,14.4 (6,10,14,28)	4	DRAG
			126	**TOTAL RUNS**

The test setup was separated into two working areas; the towing carriage and the Stereo Particle Image Velocimetry (SPIV) measurement area. The carriage hardware included the towing strut, the cylinder models, and the drag measurement system. The SPIV hardware included the SPIV system, optical trigger, flow particle seeding system, hydraulic lift and climate control system. The following sections will discuss these systems in detail.

3.2 Towing Configuration and Towing Hardware

The tests were conducted in the high-speed basin at the David Taylor Model Basin in Bethesda, Maryland. The basin is rectangular in shape with a total length of 904 m (2968 feet), a width of 6.4 m (21 feet) and a depth of 4.9 m(16 feet). The high-speed carriage (Figure 7) is capable of speeds up to 25.7 m/s (50 knots) and operates with an accuracy of approximately 0.1% (refer to Appendix A). The carriage is a truss structure, electrically powered, and designed with an open central test bay for experimental set up. The carriage operates from West to East along the towing basin.

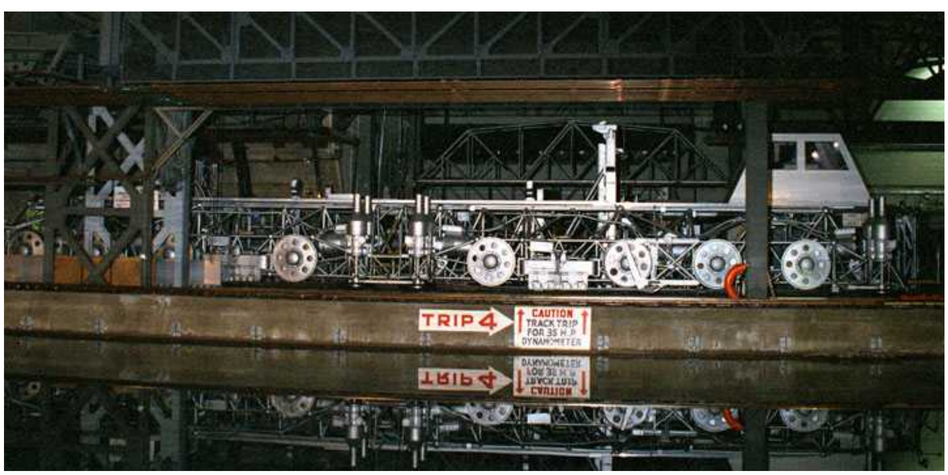

Figure 7: Towing Carriage 5. Carriage 5 is a steel truss type structure with large wheels that ride on top of the towing basin rails.

A 10-foot-long towing strut was mounted to a set of vertical rails located on the East end of the carriage test bay. The strut has a tapered ogive cross section and a wedge shaped towpoint. An overhead winch is used to move the strut up and down along the rails for positioning the towpoint depth. The strut was designed to withstand side loads up to 900 lbs and drag loads of up to 3000 lbs. This towing strut provided sufficient structural rigidity for the expected loads.

Drag loads on the cylinders were measured using a small cylinder-type load cell. The load cell was rigidly attached to the towpoint on the bottom of the tow strut. The wedge towpoint and drag cell were housed inside a fiberglass fairing (see Figure 8). The fairing provides protection from buffeting and residual loading on the cabling. A 15 m (50 ft) leader line was attached to the load cell. A snap swivel clip (Figure 9) was connected to the aft end of the leader and was followed by the cylinder model.

Figure 8: Towpoint with fairing. The towpoint is on the bottom of the towing strut. There is a through hole in the strut to allow for electrical cable to pass for the drag cell. The towpoint hardware is enclosed in the yellow fiberglass fairing.

Figure 9: Snap swivel. A snap swivel is a connecting device typically used on fishing equipment. The snap swivel has two rounded ends with a central ball and a snap connector on one end. It was used as the connector between the leaderline and the flexible cylinder.

The leader line is used to provide spatial separation between the towpoint and the model as is done in the Navy towed array units. The swivel clip is utilized in this configuration to act as a boundary layer trip to initiate new boundary layer growth at the upstream end of the model. Previous results (Cipolla, et. al. 2001, 2002, 2003) show that the upstream geometry of the towpoint does not change the measured drag results provided that the cylinder is sufficiently downstream of the initial towpoint and that a trip device is placed upstream between the leaderline and the cylinder model. Previous tests conducted with different towing configurations and boundary layer trip mechanisms produced like drag values on similar models and therefore supports the conclusion that the downstream boundary flow is comparable for the various towing configurations as well. Therefore, using a towing configuration with a trip mechanicsm would predicate that the drag and velocity measurements from this experiment can be compared to earlier works.

The flexible cylinders that were tested had diameters (2a) of 0.89-mm and 2-mm with initial lengths of 152 m (500 feet) corresponding to L/a values of 3.4×10^5 and 1.2×10^5, respectively. The cylinder models were held under tension for a week prior to testing to ensure there was no memory of bends or kinks present in the cables. The cylinders were towed along the centerline of the basin at a depth of more than 1000 diameters to ensure minimal tank wall and free surface effects on the boundary layer development. The 0.89-mm cylinder was a nylon STREN® saltwater monofilament fishing line (80 lb test). The 2-mm cylinder was a Naval Undersea Warfare Center (NUWC) fiber-optic cable with a polyurethane jacket, Kevlar lining and fiber-optic core. Both lines were considered hydrodynamically smooth. The flexible cylinders were towed down the basin through the measurement volume of the SPIV system. The towing assembly is shown in Figure 10 and 11.

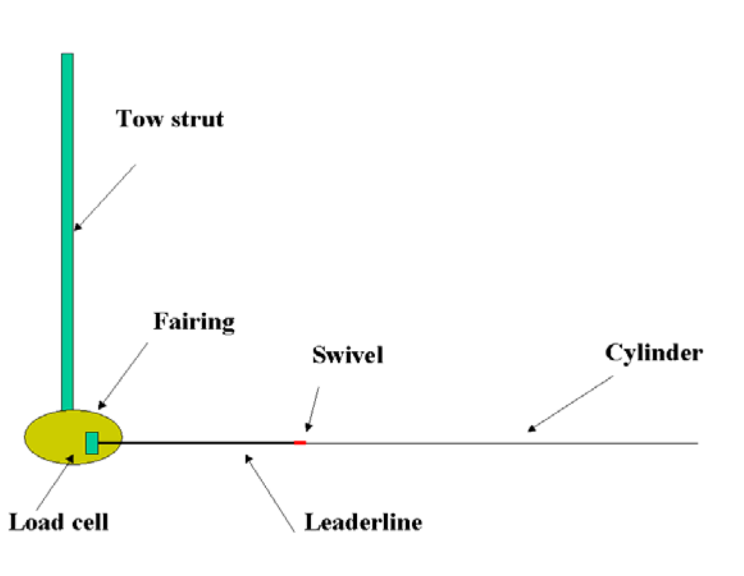

Figure 10: Schematic of towing configuration. The towing configuration includes the tow strut, fairing, loadcell, leaderline, snap swivel, and the cylinder model.

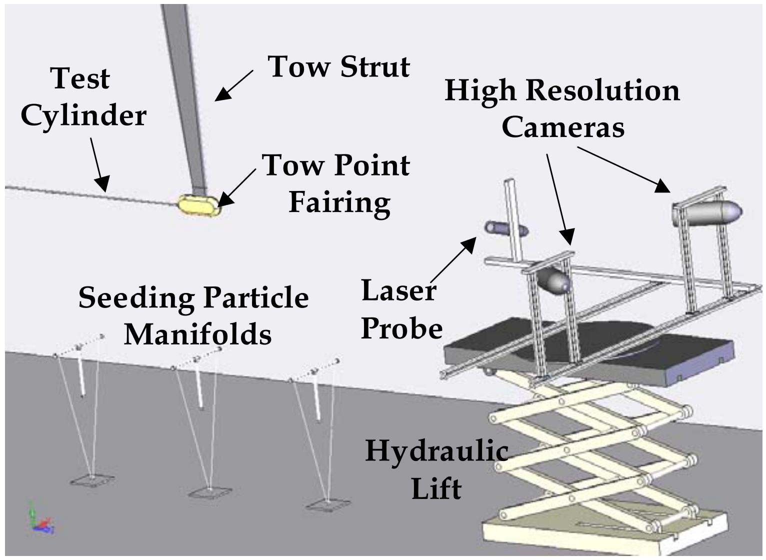

Figure 11: Schematic of test configuration. The test configuration consisted of the hydraulic lift for supporting the cameras and light sheet housings, the towstrut with load cell and model, and seeding apparatus.

3.2.1 Towpoint Wake Evolution into Downstream Flowfield

This section will discuss the influence of the towing hardware on the downstream flow development. Both in the field and laboratory, the filament must be physically attached to a towing device. Any measurements of the boundary flow around the cylinder includes components of the wake from the towing apparatus. Therefore, the flow field behind the towing hardware when no model is attached was measured. This data is used to quantify the flow due to the towing hardware alone which will be compared to the flow field measurements when the cylinder models are attached.

The towing hardware includes both the towing strut and the towpoint fairing. The tow-strut has a 6:1 ogive cross section. Ogive sections are symmetric tapered shapes and are considered to contribute very little to the wake flow at these aspect ratios. However, the fairing around the towpoint is not tapered. It is a blunt shape and is considered to be the primary contributor to the downstream wake. Therefore, an estimate of the wake from the towpoint fairing is described here to characterize the velocity and momentum defect from the upstream towing hardware.

The fiberglass fairing is approximately 6 inches tall, 14 inches long and 3 inches wide. The leading edge radius is 3 inches. From Hoerner [24], the drag coefficient (C_D) for this shape is 0.25 for a 3-dimensional geometry. For a 2-D shape with similar vertical crosssection, i.e. an infinitely wide fairing with the same profile, the drag coefficient is 0.5. The following discussion estimates a conservative wake defect caused by the strut using explicit 2-D wake similarity models from Tennekes and Lumley (21).

For flow past a 2-D body, the momentum thickness of the wake, θ, is related to the drag coefficient through the following expression:

$$D = C_d \frac{1}{2} \rho U_o^2 d = \rho U_o^2 \theta$$

Equation 17

where d is the frontal height. This relationship can be rearranged to relate the drag coefficient to the momentum thickness and frontal height as shown.

$$C_d = \frac{2\theta}{d}$$

Equation 18

Using the 2-dimensional drag coefficient for this fairing, the momentum thickness is 30 mm (1.25 inches). Tennekes and Lumley (21) show that the 2-D centerline velocity deficit falls off with the inverse of the square root of the downstream distance (Equation 19) and the wake width (2*l, where l is the half width) grows with the square root of the downstream distance (Equation 20) .

$$\frac{U_s}{U_0} = 1.58\left(\frac{\theta}{x}\right)^{\frac{1}{2}} \qquad\qquad \frac{l}{\theta} = 0.252\left(\frac{x}{\theta}\right)^{\frac{1}{2}}$$

Equation 19 **Equation 20**

For the present towing configuration, the cylinder is introduced to the flow 15 m (50 ft.) downstream of the towstrut at the end of the leaderline. The 2-D estimate predicts the centerline velocity due to the wake of the fairing to be 0.07 U_o and the wake to have a half width of 5.5 θ at this distance downstream. However, for the towpoint fairing, the flow is approximately axisymmetric and is 3-dimensional. As mentioned above, the drag coefficient for a 3-D geometry is 0.25, half of the 2-D case. Though there are no explicit formulations for the centerline velocity and wake development for the 3-D case, the growth rates are known to be –2/3 and 1/3 respectively. Therefore, the 3-D growth considerations indicate the strut wake values will have a significantly smaller deficit and larger wake width than the 2-D estimates. These values are expected to be significantly smaller than the measured velocities in the boundary layer flow and will be significantly dispersed by the time the model comes into the measurement volume. The velocity field occurring in the strut wake will be measured and compared to these values model estimates.

Also of consideration, the boundary layer growth on the leader line introduces a defect at the leading edge of the test cylinder. Using estimates from Cipolla et. al. [17], the momentum thickness developed on the 15-m leaderline is approximately 6 mm (0.25 inches). The boundary layer is perturbed at the end of the leaderline using the snap swivel device. As discussed previously, this perturbation causes the boundary layer to separate and a new boundary layer is initiated on the filament (Refer to Appendix C: Leading Edge Boundary Condition for Small Diameter Cylinder Tow Tests in Water).

3.3. Drag Measurement Hardware and Acquisition

Drag measurements were made using Sensotec load cells. A load cell was rigidly attached to the towpoint using a steel mounting plate and was enclosed by the towpoint fairing. A 50-lb load cell (Sensotec model 31/3673-01) was used for the low speed runs and a 100-lb load cell (Sensotec model 31/4267-05) was used for the high speed runs where the loads were expected to exceed the load limit on the lower capacity load cell. (Refer to Appendix B for drag estimates. Cipolla, 2003). The load cells were calibrated within the range of expected drag values using standardized weights.

The load cell output was conditioned, amplified and scanned by a digital multi-meter. The multi-meter had an RS232 port which was connected to a laptop PC for serial data collection. The loads were recorded for at least two runs at each speed and model length to ensure repeatability. Tare runs were taken on the leader-line with snap swivel to isolate the drag force acting on the upstream towing hardware alone. These values were subtracted from the total drag measurements when both the leader-line and cylindrical model were towed to determine the drag on the cylinder alone.

3.4. Velocity Measurements and SPIV System

Particle Image Velocimetry (PIV) methods measure the velocity field in a plane at one instant in time. For example, a camera viewing a longitudinal flow plane along the axis of a fixed cylinder would measure the axial and radial components of velocity in the boundary layer in that plane. However, for the present experiment, the filament is not fixed and therefore will not remain aligned with a light sheet oriented parallel to the towing direction. Therefore, this experiment requires an alternate experimental set up.

Using two cameras and a light sheet oriented perpendicular to the towing direction, three components of velocity data can be acquired using Stereo PIV methods. With this set up, data can be collected regardless of the instantaneous cylinder position. Therefore, this orientation enables data to be collected along the entire length of the cylinder though the cylinder may move within the measurement volume. The cylinder position in the field of view was determined image by image and will be discussed in Section 3.5 Experimental Considerations.

The Stereo PIV system consists of a flash lamp pump dye laser, a fiber optic to deliver the beam to the measurement volume, optics to create a light sheet, and two PIV cameras. The laser uses Rhodamine 6G dye and operates at a wavelength of 592 nm. It delivers 750 mJ/pulse with a pulse duration of 12 microseconds. The pulse rate is controlled by a pulse generator which was synchronized with the camera image acquisition system. The light sheet optics are sealed in a submersible housing with a fiber optic feed system connected to the laser. The laser is mounted outside the towing basin in the SPIV staging area. The light sheet is approximately 18mm thick. The cameras are high-resolution Roper Scientific ES4.0's with an image size of 2048 x 2048 pixels. The cameras are set up in dual exposure mode with an acquisition rate of 12 frames per second (6 image pairs per second). As previously mentioned, the axial spatial resolution of the data acquired along the cylinder for each tow speed is a function of this acquisition rate. For this experiment, the cameras were situated side by side with a relative angle to the laser sheet of ±30 degrees. Calibration was performed using a precision target (see Appendix E: Calibration grids) and a commercial software package, DaVis® by Lavision, that develops the mapping functions used to analyze the SPIV data. Calibration will be described in Section 3.4.1 Stereo PIV technique.

The SPIV staging area was located in the photography pit on the North side of the towing basin. The submersible components of the SPIV system include the two cameras and the laser optics secured in aluminum housings (see Figure 12 and Figure 13). These are mounted on an underwater hydraulic platform (see Figure 14). This platform moves in the vertical direction for positioning the cameras and laser sheet relative to the cylinder. The height is adjusted with a hand controlled hydraulic unit located on a land-based palate. The hydraulic platform weighs 3100 lbs in air and 2300 lbs in water. This type of optical table was chosen to permit the SPIV system to come out of the water for alignment purposes and to assist in positioning the measurement plane.

Figure 12: SPIV camera. The camera housing was secured on optical rails. The camera was pointed inward 30 degrees toward the field of interest.

Figure 13: SPIV laser sheet probe. The laser probe was mounted on a cantilevered rail and directed up toward the field of interest. The laser sheet was carefully aligned to be perpendicular to the towing direction

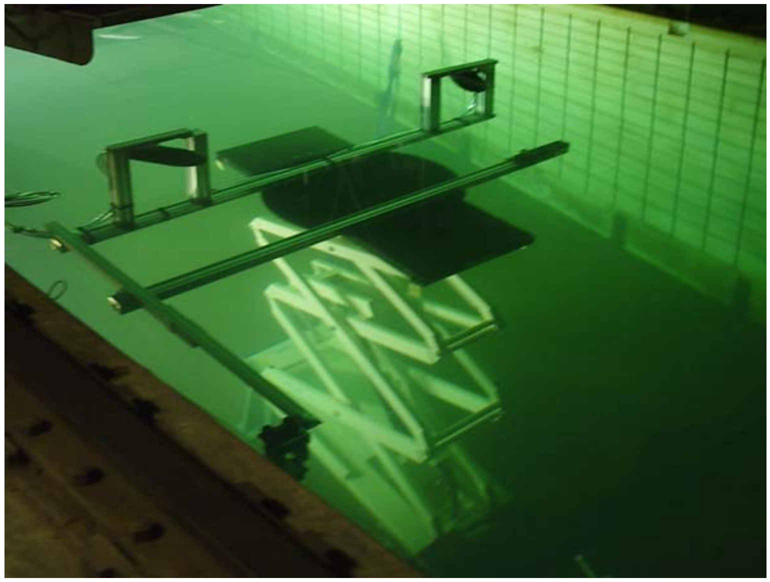

Figure 14: Underwater hydraulic lifting table. An underwater hydraulic lift was used to support the camera housings and laser probe. The lift was modified from a standard land-based man-lift to allow the entire system to be submerged.

Data collection was initiated by an optical trigger located just upstream of the SPIV staging area. An infrared transmitter/receiver unit was attached to the basin rails. As the carriage passed by, a trigger signal was sent to the data acquisition computer and laser system to initiate data collection. Data plane locations were determined by integrating the carriage speed between the initial trigger and the elapsed time to each image pair acquisition. This provides a positional accuracy of better than 0.3 m (see Appendix A).

The seeding system was located at the SPIV staging area immediately upstream of the test section. It consisted of three buoyant seeding manifolds. Each manifold was made of ¾ inch PVC tubing arranged in a ‘T’ shape and had approximately 20 ports. The manifolds were secured with a 30 lb anchor and attached to flotation blocks. Using guide ropes, the manifolds were released and allowed to float to the test depth. A mixture of seeding material (40 micron silver coated glass spheres) and water was pumped through the system to produce a cloud of seed in the test section. The test volume was thoroughly mixed to get a uniform distribution of particles in the test volume.

The particles were chosen such that they were large and reflective enough to provide good images on the CCD for the desired field of view yet small enough to follow the flow. The ability for the particles to follow the flow is determined by looking at the settling velocity, u_s, and the relaxation time, τ_s. As discussed by Raffel et. al, the settling velocity is considered to be governed by Stokes drag and is determined from the particle geometric and mass properties in relation to the surrounding fluid. The relationship is shown in Equation 21 where d_p and ρ_p are the particle diameter and density, and ρ_f and μ are the surrounding fluid density and viscosity.

$$u_s = \frac{g\, d_p^{\,2}\, (\rho_p - \rho_f)}{18\mu}$$

Equation 21

Assuming a particle distribution where the density varies by ±10% due to conglomeration and manufacturing, the heaviest of these particles have a settling velocity of approximately 0.00008 m/s. At this settling velocity, during the longest light pulse separation time used in the SPIV measurements, 6.4 ms, the particle moves vertically by a distance of 0.0005 mm which is quite small relative to the spatial resolution of the measurement, 0.3 mm/pixel. Therefore, the settling velocity does not affect the measurements.

The relaxation time for these particles is estimated by the ratio:

$$\tau_s = d_p^2 \frac{\rho_p}{18\mu}.$$

Equation 22

The relaxation time is approximately 10^{-4} seconds which corresponds to a frequency response of 10^4. Using the previous data determined by Cipolla et. al. (2002), based on the wall shear velocity in the inner most region, the diffusion time scales (l^+/u_τ) for this flow are expected to be on the order of $0.4*10^{-4}$ s to $0.1*10^{-4}$ s. The current measurements will be taken in the outer region where the shear is expected to be significantly less. Therefore, the particle relaxation time is considered sufficient to respond to the local diffusion time scales in the outer region.

3.4.1 Stereo PIV technique

Stereo PIV methods utilize 2-D PIV analysis techniques with additional gradient calibration information to resolve out of plane velocity components. For 2-D PIV, a camera is oriented perpendicular to a laser sheet illuminating a plane of interest. The laser sheet is pulsed and the camera takes a picture of the particles in the flow. After a specified time interval, the laser is pulsed again and the camera takes another picture of the particles that have now moved to a new position due to the flow. Using correlation methods, the mean displacements of small groups of particles are determined and the velocities are calculated by dividing those displacements by the specified time interval.

For Stereo PIV, two cameras separated by a known distance are used to image the same region in space (See Figure 15). The separation causes each camera to have a slightly different view of a common area. The cameras can also be oriented with different angles relative to the light sheet to obtain a greater overlap in the fields of view. When data is collected, the cameras record an image pair in time, as in the 2-D method. These images are analyzed to extract particle displacement information as above. However, for the particle displacement shown in Figure 15 by the dark vector, the left camera sees a larger displacement and the image falls on a different location on the CCD when compared to the right camera. Analysis of the images resolves in-lightsheet-plane motions of the particles for each camera view and then cross references those results using the calibration information to determine the out of plane velocity. This is done using the mapping functions calculated from the calibration images.

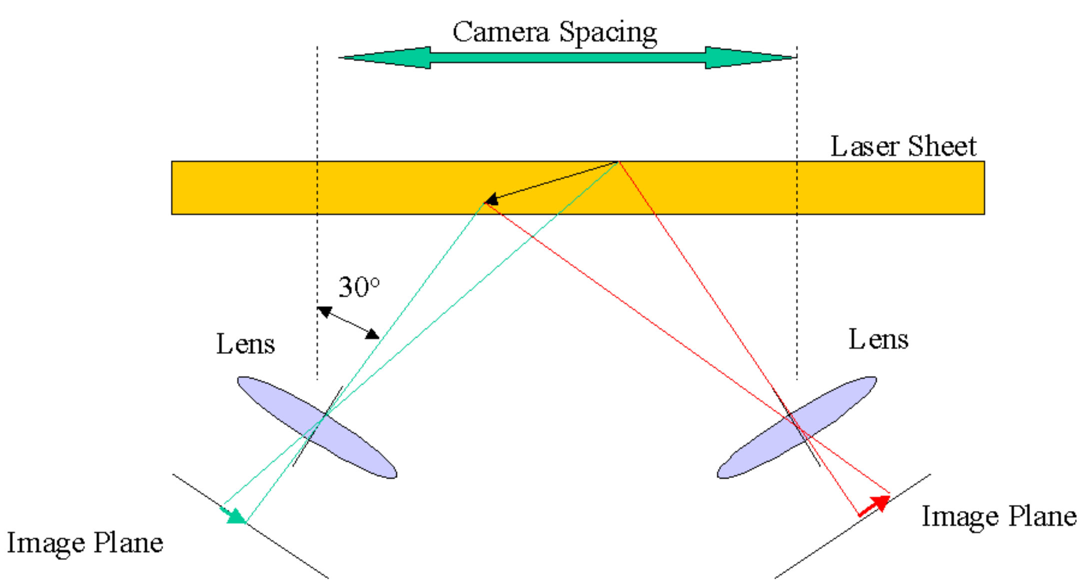

Figure 15: Stereo Particle Image Velocimetry optical set up. The SPIV setup for this experiment used two high resolution cameras mounted upstream of the light sheet. The cameras were mounted side by side, pointed inward with a 30 degree angle relative to the normal of the light sheet. The light sheet was approximately 18-mm thick.

To calculate the mapping functions, an accurately machined calibration target is used, as mentioned above (Refer to Appendix E: Calibration grids). The calibration target contains '+' marks spaced evenly on a 50.8 mm by 50.8 mm (2 in by 2 in) grid. The target is mounted vertically on a milling table in the test bay to ensure accurate positioning of the calibration grid relative to the measurement volume. The target is positioned with its grid face touching the edge of the light sheet and is imaged by both cameras. Great care is required to ensure the target is parallel with the light sheet. This is done using the precise positioning of the milling table and mechanical shims. The target is then traversed to the other side of the light sheet (t = 18 mm) and is again imaged by the cameras. The reduction code, Davis, correlates the positions of the grid points in both cameras in three dimensions using the geometrical information (grid spacing, grid line thickness, and distance traversed) from the set up. The resulting 'mapping' functions are used for determining the particle displacements that occur in the flow. (Refer to Appendix F: Stereo Particle Image Velocimetry Calibration and Mapping Information).

3.4.2 SPIV Resolution

The field of view of the SPIV system determines the spatial resolution of the images and the detail to which measurements can be made in the boundary layer flow. The cameras have a CCD size of 2048 x 2048 which is imaging an area of 60 cm x 60 cm. The resulting spatial resolution is 60cm/2048 pixels or 0.3 mm/pixel. The following discussion will present an estimate of the boundary layer inner length scale and will compare that to the spatial resolution and measuring capabilities of the SPIV system.

Utilizing the data from Cipolla et. al.[17], the drag coefficient for the flow over the .89-mm cylinder is on the order of 0.005 in this speed range. The wall shear stress for the low speed condition is given by:

$$\tau_{avg} = C_d \frac{1}{2} \rho U_0^{\,2} = 0.005 * \frac{1}{2} * \frac{1g}{cm^3} * \left(3\frac{m}{s}\right)^2 = 22.5\frac{N}{m^2}$$

Equation 23

The average friction velocity for this condition is

$$U_\tau = \sqrt{\frac{\tau_w}{\rho}} = \sqrt{\frac{22.5\frac{N}{m^2}}{1\frac{g}{cm^3}}} = 0.15\frac{m}{s}$$

Equation 24

and the resulting viscous length is

$$l^+ = \frac{\upsilon}{U_\tau} = \frac{0.01\frac{cm^2}{s}}{0.15\frac{m}{s}} = 0.000008\,m = 0.008\,mm$$

Equation 25

The present SPIV correlation method uses 16pixel by 16 pixel interrogation windows with a 50% overlap. A velocity vector is resolved every 8 pixels which corresponds to every 2.38 mm. The field of view is resolved into 248 measurements horizontally and 229 measurements vertically. This resolution will allow for measuring the outer region of the boundary layer but the inner region, whose thickness is estimated to be ~10 l^+ = 0.08 mm, will not be resolved.

The time delay between laser pulses was selected to ensure that data was collected with adequate dynamic range in the measured flow field. The dynamic range is determined by the minimum discernable particle displacement and the maximum possible particle displacement that occurs between laser pulses. As mentioned above, the spatial resolution of the SPIV system does not allow for measurements in the high-speed flow region (inner region). Therefore, the time delay was adjusted to more accurately measure the flow in the outer region, where smaller displacements will occur. Initial test runs used time increments based on the tow speed as a first estimate. For example, to measure the high-speed inner flow, a time increment of 1.6 ms for the 3.8 m/s (7.5 kt) case results in axial displacements of 24 pixels for particles moving at towing speed (shown in expression below).

$$PixelDisplacement = 3.8m/s * 0.0016s * 2048pix/0.5m = 24pix$$

This would be imaged on the camera CCD as a 16 pixel displacement due to the 30 degree angle relative to the laser sheet. However, test runs revealed that for this time increment the displacements in the outer flow regions were not measureable. Therefore, in the end, time delays of approximately 4 times the value calculated for the inner regions (as above) were chosen (see Table 2). Also shown are the maximum displacements that would occur if the particles moved at towing speed for that time delay

Table 2: Time Delays for SPIV

Speed (m/s)	Time delay (ms)	Towspeed pixel displacement
3.8	6.4	100
7.6	3.2	100
12.7	2	100
15.2	1.7	100

3.5 Experimental Considerations

This section briefly discusses several experimental considerations which influence the test procedure and design. Three issues are explicitly discussed here; the axial-spatial averaging of the velocity data, wake measurement considerations and the utilization of the data.

This data set will provide boundary flow velocity measurements in discrete planes along the primary axis of the cylinder. As stated previously, the axial spacing of the data changes with towing speed since the number of image pairs per second for the camera is fixed. Previous measurements by Cipolla et. al. (2002) shows that the momentum thickness changes very slowly with axial position. Therefore, consecutive planes of data will be ensemble averaged to evaluate mean and turbulent velocity fields over each 10-m interval of the cylinder. This results in approximately 15 averaged planes of velocity data for a cylinder length of 152 m. In addition, circumferential averaging is utilized to further resolve the data into radial profiles.

It is being assumed that the average velocity in the strut wake and the average boundary flow values are additive. To evaluate the strut wake flow, data collected with no cylinder or leaderline will be collected. The average velocity values determined in the strut wake will be subtracted from the measured cylinder data to remove the strut induced velocity field from the cylinder flow for the averaged velocity measurements. In these calculations the instantaneous location of the cylinder in each flow field will be correlated to the position in the wake to ensure proper weighting of the residual flow fields.

The mean velocity fields will be used to determine the average boundary layer thickness and momentum thickness for each axial location. Fluctuation velocities will be calculated for each ensemble plane of data and used to evaluate average turbulent velocity profiles, as well as average Reynolds stress quantities for selected planes. The turbulent quantities in the boundary layer flow can be compared in magnitude to those in the wake flow. Further, using the method developed by Cipolla et. al. (2002), momentum thickness quantities will be calculated from the drag measurements for the different cylinder lengths and compared to the results determined from the velocity data.

3.6 Test Procedure

The test procedure included model deployment, seeding the measurement volume, positioning the carriage, and conducting the runs. This section will outline each step detailing specific requirements and considerations.

The model deployment required a four person team. There was a carriage operator driving the towing carriage, an on-board observer monitoring the towpoint, and two model handlers hand feeding the model over the towing basin rails. The leaderline was secured to the towpoint and hand maneuvered under the carriage to the East side (front) of the carriage. The end of the leaderline was then handed over the basin rail and the leading edge of the 152-m cylinder was attached to the end of it. Then, the on-board observer would communicate to the driver to slowly move West while the model handlers hand fed the cylinder into the water. The carriage moved at approximately 1.5 knots during deployment. If the filament became taut or tangled, hand-held radios were used to communicate that there was a problem and the carriage would be stopped. Radios were required due to the long distances over which deployment was occurring.

Once the cylinder was completely deployed, the carriage would continue to the SPIV area. At this location the carriage was stopped and the seeding material was pumped into the water and thoroughly mixed. The carriage would then continue West to the starting point. The starting point for each speed would be selected based on the required distance for a stabilized boundary layer to be established as determined by monitoring the drag reading. This ensured that the measured drag values stabilized before velocity measurements were collected.

The cylinder remained attached to the towing strut between runs and would fall on the bottom of the basin when the carriage stopped at the starting position. At this point, the cylinder was stretched out on the basin floor East (ahead) of the carriage. When the run commenced, the carriage would slowly move East until the towpoint was over top of the trailing edge of the cylinder. At that point, the carriage would accelerate to full speed.

The entire run procedure took typically 20-30 minutes. Because of the small physical size of the model and the tapered strut, this run time was sufficient to allow the background turbulence to diffuse and decay. There were no measurements taken in between runs to evaluate the ambient turbulence, but observations were made of the particles in the flow to ensure there were no significant eddies in the flow field.

CHAPTER 4: DRAG RESULTS

The total drag force acting on a towed flexible cylinder can be related directly to the shear force acting on the cylinder wall and to the resulting change in momentum flux due to the boundary flow, as discussed previously. These relationships when used together can resolve relevant wall and boundary layer parameters for cylindrical boundary layers. For this experiment, two sets of drag data were collected. One set was collected using various cylinder lengths for incorporating into previous data sets. The second set of drag data was collected using full length cylinders at the conditions coinciding with the SPIV data. This chapter will present the drag results for the cylinder models of varying lengths and the corresponding wall shear and momentum thickness development. Secondly, the drag results and wall parameters will be presented for the full length filaments for speeds corresponding to the SPIV data set. These values will be used in conjunction with the SPIV velocity field information for evaluating relevant boundary layer parameters.

4.1 Measurements on Varying length Models

Drag loads occurring on the cylinder models were measured at several speeds and cylinder lengths. Averaged drag values occurring on the 0.89-mm cylinder at speeds of 3.1, 5.1, 9.25 and 14.4 m/s (6, 10, 18 and 28 knots) for cylinder lengths varying from 25 m to 145 m are shown in Table 3. Table 4 shows the resulting loads for the 2.5-mm cylinder at lengths from 25 m to 120 m and the same towing speeds as were used for the 0.89-mm cylinder.

Table 3: Average drag measurements in Newtons on 0.89-mm cylinder

Speed	145 m	130 m	115 m	100 m	85 m	70 m	55 m	40 m	25 m
3.1	14.7	13.4	12.5	10.7	9.8	8.8	7.4	6.5	5.2
5.1	35.6	33	28.9	26.7	23.6	20.9	18.3	15.6	12.9
9.3	102.4	94.4	84.6	77.0	69.0	60.6	52.1	44.5	36.7
14.4	231.6	212.9	191.5	173.7	154.5	135.8	118.0	98.9	81.9

Table 4: Average drag measurements in Newtons on 2.5-mm cylinder

	120 m	90 m	60 m	30 m
3.1 m/s	23.2	18.5	13.8	8.9
5.1 m/s	57.9	45.9	33.9	21.4
9.3 m/s	170.1	134.1	98	61.2
14.4 m/s		303.8	222.7	139

The data show that for a fixed diameter, the drag increases with increasing length and towing speed. The drag also increases with increasing diameter.

4.1.1 Wall Shear

Total drag measurements are used to calculate averaged tangential drag coefficient and momentum thickness (refer to Equation 13 to Equation 16) as a function of length. The drag occurring on each incremental length was determined by evaluating the difference between drag values taken at the corresponding adjacent lengths. For example, the drag occurring on the 0.89-mm cylinder segment from 130 m to 145 m at 5.1 m/s is the difference between the drag measured for a length of 130 m and the drag measured for a length of 145 m. The ‘local’ wall shear stress is then determined by dividing that increment of drag by the corresponding surface area of that segment of cylinder.

Figure 16 shows the resulting values for the averaged wall shear stress $\tau_w(x_n)$ occurring on each cylinder segment for the 0.89-mm cylinder at four towing speeds. These values were combined with previously reported results (Cipolla, 2003b). The spatially averaged values of τ_w have been plotted at the center point of each length Δx, assuming a linear variation in τ_w over each Δx. The data reveal non-monotonic development of the average wall shear with distance along the cylinder. The wall shear stress values are on the order of 3 times larger than for a two-dimensional boundary layer at the same Reynolds number based on axial distance and free stream speed. This result is consistent with previous findings by Cipolla et. al. 2002. For comparison, the rate of change of the wall shear stress in a flat plate turbulent boundary layer occurring at distances of 50 m, 100 m and 150 m is calculated to be on the order of 0.5 N/m^2/m, 0.24 N/m^2/m and 0.15 N/m^2/m respectively. Therefore, even for a flat plate turbulent boundary layer the rate of change of the wall shear stress would be close to zero at these lengths.

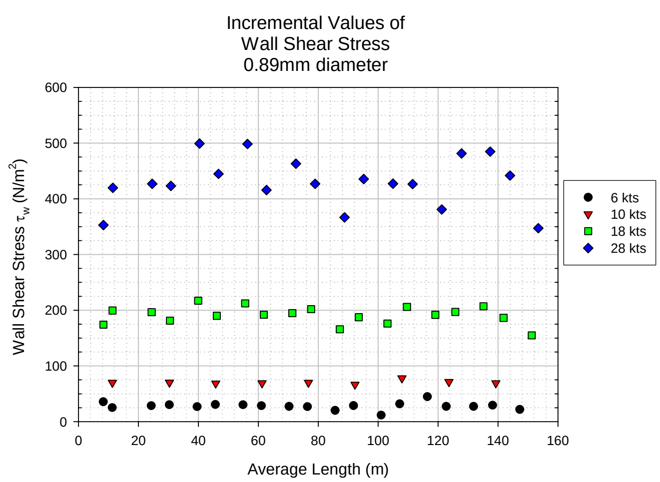

Figure 16: Wall shear stress versus axial location. Wall shear stress values increase with increasing speed. The data from this experiment is shown here with data from previous results (Cipolla, 2003).

4.1.2 Momentum Thickness

Momentum thickness values for this flow geometry are significantly different from flat plate geometries. The results show that for a fixed diameter cylinder and towing speed, the momentum thickness at the end of the cylinder increases with increasing length and that the momentum thickness in the present boundary layer develops more slowly than that of a flat plate (see Figure 17). In particular, the values of θ are only 20-50% of the values predicted for a flat plate turbulent boundary layer (Schlichting, 1979). A thinner momentum thickness is consistent with a higher wall shear stress, based on flat plate results.

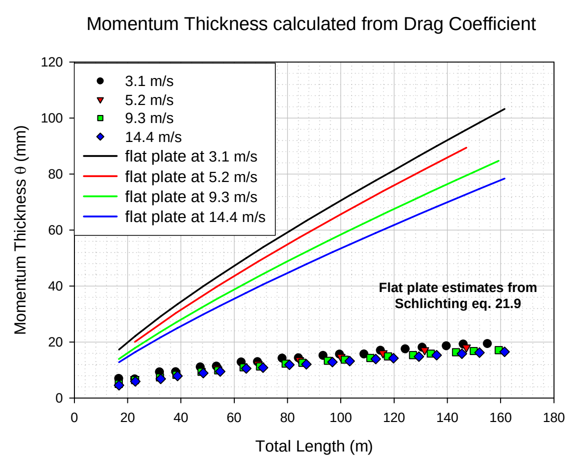

Figure 17: Momentum thickness versus axial length. Momentum thickness is determined from the control volume analysis of the drag data for length cylinder tested. Results are combined with previous results (Cipolla, 2003).

4.2 Measurements on 150-m Filaments

The SPIV data was collected at 3.8, 7.7, 12.7 and 15.4 m/s and therefore, the second set of drag data was collected for the full cylinder length at these speeds. This data was used to give an independent evaluation of the average shear values over the full length of the cylinder as well as the momentum thickness at the trailing edge. Results give a single average shear value over the entire length of the filament. Table 5 and Table 6 show the results for the 0.89 mm and the 2.5 mm cylinders.

Table 5: Momentum Thickness and Shear Results 0.89 mm 150-m Filament

U (m/s)	L(m)	D(N)	C_d	θ (m)	τ (N/m^2)	u_τ (m/s)	u_τ/U	viscous length (mm)
3.8	150	16.524	0.0052	0.0181	39.408382	0.194	0.0510	0.0088
7.6	150	58.360	0.0046	0.0170	139.14949	0.364	0.0479	0.0047
12.7	150	149.442	0.0042	0.0164	356.31885	0.583	0.0460	0.0029
15.4	120	173.076	0.0043	0.0147	515.84106	0.701	0.0461	0.0024

Table 6: Momentum Thickness and Shear Results 2.5mm 150-m Filament

U (m/s)	L(m)	D(N)	Cd	θ (m)	τ (N/m^2)	u_τ (m/s)	u_τ/U	viscous length (mm)
3.8	150	39.184	0.0044	0.0274	33.25937	0.178	0.0468	0.0096
7.6	150	129.273	0.0036	0.0248	109.7327	0.323	0.0425	0.0053
12.7	150	334.415	0.0034	0.0239	283.86341	0.520	0.0410	0.0033
12.7	120	249.813	0.0031	0.0205	265.05984	0.503	0.0397	0.0034

Table 5 and Table 6 show that the drag increases with increasing diameter and speed but that the drag coefficient decreases with increasing diameter at a given speed. Therefore, the drag coefficient increases as the transverse curvature becomes more severe (model diameter decreases). As a consequence, the local wall shear increases with increasing speed and decreasing diameter as well. The shear velocity increases with increasing speed and is on the order of 4-5% of the towing velocity. The viscous length decreases with increasing speed as is expected with the higher shear values. Lastly, the momentum thickness increases with increasing diameter at a given speed. This is expected due to the higher drag values occurring on the larger diameter cylinder.

CHAPTER 5: SPIV DATA ANALYSIS

The analysis of the SPIV data required a several step procedure to evaluate the filament boundary flow. First, the characterization of the flow field from the towing strut is required. This evaluation provides the residual mean velocities and turbulence levels caused by the towing hardware at each speed and axial location. These values, called tare values, are necessary for comparing to the cylinder flow results. Second, the cylinder flow fields are averaged together and the averaged tare fields are subtracted out to remove strut induced ambient flow effects. As previously mentioned, since the boundary layer develops slowly, all planes of data occurring within each 10 meter increment of the cylinder length are averaged together and then averaged azimuthally around the cylinder. Finally, the fluctuating velocity levels are evaluated for the flow with the cylinder and compared to the fluctuating velocity levels in the tare data. This chapter will first discuss the data analysis techniques for the tare data and the averaging methods implemented. Second, the data analysis considerations will be presented for the cylinder data and the averaging and cylinder tracking techniques.

5.1 Tare Data

Averaging the tare data requires summing and averaging the vector images collected over each 10 meter increment downstream of the towing strut. This data yields the evolution of the wake from the towing hardware as a function of distance downstream and is used to provide a benchmark for the background mean velocity and turbulence in the flow when the cylinder is present.

The first SPIV frame used in the averaging procedure is the first frame occurring at or just past the equivalent axial location of the leading end of the cylinder. This is calculated from the known camera trigger location, the towing speed and the image frame rate. The last SPIV frame used in the averaging procedure is the frame occurring at or just before the equivalent axial location of the trailing end of the cylinder. The number of frames used in each average flow field is the integer number of images occurring within 10 meters. The axial location of this average frame is taken as the average axial location of the frames used to obtain each average flow field. This results in a spacing between averaged planes that is smaller than 10 meters and since the SPIV frame rate is independent of towing speed, both the spacing between averaged planes and the number of images used in each average are functions of towing speed. (See Table 7)

Table 7: Frame Calculations for Averaging

Speed m/s (kt)	No. Frames per 10 m	No. of Image pairs per 10 m	Spacing of Avg's (m)	Total number of Averaged planes
3.8 (7.5)	31.10	15	9.65	15
7.7 (15)	15.55	7	9.00	16
12.8 (25)	9.33	4	8.57	17
15.4 (30)	7.78	3	7.72	19

As an indication of the developing strut wake flow field, a single row of axial velocity data is extracted from each averaged data image. The row of velocity data selected in each image was the one with the largest peak axial velocity. These axial velocity profiles are plotted in Figure 18 for each speed. On average, the peak velocities, U_s, are less than 0.03 times the towing speed for all cases at a distance of 15 m downstream from the strut, the equivalent location of the end of the leader line and leading edge of the flexible cylinder. These velocity values are smaller than the 2-D estimate discussed in Chapter 3, as expected. The wake width is defined as the distance from one side of the wake to the other side of the wake where the velocity equals $U_s/2$. In Figure 18a, the wake centerline velocity is approximately 0.09 m/s and the wake velocity reaches half that value at approximately 190 mm and 400 mm across the field of view. From the other profiles, the wake width varies from 200 mm to 300 mm for all cases and is larger than the 2-D estimate, also expected. The wake widens and the peak velocity decays with distance downstream. The profiles appear to move or rotate within the field of view. This may be due to a small angle on the mounting strut which imposed a slight circulation on the downstream flow.

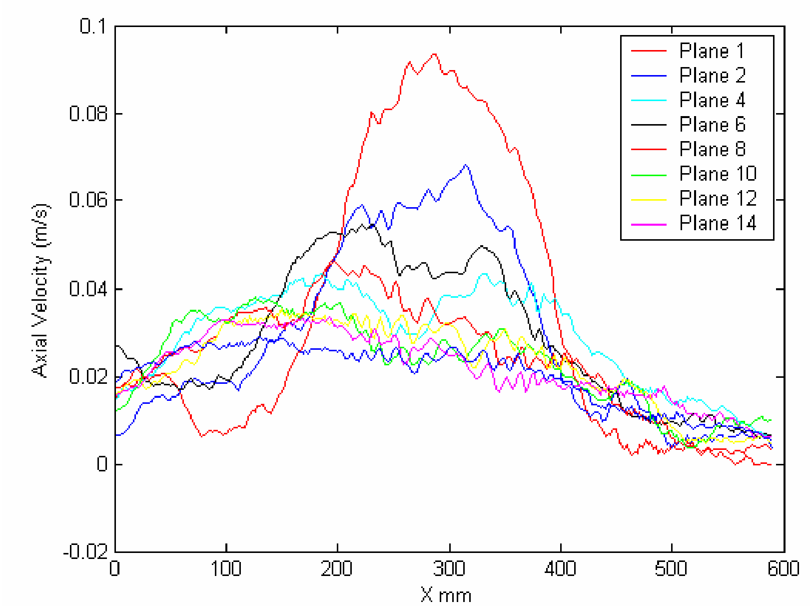

a

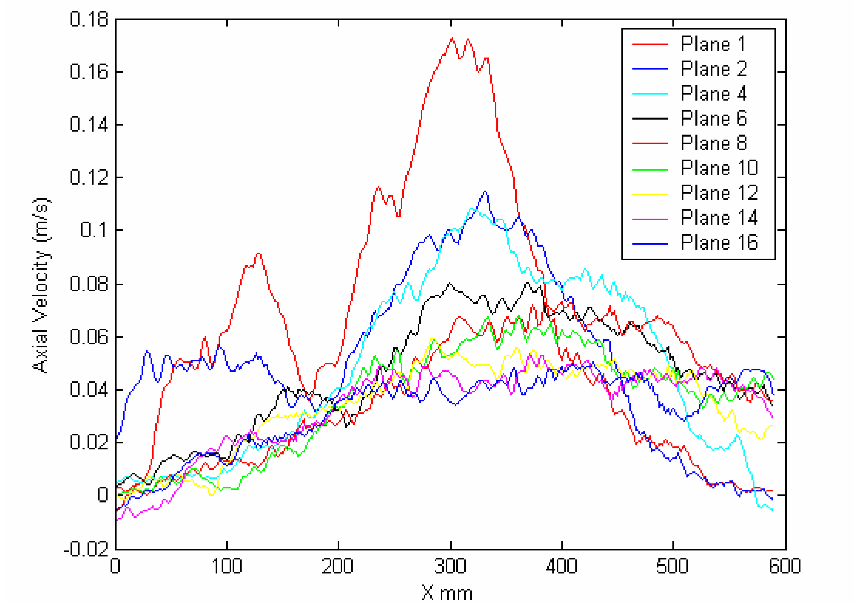

Axial Velocity (m/s)
X mm
Plane 1
Plane 2
Plane 4
Plane 6
Plane 8
Plane 10
Plane 12
Plane 14
Plane 16

b

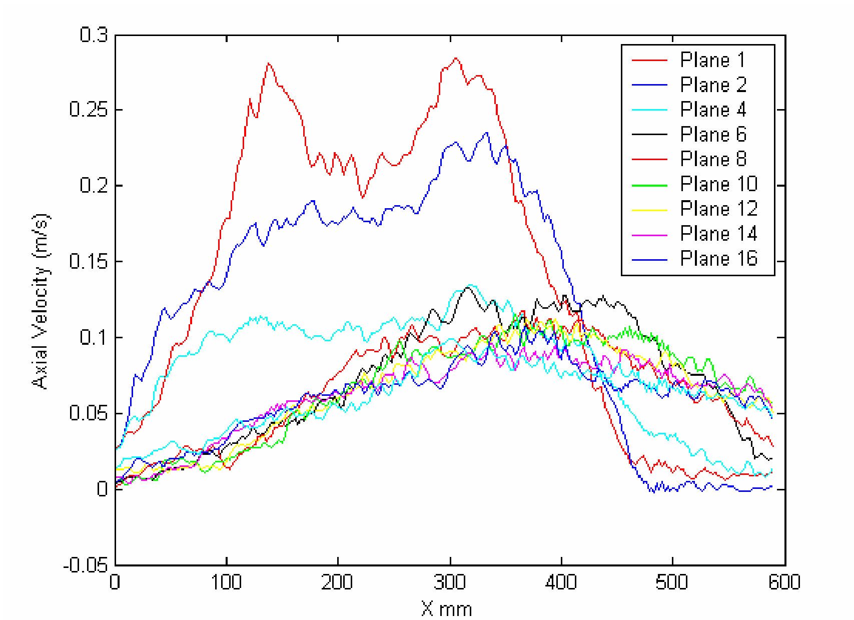

Axial Velocity (m/s)
X mm
Plane 1
Plane 2
Plane 4
Plane 6
Plane 8
Plane 10
Plane 12
Plane 14
Plane 16

c

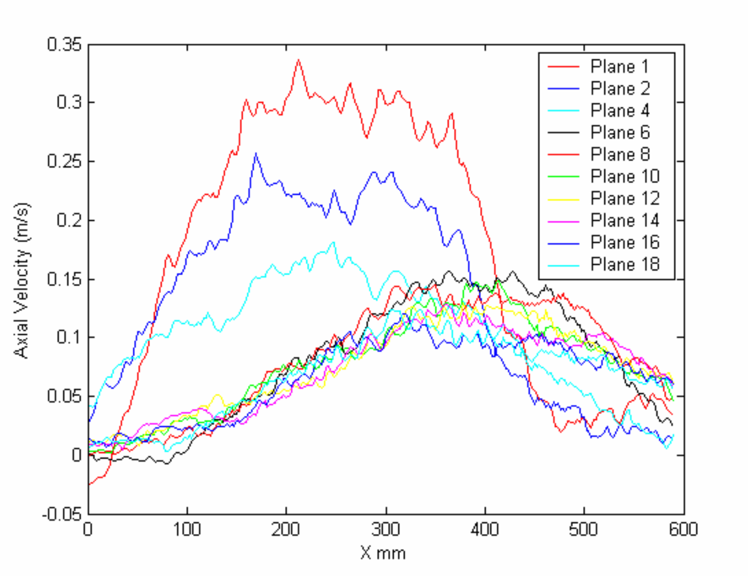

d

Figure 18: Axial Velocity Profile across Average Wake Field. A horizontal profile of the average axial velocity in the wake fields is plotted for different downstream planes. The velocity magnitude diminishes and the wake field spreads wider with downstream distance. The maximum value is on the order of 0.03 of the towing speed at the downstream location corresponding to where the leading edge of the filament would be. a. Towing speed of 3.8 m/s, b. 7.7 m/s c. 12.7 m/s d. 15.4 m/s

Once the averaged fields are determined, the fluctuating velocities can be evaluated. The averaged velocity field is subtracted from each instantaneous velocity field to evaluate the perturbation velocities in the flow. The root-mean-square (RMS) velocity fluctuation is computed using the following expression:

$$I' = \sqrt{\frac{\sum_{i=1}^{N}(I_i - I_{avg})^2}{N-1}}$$

Equation 26

where I_{avg} is the averaged velocity field image, I_i is the instantaneous field image, I' is the fluctuation field image and N is the total number of images being averaged together. The RMS velocities in the strut wake are less than 0.001 times the towing speed for all cases. The RMS axial velocity fluctuation profiles occurring in the wake are presented with the velocity profiles occurring in the cylinder flow in Chapter 7 and Appendix H: Fluctuating Velocity Profiles.

5.2 Cylinder Data

Evaluating the average cylinder flow field required image manipulation due to cylinder motions within the field of view. Therefore, it was necessary to first locate the cylinder in the data image. Considering that the high-speed fluid is adjacent to the cylinder, the flow field was analyzed to identify where the high axial velocities were occurring. This search was done by calculating the total magnitude of the axial velocities occurring in a predefined search window. This value is taken as the local norm for that region of the flow. The region with the largest norm value can be considered to contain the cylinder. This search method was referred to as a Regional Norm technique.

The Regional Norm method uses a distributed group of vectors for determining cylinder location minimizing the effect of individual spurious vectors on that determination. An initial search window of 8x8 vectors is analyzed to identify the fastest moving fluid. The search is done by using a 50% overlap between successive search windows. Once the window containing the largest net axial flow is identified, the region is further interrogated to more precisely locate the cylinder within this region. A refined search of the window is conducted to identify the 3x3 vector region with the highest speed flow. The center of the 3x3 region is taken to be the location of the cylinder. This is then identified as the new image center and is overlaid, or collocated, with the image centers of the other relevant planes of data. This method allows velocity vectors to be averaged based on their relative position from the cylinder, not relative to their positions in the field of view.

For each cylinder image, the corresponding averaged strut wake field is repositioned according to the cylinder location determined from the Regional Norm. This effectively creates a composite wakefield. This is necessary due to the motion of the cylinder through the field of view. Each cylinder location requires a different reference point in the wake velocity field. The net composite wake is subtracted from the net averaged cylinder fields to result in the flow field from the cylinder boundary layer only. Figure 19 shows the averaged velocity field for the 2.5 mm cylinder at 12.8 m/s (25 knots). The vectors indicate the in-plane velocity components. The color contours represent the axial velocity magnitude, white being high speed and black being zero speed. Figure 20 is a 3-D rendition of the averaged cylinder flow field rotated 90 degrees to illustrate the mass flux out of the plane of measurement.

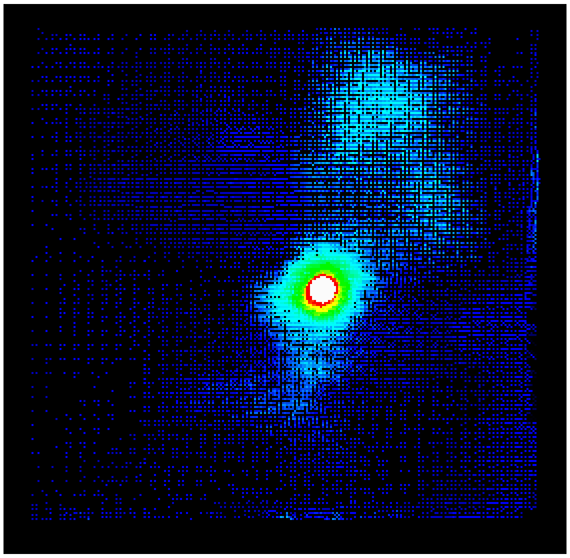

Figure 19: Average SPIV velocity field. The averaged velocity field for the cylinder flow has high speed fluid in the center of the region of interest and the velocity decreases with distance from the cylinder. This image was determined for a towing speed of 7.7 m/s and a cylinder diameter of 2.5-mm. This average was calculated for a distance approximately 140 meters from leading edge of the filament.

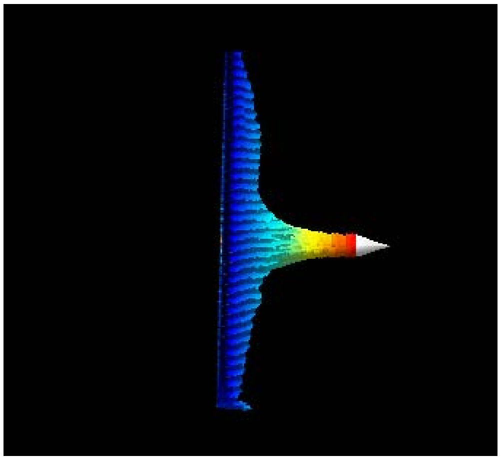

Figure 20: Three dimensional averaged SPIV velocity field in a profile view. The averaged velocity field, when viewed in three dimensions from a profile view, illustrates the flow pattern resulting from the cylinder boundary flow. The flow appears to be pulled through the test volume, resulting in a cone-like shape for the velocity field. The white and red colors correspond to the highest speed fluid. Blue and black is slow moving fluid. This image was determined for a towing speed of 7.7 m/s and a cylinder diameter of 2.5-mm.

The axisymmetry of the averaged boundary layer data was examined. A horizontal profile and a vertical profile that go through the known location of the cylinder were selected to be reference data and were considered to be the indicators of the flow axisymmetry. The velocity profiles show good agreement near the cylinder indicating that the measurements are axisymmetric in that region but the amount of symmetry changes with distance from the cylinder, as shown in Figure 21. Figure 21a. shows that the velocity values are almost equivalent out to distances of 50 to 80 mm for the horizontal and vertical profiles in the first averaged plane of data. However, the profiles have large differences further away from the cylinder. The flow also appears to become more axisymmetric with downstream distance, as shown in Figure 21 b and c.

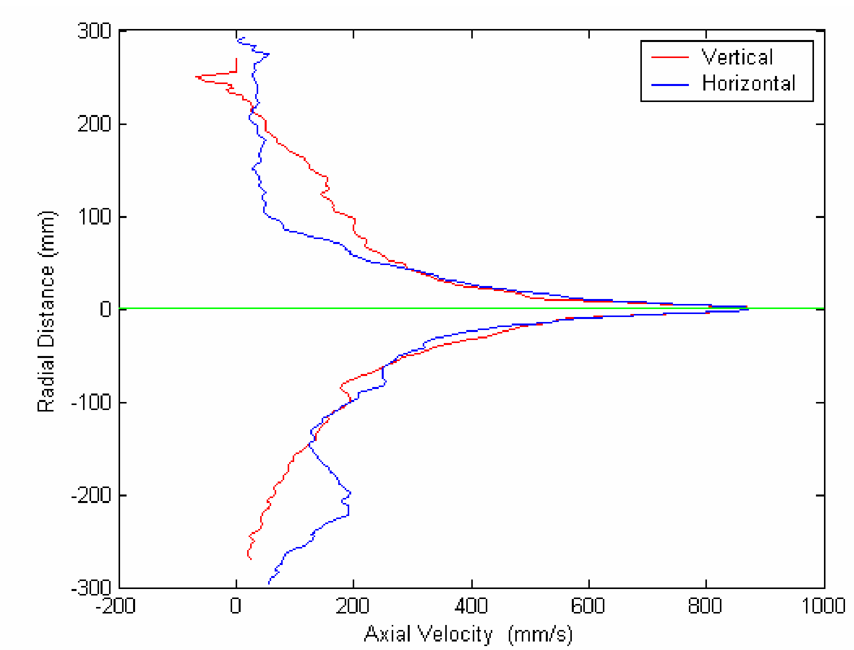

a)

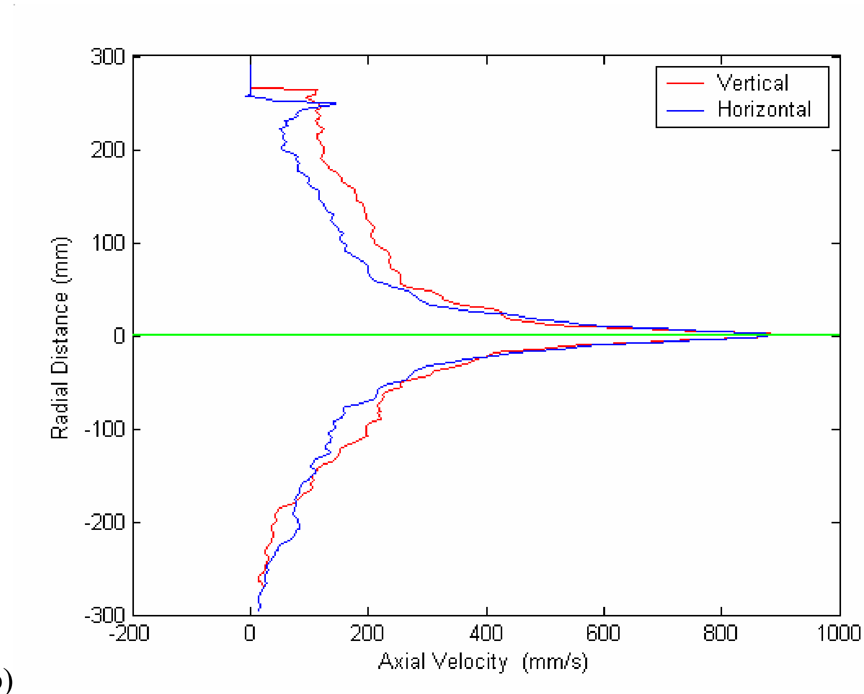

b)

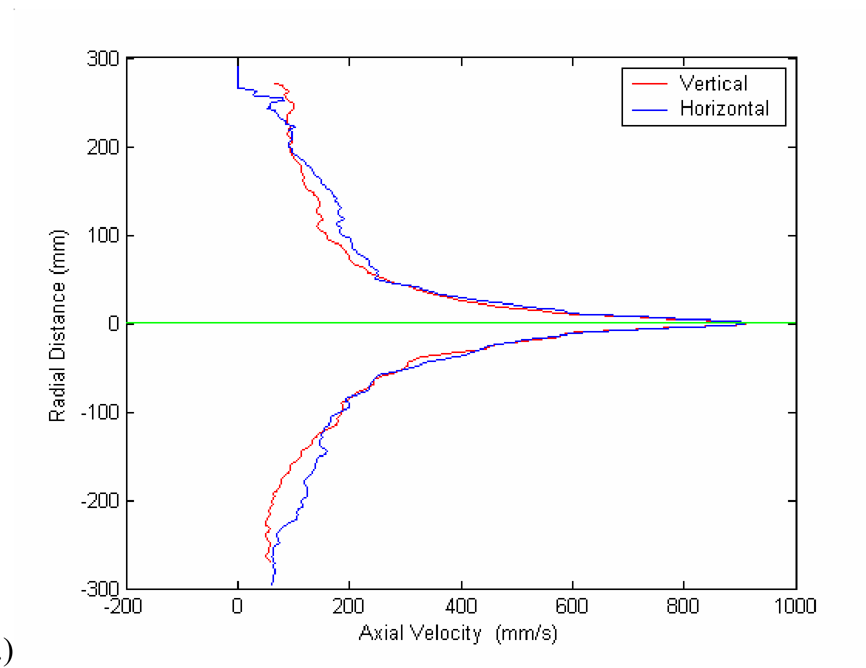

c.)

Figure 21: Axisymmetry profile examination. Horizontal and vertical profiles were plotted to examine the axisymmetry of the flow around the filament. The profiles shown are for U=12.8 m/s and d=2.5-mm. a. Averaged plane 1 b. Averaged plane 5 c. Averaged plane 10.

To quantify the symmetry of the flow, a ratio of corresponding axial velocity values was evaluated. The velocity at each radial location was divided by the velocity on the opposite side of the cylinder at the same radial distance to produce a symmetry ratio. An axisymmetric profile would result in symmetry ratios of 1 at all positions. The data for U=12.8 m/s and d=2.5-mm is shown in Figure 22 and indicates that the flow is symmetric near the cylinder and deviates further from the boundary. The symmetry ratios in plane 1, Figure 22 a, are close to 1 over the entire vertical profile but they deviate from 1 at approximately 80 mm from the boundary for the horizontal profile. For planes 5 and 10, Figure 22 b and c, the ratio remains close to 1 over both profiles. This indicates that the flow is axisymmetric further downstream.

Fluctuating quantities at each plane are evaluated using the average cylinder flow fields and each instantaneous field . For data with the cylinder present, the cylinder location in each instantaneous velocity field is taken as the cylinder locaton in the correspoding averaged cylinder flow field. The difference between the mean and instaneous velocity fields is then squared and summed over all instantaneous images in the average. for that axial location These RMS values are evaluated over the entire field. Chapters 6 and 7 will present the averaged boundary layer data and the turbulent velocity data examined for this experiment.

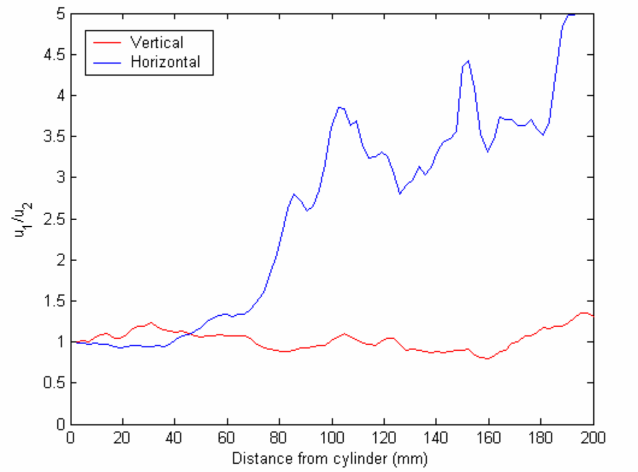

a.)

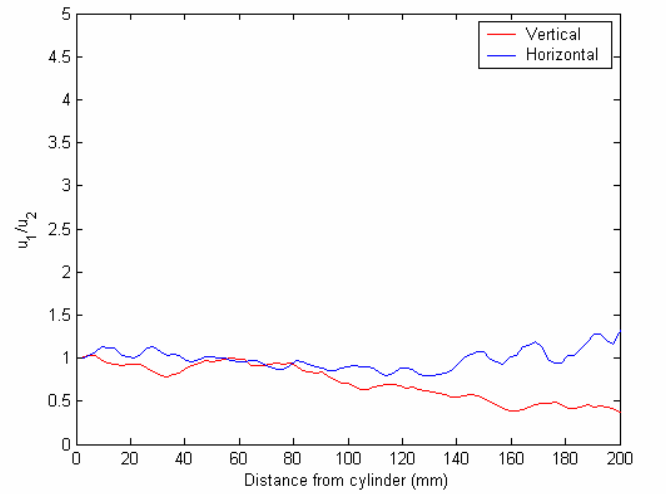

b)

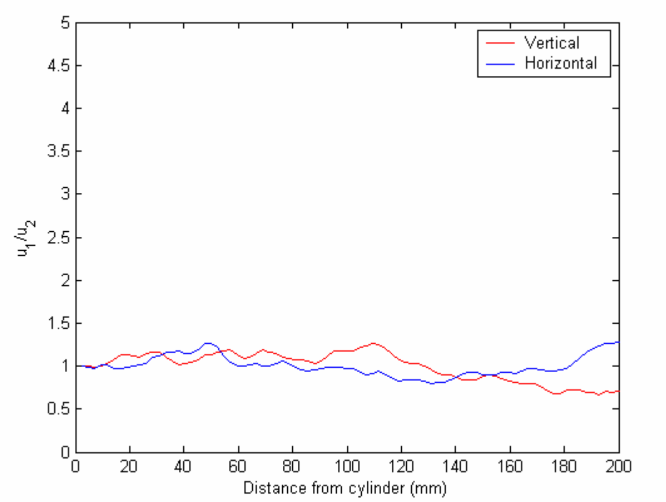

c)

Figure 22: Velocity ratios. The ratio of the axial component of velocity on opposite sides of the cylinder (u1/u2) versus distance away from the cylinder indicates the extent to which the flow is symmetric. The ratio will be equal to 1 when the velocities are the same on either side of the cylinder indicating the flow is symmetric. U=12.8 m/s and d=2.5-mm. a. Averaged Plane 1 b. Averaged plane 5 c. Averaged Plane 10.

CHAPTER 6: AVERAGED BOUNDARY FLOW RESULTS

The averaged velocity fields measured in the boundary layers of the flexible cylinders are analyzed First, the averaged fields are azimuthally averaged around the cylinder to obtain the mean boundary layer velocity profiles. These velocity profiles reveal a recurrent relaxation in the axial development of the boundary layer. The profiles are analyzed to extract the boundary layer thickness (δ), displacement thickness (δ^*), and momentum thickness (θ). These parameters are used to describe the evolution of the boundary layer.

6.1 Boundary Layer Profiles

As previously mentioned, the flexible cylinder is located in the center of the averaged flow fields as discussed in Section 5.2 Cylinder Data. The axial component of these mean flow fields are azimuthally averaged around the cylinder to determine the boundary layer profiles. The first step is to identify each vector in terms of its radial position relative to the cylinder location. The effective radial location of each velocity measurement relative to the cylinder was determined by using the relative column and row distances from the cylinder. The horizontal and vertical distances between adjacent velocity measurement locations in the data array is Δx=2.38 mm and Δy=2.38 mm respectively. The radial distance is then given by

$$r = \sqrt{(n\Delta x)^2 + (m\Delta y)^2}$$

Equation 27

where n and m are distances in columns and rows between the cylinder and the vector velocity measurement point. Each velocity vector is averaged azimuthally with all other velocity measurements occurring within the same radial 'band'. The band is defined to be of a thickness equivalent to the vector spacing. A vector occurring at a distance r is considered to be in band 'i' if $r(i) < r < r(i)+2.38$ mm (see Figure 23). All vectors occurring within band 'i' are averaged together and considered to be located at radial position r(i).

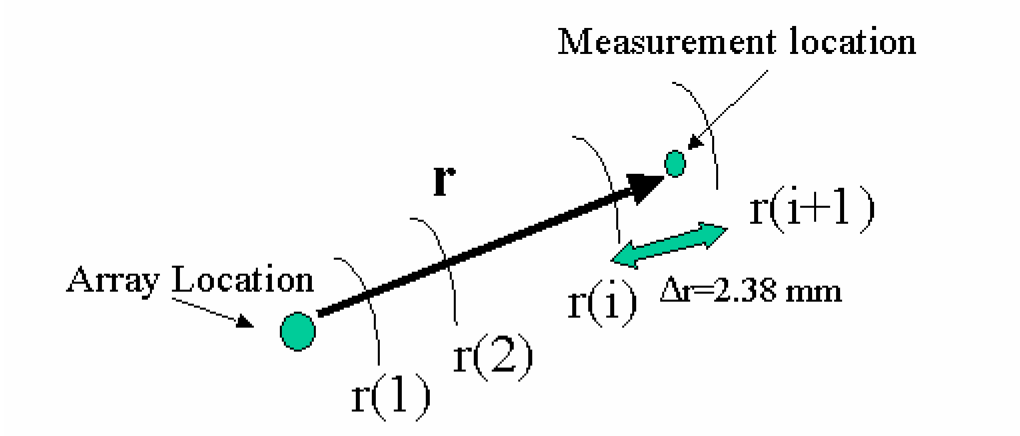

Figure 23: Schematic of vector 'banding' procedure. Averaging the vector fields required azimuthal averaging of the velocities. The radial location of each vector measurement was determined. Each measurement was averaged together with other measurements occurring in its corresponding band..

Azimuthal averaging greatly improved the statistical reliability of the results. The number of samples in each radial band increases with distance from the cylinder as shown in Figure 24 . The inner most value is the average of 9 samples (the center value is included in the calculation) and the outermost locations include approximately 700 samples. However, since each average image is created from approximately 40 instantaneous images, there are approximately 360 instantaneous samples at the inner most radial position and 28,000 instantaneous samples at the outermost location. This provides sufficient sampling to calculate the mean and fluctuating quantities occurring in the flow. Convergence was evaluated for both averaged and RMS velocity fluctuations. The mean velocities converged to within 0.5% of the final values while the RMS velocities converged to within 3% of the final values. Further discussion and description is included in Appendix J.

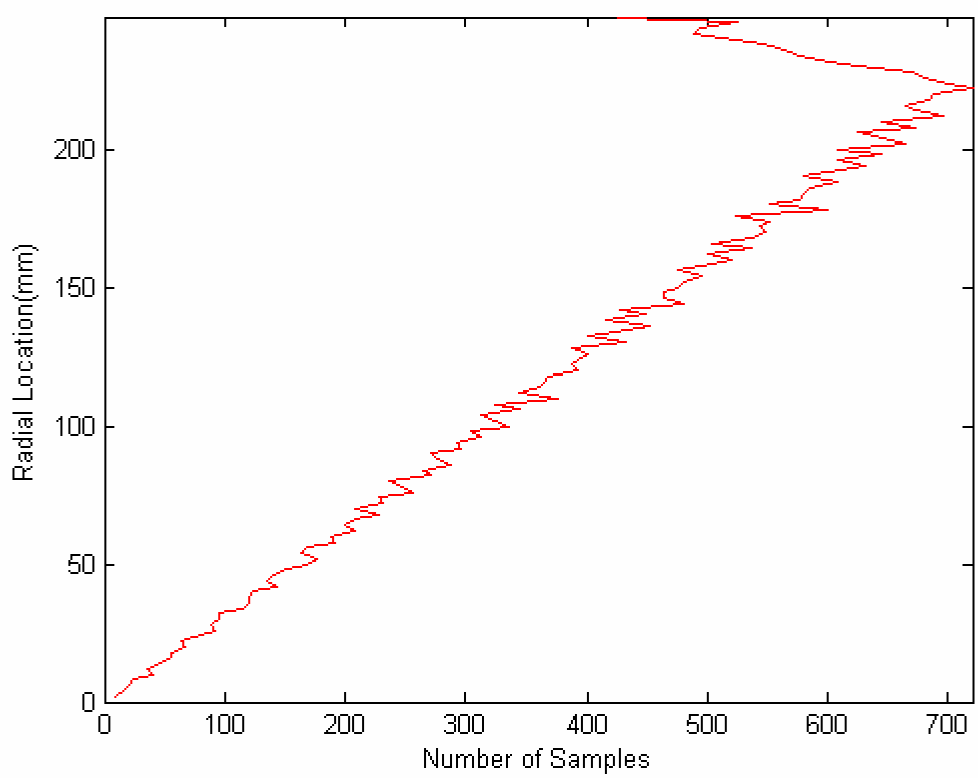

Figure 24: Number of samples per radial location. The number of samples increases with increasing radial location due to the increased perimeter over which samples are averaged

As an example of the averaged boundary layer profiles, the mean axial velocity is plotted versus radial position for a number of axial positions along the cylinder in Figure 25 (U=3.8 m/s and d=2.5mm). The profiles are smooth and have a traditional boundary layer profile shape. There is a significant high-shear region near the cylinder and the velocity approaches zero, the ambient flow condition, as the radial distance increases. The complete set of profiles for all towing speeds and both diameter cylinders is shown in Appendix G.

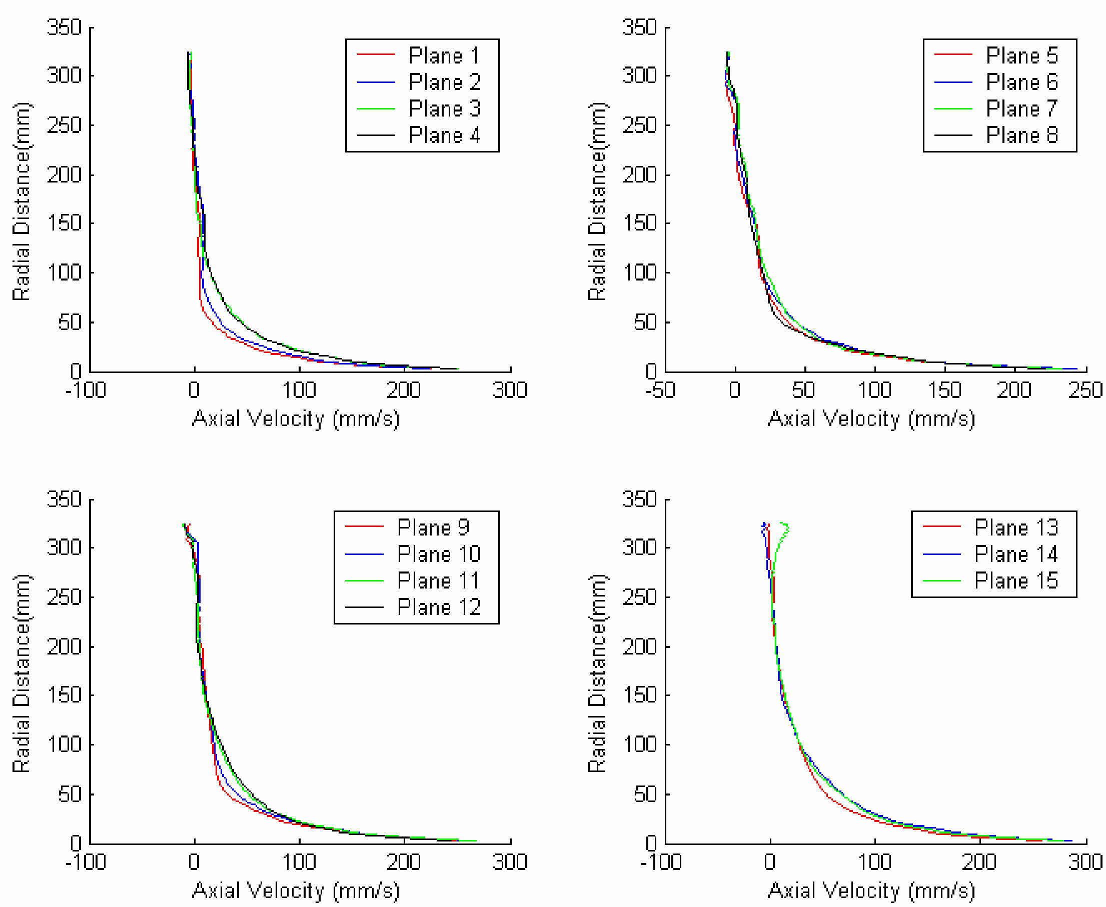

Figure 25: Mean axial velocity versus radial location for U=3.8 m/s and d=2.5-mm at 15 axial planes along the cylinder. The spacing between measurement planes is 9.65 m. Average measurement plane 1 is located approximately 5 m from the leading end of the cylinder.

The evolution of the profiles in Figure 25 suggests a departure from a classic boundary layer growth model. In the classic model, the local wall shear, indicated by the near wall velocity gradient, monotonically decreases and the boundary layer thickness monotonically increases. For data shown in Figure 25, the most upstream profile (average measurement plane 1) shows a high velocity gradient near the boundary. This occurs for all speeds and diameters, as expected. Downstream the profiles become more full as the effect of the cylinder spreads radially. This causes a reduction in the local velocity gradients near the wall (averaged planes 2 to 8). Further downstream, however, the boundary layer profiles exhibit a relaxation and consequently there is an increase in the local near-wall velocity gradients (planes 9 and 10 compared to 8). The profiles then begin to fill out again (planes 14 and 15). This relaxation is seen at all speeds and diameters as shown in Figure 26 a through g. For example, referring to Figure 26 d) 7.7m/s 2.5mm,

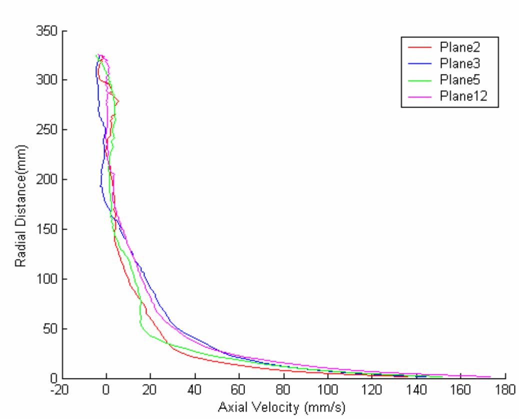

a)

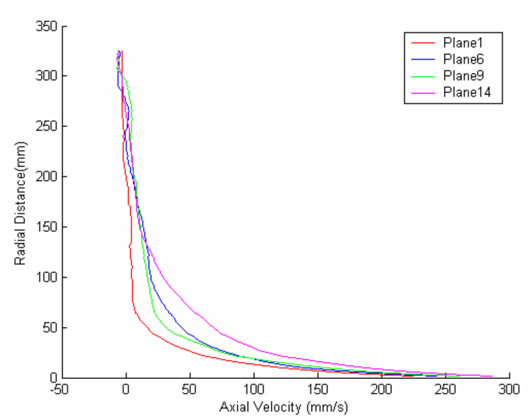

b)

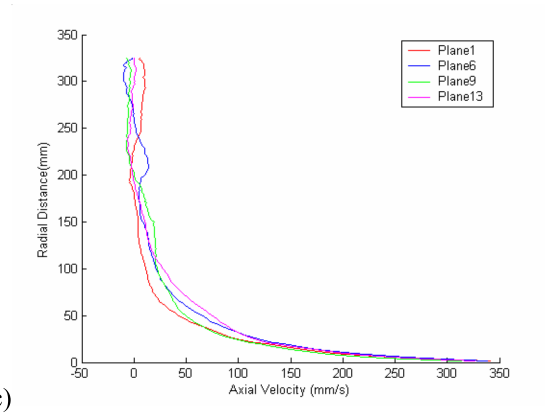

c)

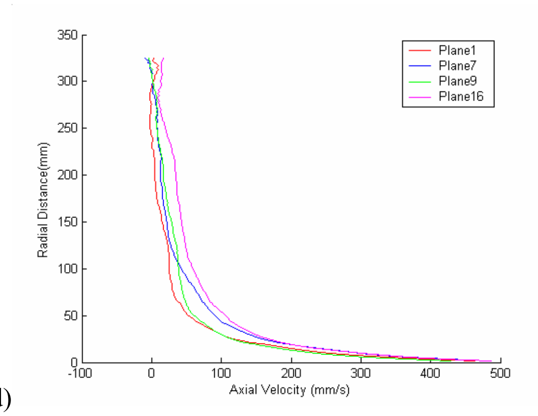

d)

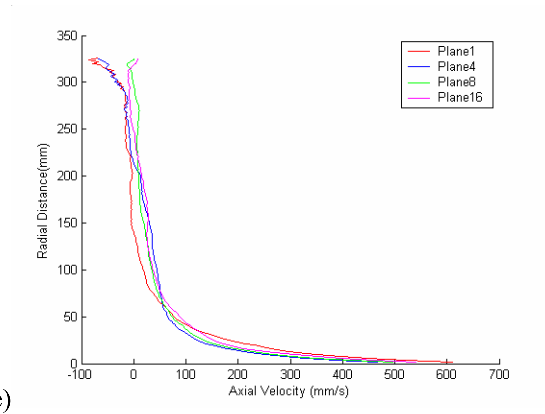

e)

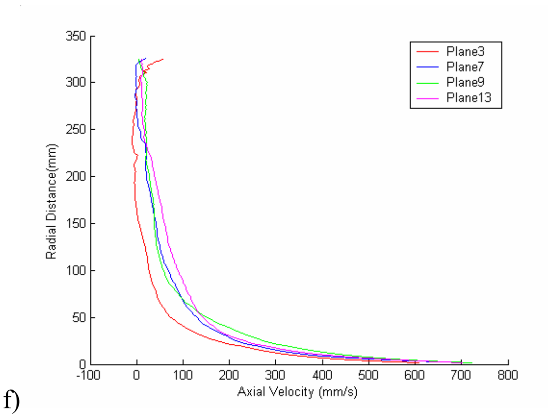

f)

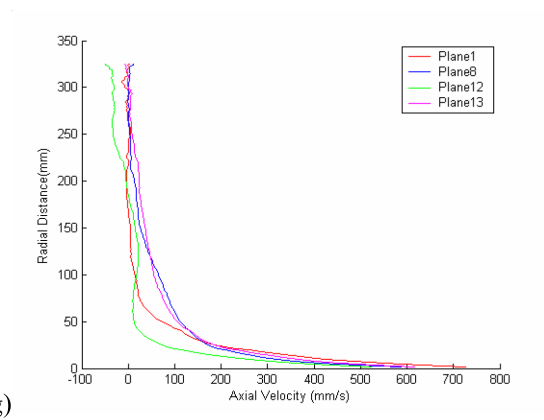

g)

Figure 26: Boundary Layer Profile Relaxation. Average profiles show a relaxation occurring in the fullness of the boundary layers along the length of the cylinder. a) 3.8 m/s 0.89-mm b) 3.8 2.5-mm c) 7.7 m/s 0.89-mm d) 7.7 m/s 2.5-mm e) 12.8 m/s 0.89-mm f) 12.8 m/s 2.5-mm g) 15.4 m/s 0.89- mm

there is high shear, high momentum fluid near the boundary in the profile for averaged plane 1. A reduction in the local fluid shear occurs as the boundary flow develops downstream to plane 6. The boundary layer then experiences a relaxation causing the velocity gradients to increase near the boundary in plane 9. The boundary layer again begins to develop and again results in reduced shear downstream which is evident in plane 16. This result complements the findings from the cylinder drag measurements (Section 4.1.1 Wall Shear) where the wall shear values do not develop in a monotonic fashion but fluctuate along the length of the filament.

The boundary layer profiles can be scaled using the inner variables u_τ. For planar boundary layers, the profile in the log region relates the local velocity divided by the wall shear velocity and the distance from the wall divided by the viscous length, ν/u_τ as follows:

$$\frac{\bar{u}}{u_\tau} = \frac{1}{\kappa}\ln\left(\frac{yu_\tau}{\upsilon}\right) + 5.0$$

Equation 28

where κ is the Von Karman coefficient, 0.4 and *U* is measured in the reference frame fixed with respect ot the wall. This is the logarithmic form of the 'Law of the Wall'.

For the present experiment, the boundary layer profiles are plotted using inner variables ($u^+=U_{tow}-\bar{u})/u_\tau$ and $y^+=y/(\nu/u_\tau)$) in Figure 27. The velocity term is expressed as a velocity difference because in the current experiment, the velocity measurements are made in a reference frame fixed with respect to the fluid at infinity. The shear velocities are calculated using the wall shear stress values from the drag measurements and are shown in Table 5 and Table 6. The non-dimensional boundary layer profiles are shown in Figure 27. (Note: $\bar{u}$ is expressed as u_{avg} in graphs.) Like the flat plate case, the non-dimensionalized profiles form a straight line in the central region indicating a logarithmic relationship.

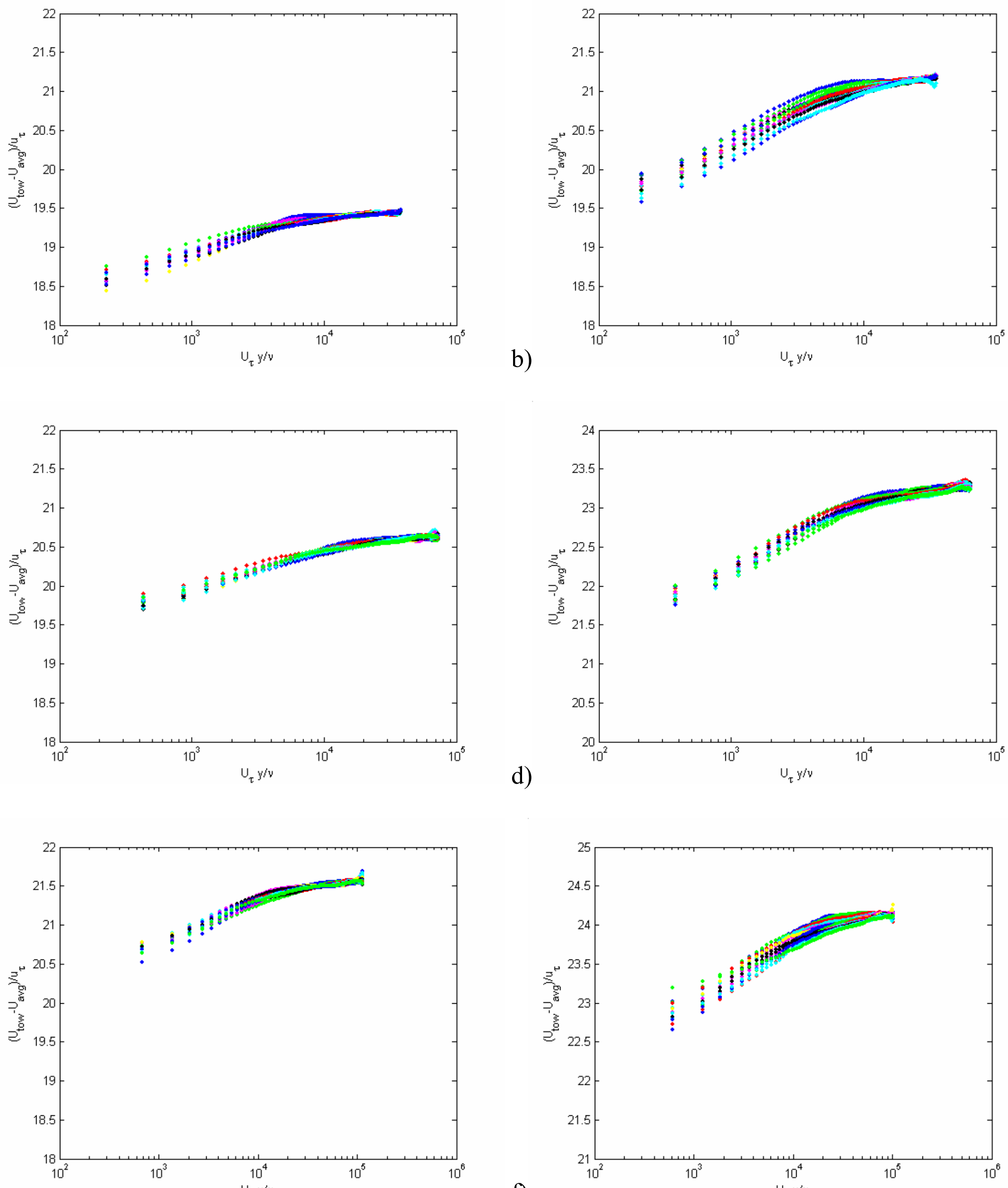

a) b) c) d) e) f)

g) 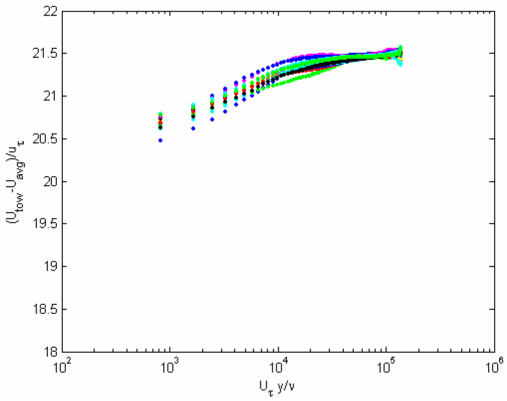

Figure 27: Non-dimensionalized Boundary Layer Profiles using Inner Scaling. Boundary layer profiles nondimensionalized with inner variables reveal a change in slope with change in transverse curvature. a) 3.8 m/s 0.89 b) 3.8 2.5 mm c) 7.7 m/s 0.89 mm d) 7.7 m/s 2.5 mm e) 12.8 m/s 0.89 mm f) 12.8 m/s 2.5 mm g) 15.4 0.89 mm

For the largest values of y+ in Figure 27, the nondimensional profile develops a zero slope indicating that this region is outside the boundary layer. The non-dimensionalized data was analyzed to determine mean coefficients for a logarithmic boundary layer profile formulation as shown:

$$u^+ = A\ln(y^+) + B$$

Equation 29

The resulting constants for each condition are shown in Table 8 and Table 9.

Table 8: Profile fit using inner variables for 0.89mm line

Speed m/s (kts)	A	B
3.8 (7.5)	0.2	17.6
7.7 (15)	0.22	18.4
12.9 (25)	0.24	19.1
15.4 (30)	0.23	19.2

Table 9: Profile fit using inner variables for 2.5mm line

Speed m/s (kts)	A	B
3.8 (7.5)	0.33	18.0
7.7 (15)	0.37	19.6
12.9 (25)	0.35	21.3

The slopes of the profiles, as indicated by the constant A, for each diameter filament are comparable for the different speeds. In general, the boundary layer profiles for the 0.89-mm line satisfy the following relationship:

$$\frac{U_{tow} - \overline{u}}{u_\tau} = 0.22 \ln(\frac{u_\tau y}{\upsilon}) + B$$

Equation 30

while the profiles for the 2.5-mm line satisfy:

$$\frac{U_{tow} - \overline{u}}{u_\tau} = 0.35 \ln(\frac{u_\tau y}{\upsilon}) + B$$

Equation 31

Where, as mentioned above, the velocity term on the left hand side of Equation 30 and Equation 31 has been put in the same reference frame as that in Equation 29, i.e., the left hand side is zero at the wall.

Based on these results, increasing transverse boundary curvature (smaller diameter) reduces the slope in the log region (smaller values of A) of the boundary layer profile. This trend of decreasing slope with increased transverse curvature is also shown in data for fixed cylinders, see Figure 28. In this fixed cylinder data, the non-dimensionalized profiles for cases with cylinders of radii 0.5-mm (0.02-in) and 0.25-mm (0.01-in) where δ/a values reach 27 and 37.5, respectively, fall below the flat plate profile. Data points were selected from Figure 28 for each case to estimate the slope and intercept values for comparison to the present filament results. These estimates are shown in the table below.

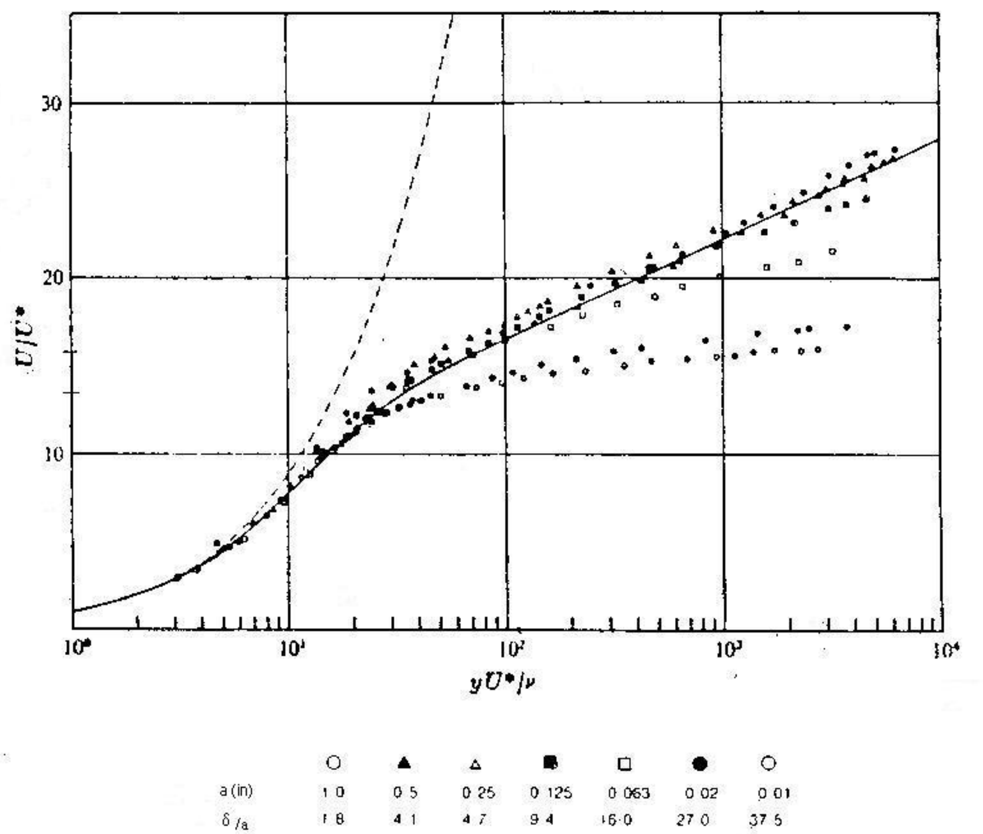

Figure 28: Non-dimensional Velocity Profiles reprinted from *Lueptow, R., "Turbuent Boundary Layer on a Cylinder in Axial Flow", NUSC Technical Report 8389, Sept. 1988.* (12). The profiles indicate that for cases with severe transverse curvature the slope is reduced when compared to a flat plate profile.

Table 10: Estimated values and fits for small diameter boundary layer profiles from Figure 28.

A (mm)	δ/a	y_1^+	u_1^+	y_2^+	u_2^+	A	B
0.25	37.5	1200	15	100	14	0.93	12.1
0.50	27.0	2000	17	100	15	1.53	11.9

The coefficients in Table 10 are consistent with the trends indicated from the velocity results from the current experiment, the values of A are smaller and the values of B are larger than the flat plate boundary layer case (zero boundary curvature) and this trend continues as the curvature of the cylinder increases. However, the values of A and B are larger and smaller, respectively, than the values determined for the current data set. This may be an indication that these constants are strongly dependent on δ/a. While the boundary curvature for the present cylinders and the fixed cylinders are comparable (a = .45-mm and 1.25-mm for the present experiment and a= 0.25-mm and 0.5-mm for the fixed cylinder experiments, see Table 10), the ratio δ/a is 27 to 37.5 for the fixed-cylinder experiments and on the order of 50 to 100 for the present experiments, see the following section. For comparison, the nondimensional boundary layer profile in the log region derived from Figure 28 (Lueptow, 2002) , the present data (Equation 30 and Equation 31) and the flat plate are plotted in Figure 29.

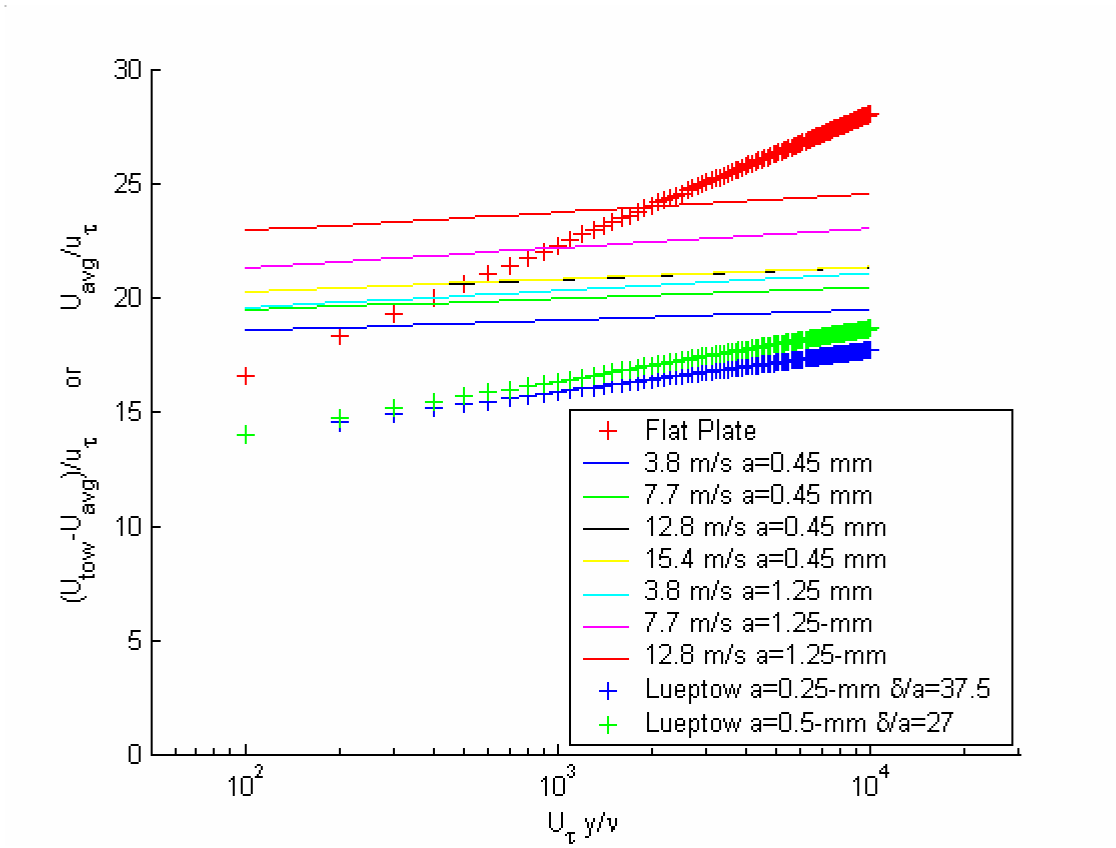

Figure 29: Non-dimensionalized Boundary Layer Fits. Using the profile fits and the estimated values from Table 10, the non-dimensionalized boundary layer profiles for the small diameter arrays have a smaller slope than the flat plate boundary layer.

The flat plate profile is the limiting case where δ/a is zero for all δ since the effective radius of curvature is infinite. In the present experiment, δ/a values approach 50 to 100 and the slope (A) becomes very small, approaching zero. This reduced slope indicates that there is a reduction in the relative shear in this outer region. Further, the present results show the values of B get larger for thick axisymmetric boundary layers and the value of B increases with increasing speed. This increase in the value of B may be an indication of the distance from the wall where the log region begins. In other words, it may be an indication that the viscous inner region extends further into the flow as the boundary curvature increases as indicated by Rao (1) and the shear balance discussed previously.

6.2 Boundary Layer Thickness

The mean axial velocity data is analyzed to evaluate the thickness characteristics of the boundary layer. This section will present three methods used to evaluate the boundary layer thickness. These three methods, which are described in the following subsections, are based on the mean axial velocity field, the RMS axial velocity fluctuation field and the curvature of the mean velocity profile.

6.2.1 Boundary Layer Thickness Determined from the Axial Velocity Field

The boundary layer thickness is defined as the radial distance from the boundary surface to the location in the flow where the axial fluid velocity reaches a chosen small percent of the towing speed. For the filament experiment, the inter-pulse timing of the SPIV system was selected to resolve the small velocities in the outer boundary layer region down to 0.001 of the towing speed (Refer to Appendix D: Stereo Particle Image Velocimetry System Specifications). Therefore, regions in the flow with a velocity of 0.005 times the towing speed or greater were considered to be part of the boundary layer. The analysis procedure involves resolving the total area in the field over which the fluid velocity is larger than or equal to 0.005 times the towing speed and defining an equivalent radius for that area to represent the effective boundary layer thickness.

The total area, A_T, corresponding to the boundary layer flow is calculated as the number of vectors with velocity greater than or equal to $0.005U_{tow}$ multiplied by the cross sectional area corresponding to each vector, A_n = 2.38 times 2.38 mm^2. Since the boundary layer flow is assumed to be axisymmetric, an equivalent radius, i.e. the boundary layer thickness, is given by (Refer to Figure 30).

$$\delta(x) = \sqrt{\frac{\sum_{n=1}^{N}(A_n)}{\pi}} = \sqrt{\frac{N\,A_n}{\pi}}$$

Equation 32

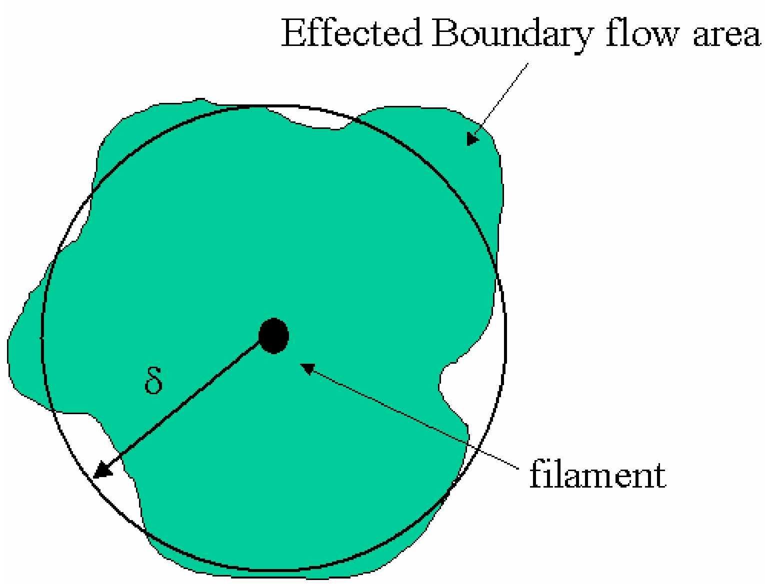

Figure 30: Schematic showing region of boundary layer flow (green, where the velocity is above 0.005 times the towing speed) and the equivalent boundary layer thickness δ. The boundary layer thickness was calculated to be equivalent to the effective radius of the boundary flow area.

The boundary layer thickness values are calculated at each axial location for all speeds and conditions. The results are shown in Figure 31 for both filament diameters.

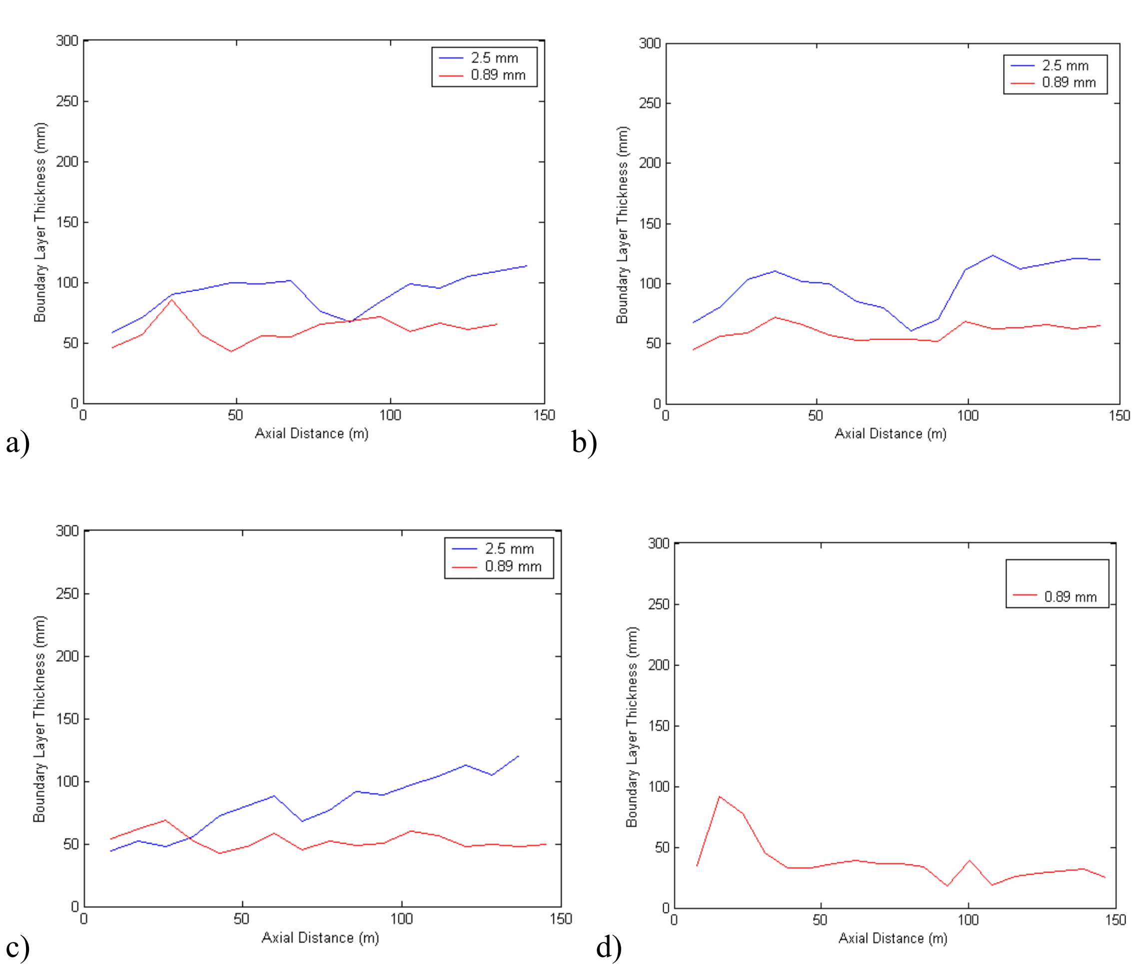

Figure 31: Boundary Layer Thickness vs Axial Location. The boundary layer thickness value fluctuates along the length of the cylinder. a) 3.8 m/s b) 7.7 m/s c) 12.8 m/s d) 15.4 m/s

The data shows that the boundary layer thickness exhibits a periodic relaxation in growth along the length of the cylinder and that the boundary layer thickness is larger on the larger diameter cylinder. This periodic relaxation was observed at all speeds and is consistent with the relaxation found in the boundary layer profiles (Section 6.1 Boundary Layer Profiles) where it was shown that the mean axial velocity profiles did not develop monotonically but showed recurring near-wall changes in slope and fullness. The area-based boundary layer thickness calculations reported in this subsection show that the cross sectional area of the boundary flow volume also exhibits a relaxation with axial distance.

These results show that the boundary layer thickness values are larger for the larger diameter filaments for all speeds, as previously stated. Considering the filament diameters, the amount of exposed surface area is 2.8 times larger for the larger filament. This suggests that the boundary layer growth for thick axisymmetric boundary layers is largely a function of length and the available surface area, i.e. length times circumference. However, the small diameter filament reaches considerably larger δ/a ratios than the larger diameter filament for similar lengths. For example, in Figure 31 b, the ratio of δ/a at the trailing edge of the filament is approximately 90 for the 2.5-mm line and 140 for the 0.89-mm line. The ratio δ/a can be considered a measure of the effectiveness with which momentum is transferred to the outer fluid. Relating δ to the volume of the effected boundary flow and a to the amount of available surface area generating momentum flux, the smaller diameter line reaches a larger number of cylinder radii into the flow. Therefore, momentum transfer to the outer fluid becomes more effective as the transverse curvature of the boundary becomes more severe.

6.2.2 Boundary Layer Thickness Determined from RMS Axial Velocity Fluctuation Fields

An analysis of velocity fluctuations provides additional information about the extent of the boundary layer flow region (Chapter 7 will present the turbulent velocity fluctuation results.) It was initially considered that the cylinder boundary layer would extend from the boundary to the location in the flow where the fluctuations fall off to ambient levels. It should be kept in mind that ambient levels include the turbulence in the wake of the strut alone. Therefore, the magnitudes of the velocity fluctuations in the boundary layer flow must be compared to those occurring in the strut wake. Curves of the RMS axial velocity fluctuation versus radius in the boundary layer of the cylinder and in the wake of the strut alone are shown in Figure 32. As can be seen from the figure, the RMS axial velocity fluctuation levels in the cylinder flow field (red) are significantly larger than in the strut wake (blue) near the cylinder. However, though these levels diminish with radial distance, they do not reach ambient levels within the field of view of the SPIV measurements.

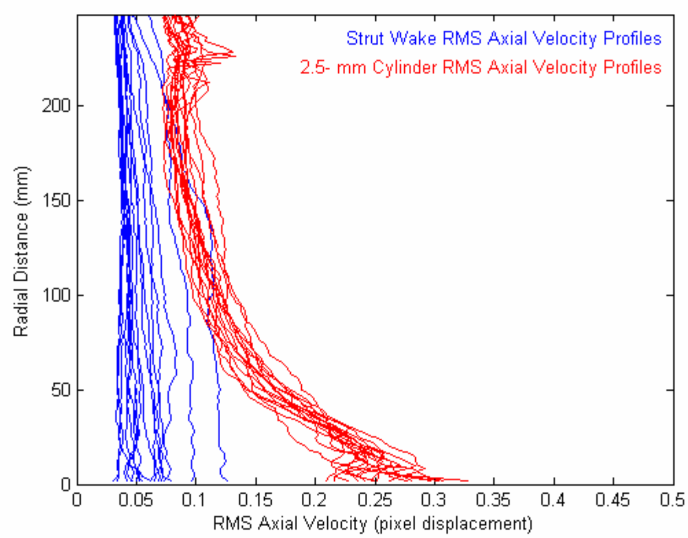

Figure 32: RMS axial velocity fluctuations. The RMS axial velocity fluctuations expressed in pixels versus radial distance for the wake of the strut (blue) and the boundary layer of the cylinder (red) are plotted for all planes along the cylinder. The profiles indicate that the cylinder flow has an elevated fluctuation level compared to the strut wake flow.

It was mentioned in Chapter 2 that turbulent energy in the background flow is effected by the presence of thick axisymmetric boundary layers, $\delta/a>20$. This influence on the background flow is likely happening in the present experiment since it appears that the level of turbulence in the outer flow region when the cylinder is present is elevated relative to the values with the strut wake alone. Therefore, the above approach does not provide a distinct location defining the outer edge of the boundary layer.

6.2.3 Boundary Layer Thickness Determined from the Curvature of the Mean Axial Velocity Profile

An alternate measure of the boundary layer thickness at each axial location was taken to be equal to the radial distance from the cylinder surface where the curvature of the mean axial velocity profile is zero. This location was determined by analyzing the second derivative of the velocity profiles using a second order accurate central differencing scheme shown below:

$$\bar{u}_i'' = \frac{\bar{u}_{i+1} - 2\bar{u}_i + \bar{u}_{i-1}}{dr^2} + O(dr^2)$$

Equation 33

This discrete numerical formulation results in a jagged distribution of the curvature with no single clear location where the derivative is distinctly zero. Therefore, a logarithmic curve was fitted to the distribution of the curvature values using a least squares method and the radial distance from the cylinder surface to the zero crossing of this curve was taken as the boundary layer thickness. The analysis for U= 3.8 m/s and d= 0.89-mm is shown in Figure 33. For clarity of presentation, each profile is offset by 0.02 in the y direction from the previous profile. The logarithmic curve fits are plotted on top of the difference values determined from the numerical approximation. Figure 34 shows the resulting boundary layer thickness as a function of axial position.

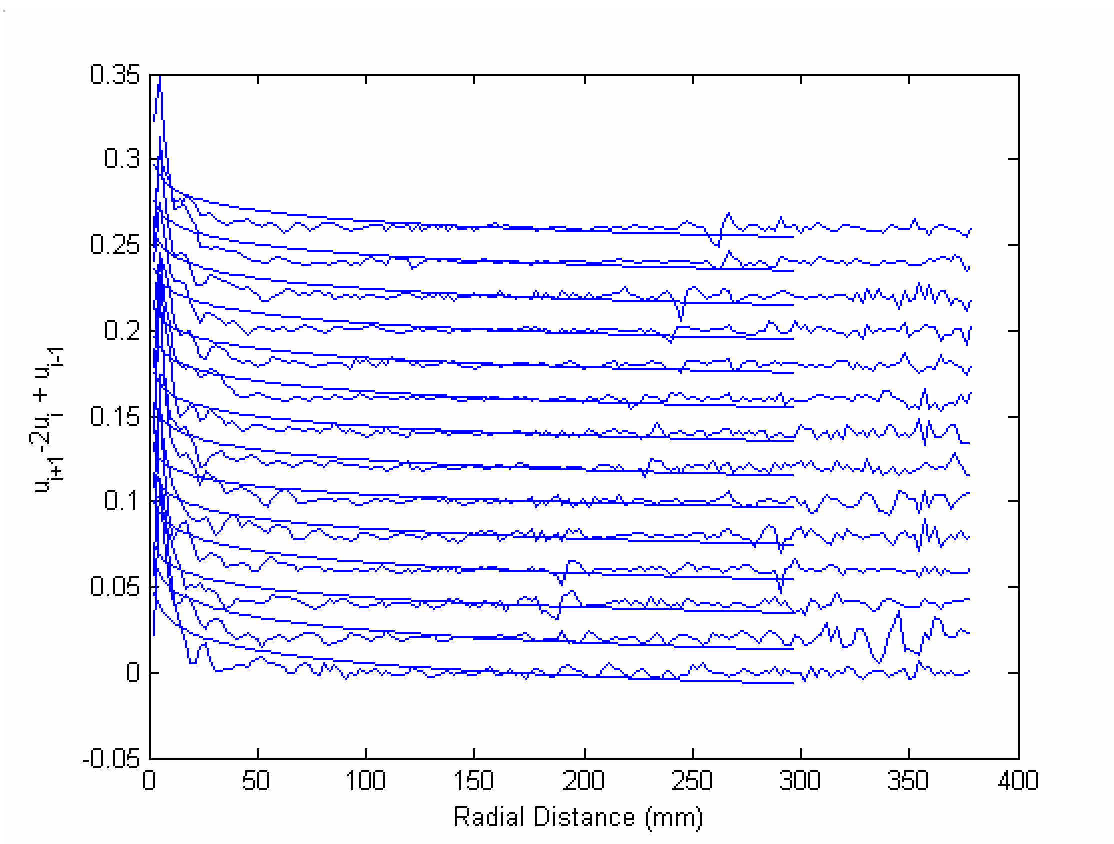

Figure 33: Second Derivative of the Velocity Profile vs Radial Location. The second derivative of the velocity profile was evaluated using Equation 32 (jagged curves). Each profile is plotted with an offset relative to the previous profile. A logarithmic curve was fitted to the data using a least squares method (smooth lines) to estimate the radial position where the curvature goes to zero. This radius was taken as the boundary layer thickness.

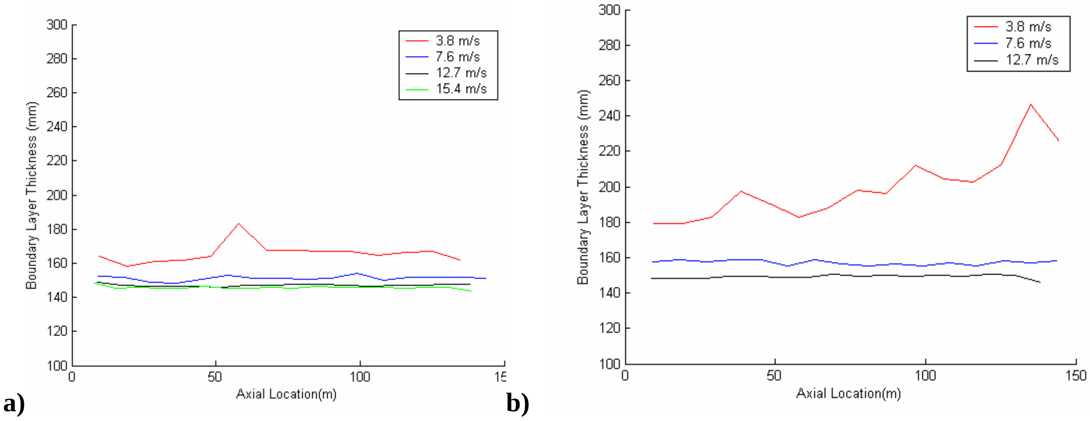

Figure 34: Boundary Layer Thickness Estimate using the Second Derivative of the Mean Axial Velocity. These curves illustrate how the characteristic boundary layer thickness defined using the second derivative technique changes with axial location. The boundary layer thickness becomes thinner with increasing speed for both cylinder diameters tested. a) 0.89 mm b) 2.5 mm

The boundary layer thickness values are larger in magnitude when compared to the values determined using the equivalent radius method (Section 6.2.1 Boundary Layer Thickness Determined from the Axial Velocity Field) and the values do not exhibit significant growth along the length of the cylinder. Also, Figure 34 shows that using this curvature method, there is a trend of decreasing boundary layer thickness with increasing speed and decreasing cylinder radius.

6.3 Boundary Layer Profiles Scaled using Outer Variables

The boundary layer profiles can also be scaled using the outer variable $\delta(x)$. For the outer region of planar boundary layers, the relationship between the local velocity defect, $(U_o-\bar{u})$, divided by the wall shear velocity and the distance from the wall divided by the local boundary layer thickness is expressed as follows:

$$\frac{(U_o - \overline{u})}{u_\tau} = (\frac{-1}{\kappa})\ln(\frac{y}{\delta}) + 2.5$$

Equation 34

where U_0 and $\bar{u}$ are the free stream and local mean velocities relative to the fixed flat plate, respectively. (The minus sign in front of the log term is due to the change in reference frame relative to Equation 28.)

In applying this equation to the filament boundary layer data, the measured mean axial velocity (equivalent to U_0-$\bar{u}$ in the above equation) is scaled with u_τ and the radius is scaled with the boundary layer thickness $\delta(x)$ determined as the equivalent radius where the mean axial velocity was greater than 0.005 times the towing speed, see Subsection 6.2.1 (Figure 31). The scaled profiles are shown in Figure 35 a through g for towing speeds ranging from 3.8 m/s to 15.2 m/s. As can be seen from the plots, the logarithmic portion of the profiles does not collapse to a single curve. This is attributed to the relaxation in the boundary layer which results in a fluctuating boundary layer thickness and wall shear with distance along the filament. Also, the wall shear stress used in the present study is an average value obtained from the total drag on the cylinder rather the local value.

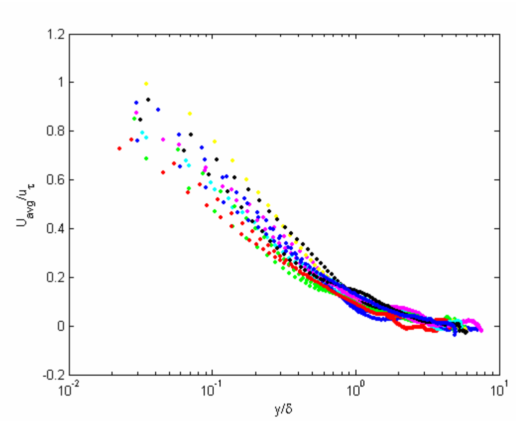
U_avg/u_τ
y/δ
1.2
1
0.8
0.6
0.4
0.2
0
-0.2
10^-2
10^-1
10^0
10^1
a)

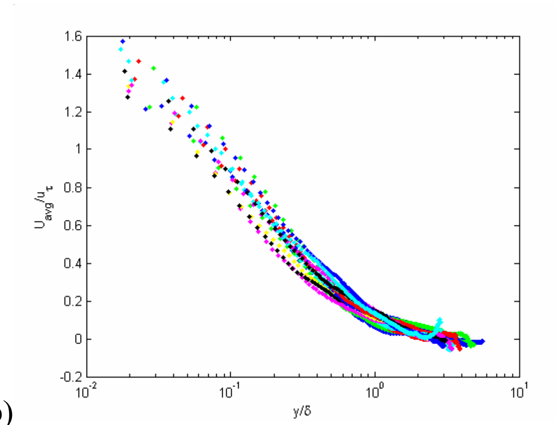
U_avg/u_τ
y/δ
1.6
1.4
1.2
1
0.8
0.6
0.4
0.2
0
-0.2
10^-2
10^-1
10^0
10^1
b)

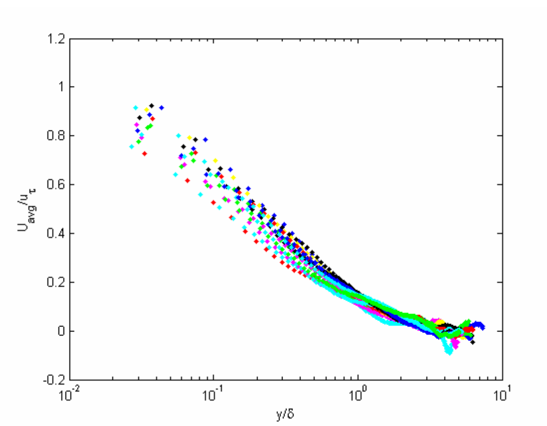
U_avg/u_τ
y/δ
1.2
1
0.8
0.6
0.4
0.2
0
-0.2
10^-2
10^-1
10^0
10^1
c)

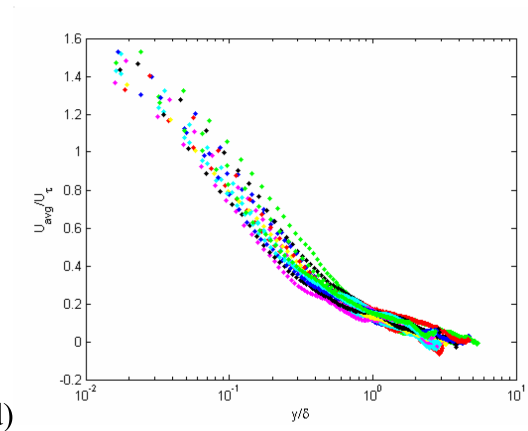
U_avg/U_τ
y/δ
1.6
1.4
1.2
1
0.8
0.6
0.4
0.2
0
-0.2
10^-2
10^-1
10^0
10^1
d)

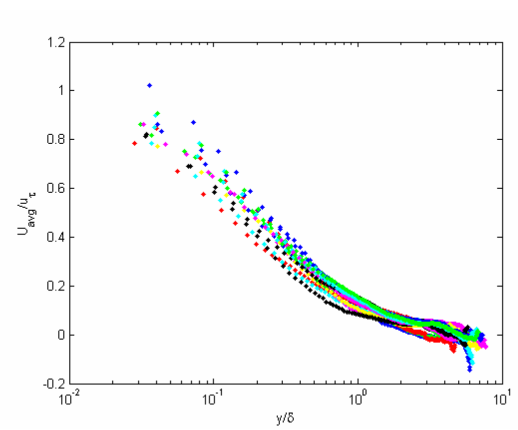
U_avg/u_τ
y/δ
1.2
1
0.8
0.6
0.4
0.2
0
-0.2
10^-2
10^-1
10^0
10^1
e)

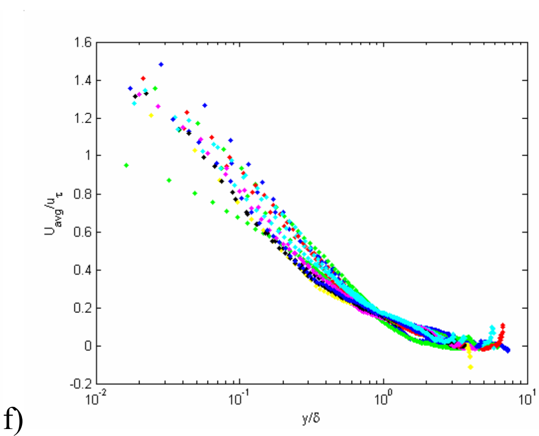
U_avg/u_τ
y/δ
1.6
1.4
1.2
1
0.8
0.6
0.4
0.2
0
-0.2
10^-2
10^-1
10^0
10^1
f)

g) 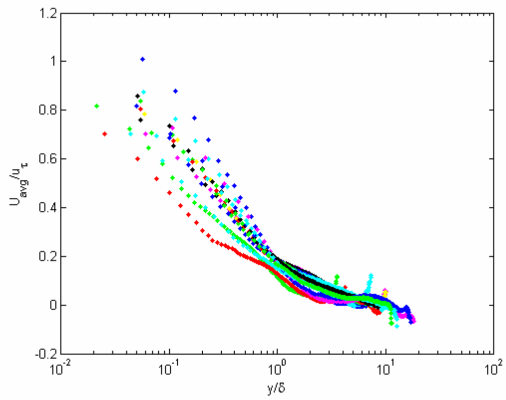

Figure 35: Outer Scaling of the Mean Axial Velocity profiles. The mean axial velocity profile is nondimensionalized with the wall shear velocity and the distance from the boundary is nondimensionalized with the boundary layer thickness. The slopes of the curves in the logarithmic region show dependence on the cylinder diameter. a) 3.8 m/s 0.89 b) 3.8 2.5 mm c) 7.7 m/s 0.89 mm d) 7.7 m/s 2.5 mm e) 12.8 m/s 0.89 mm f) 12.8 m/s 2.5 mm g) 15.4 0.89 mm

In spite of these difficulties, averaged curve fits were determined for the data in the log region of the profiles and the resulting values of the slope, A, and offset values, B, are shown in Table 11. The values of *A* are approximately the same as those determined with inner scaling paramters. (The change in sign is due to the change in reference frame).

Table 11: Profile fits for the 0.89 and 2.5 mm lines in Mixed Variables

Speed (m/s)	**0.89mm**		**2.5mm**	
	A	B	A	B
3.8	-.21	0.08	-.34	0.06
7.6	-.22	0.11	-.32	0.07
12.7	-.23	0.10	-.32	0.11
15.2	-.22	0.16		

For comparison, velocity defect profiles for axisymmetric boundary layers on fixed cylinders with diameters from 1 inch to .01 in and δ/a values as large as 42 are shown in Figure 36. The x-axis is the non-dimensionalized velocity deficit, $(\bar{u}-U_0)/u_\tau$ and the y-axis is the scaled radial distance y/δ. The sign of the velocity term is negative for this figure and positive for Figure 35 by definition of the terms.

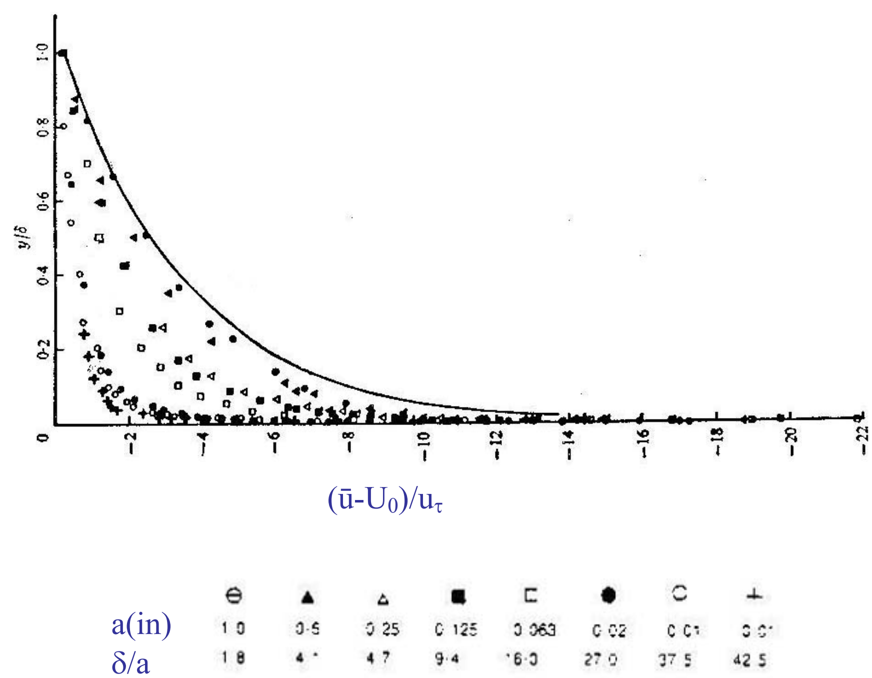

Figure 36: Velocity Defect Profiles reprinted from Lueptow, R., "Turbuent Boundary Layer on a Cylinder in Axial Flow", NUSC Technical Report 8389, Sept. 1988. (12). This graph demonstrates the influence of transverse curvature on boundary layer profiles. The high shear region becomes thinner as the boundary layers become thicker for cases with high transverse curvature.

For the current experiment, the inner-most measurement occurs at a non-dimensional distance of approximately y/δ of 0.02 and non-dimensional velocities of $\bar{u}/u_\tau$ of 1.4 for the 2.5-mm cylinder and 0.8 for the 0.89-mm cylinder, respectively (see Figure 35). These velocity values agree with the trend indicated on Figure 36. The figure indicates that as δ/a increases, $\bar{u}/u_\tau$ decreases at a given y/δ and therefore indicates that the high shear region gets thinner. It should be noted that the measurements for the present experiment are taken in the outer 98% of the boundary layer and that there were no measurements in the very high shear region adjacent to the wall.

6.4 Displacement and Momentum Thicknesses as a function of Axial Location

Additional characteristic boundary layer parameters were calculated from the averaged boundary layer velocity profiles. The displacement thickness and momentum thickness values were calculated to resolve the length scales related to the mass and momentum fluxes associated with the boundary layer flow.

The displacement thickness, δ^*, is defined as the distance that streamlines just outside the boundary layer are displaced due to the presence of the boundary layer. This value is associated with the change in mass flux caused by the presence of a viscous boundary layer when compared to an equivalent inviscid flow. The displacement thickness is related to the change in mass flow through the following relationship (Cipolla et. al..):

$$\delta^{*2} + 2a\delta^* = 2\int_a^{a+\delta} \left(1 - \frac{\overline{u}(r)}{U_0}\right) r\, dr$$

Equation 35

This can be rearranged into the normal quadratic equation form in terms of δ^*

$$\delta^{*2} + 2a\delta^{*} - 2\int_{a}^{a+\delta}(1 - \frac{\bar{u}(r)}{U_0})\, r\, dr = 0$$

Equation 36

The solution to this quadratic equation is

$$\delta^{*} = \frac{-2a \pm \sqrt{4a^2 + 4I}}{2}$$

Equation 37

where I is the right side of Equation 35.

The momentum thickness was determined by solving the quadratic expression relating θ and the integrand evaluating the change in momentum (Equation 15.) which can be written as the following quadratic expression,

$$\theta^2 + 2a\theta - 2\int_{a}^{a+\delta} \frac{\bar{u}(r)}{U_\infty}\left(1 - \frac{\bar{u}(r)}{U_\infty}\right) r\, dr = 0$$

Equation 38

This can be solved using the quadratic formula as described previously. Figure 37 shows the displacement thickness and the momentum thickness results for both cylinders at speeds of 3.8, 7.7, 12.8, and 15.4 m/s (7.5, 15, 25 and 30 knots).

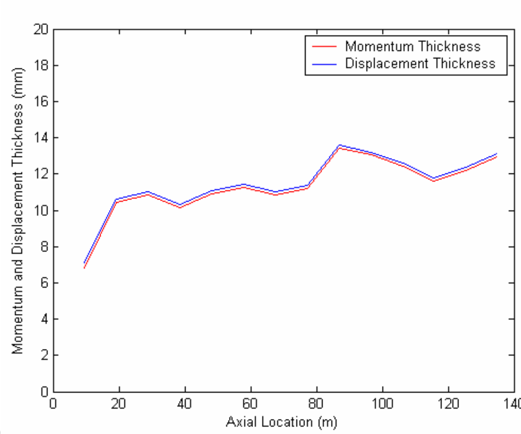
Momentum Thickness
Displacement Thickness
Momentum and Displacement Thickness (mm)
Axial Location (m)
a)

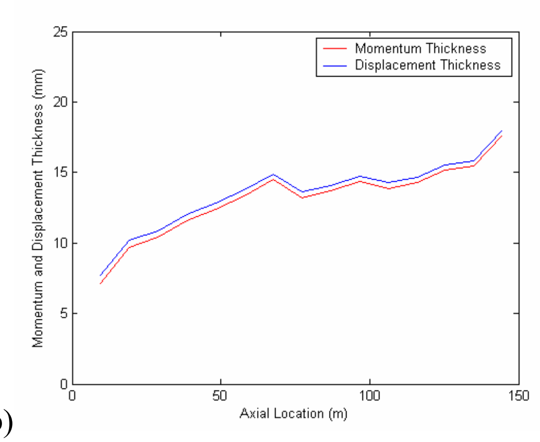
Momentum Thickness
Displacement Thickness
Momentum and Displacement Thickness (mm)
Axial Location (m)
b)

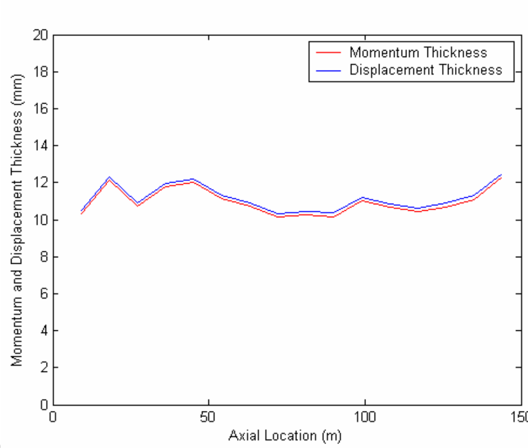
Momentum Thickness
Displacement Thickness
Momentum and Displacement Thickness (mm)
Axial Location (m)
c)

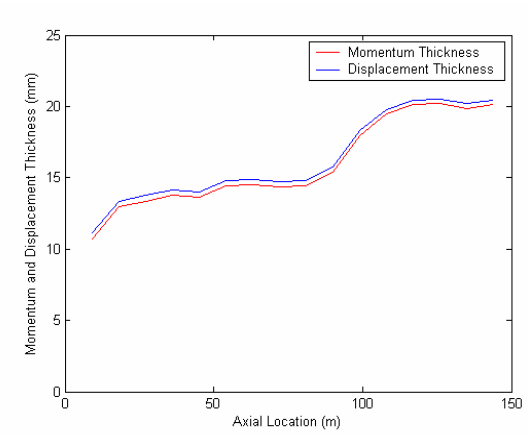
Momentum Thickness
Displacement Thickness
Momentum and Displacement Thickness (mm)
Axial Location (m)
d)

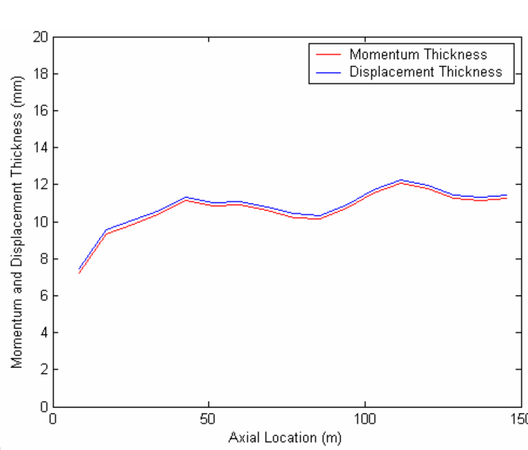
Momentum Thickness
Displacement Thickness
Momentum and Displacement Thickness (mm)
Axial Location (m)
e)

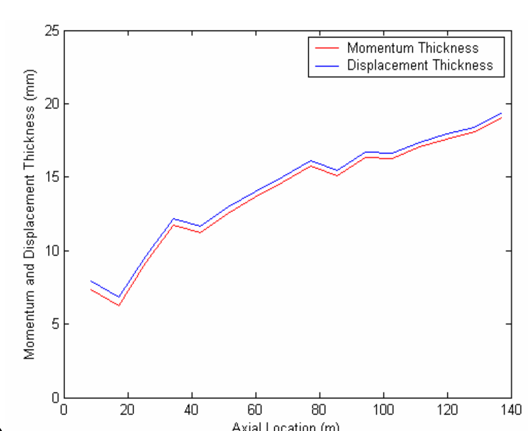
Momentum Thickness
Displacement Thickness
Momentum and Displacement Thickness (mm)
Axial Location (m)
f)

g) 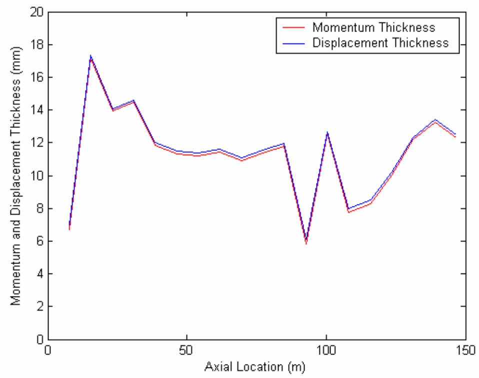

Figure 37: Displacement and Momentum Thickness versus Axial Location. The displacement and momentum thickness exhibit periodic relaxations along the length of the filament as seen in the boundary layer thickness development. Momentum thickness values are comparable to the momentum thickness values calculated from the drag results. a)U= 3.8 m/s d=0.89-mm b) U=3.8m/s d= 2.5-mm c) U=7.7 m/s d=0.89-mm d) U=7.7 m/s d=2.5-mm e) U=12.8 m/s U=0.89-mm f) U=12.8 m/s d=2.5-mm g) U=15.4 m/s d=0.89 mm

The 0.89-mm-diameter cylinder produces smaller displacement and momentum thickness values at a given velocity and length when compared to the 2.5-mm diameter cylinder. The displacement thickness calculations are consistently larger than the momentum thickness values, as expected. The momentum thickness values agree well with the momentum thickness values calculated from the drag data (Refer to Table 5 and Table 6). These displacement and momentum thickness results exhibit a similar growth characteristic to the development of the boundary layer thickness shown in Section 6.2.1. This is not unexpected since these techniques are all integral methods.

6.4 Discussion

The analysis of the averaged velocity data reveals periodic changes in the development of the boundary layer flow along high aspect ratio flexible cylinders. The axial development of the averaged velocity profiles reveal periodic relaxations occurring in the near wall high shear flow. Relaxation is also evident in the outer flow as seen in the boundary layer thickness, displacement thickness and momentum thickness values. Ratios of the boundary layer parameter values provide a criteria for comparison to known flow geometries.

The parameters for laminar and turbulent flat plate boundary layers are explicitly known. For a laminar boundary layer, the Blasius flat plate solutions are:

$$\delta(x) = \frac{5.2x}{\sqrt{\mathrm{Re}_x}} \qquad \delta^*(x) = \frac{1.721x}{\sqrt{\mathrm{Re}_x}} \qquad \theta(x) = \frac{0.664x}{\sqrt{\mathrm{Re}_x}}$$

Comparing these relationships, the ratios of these parameters are $\delta^*/\delta = 0.33$, $\theta/\delta=0.13$ and $\delta*/\theta=2.53$. From Schlichting (22) turbulent flat plate boundary layer relationships are:

$$\delta = 0.37x\left(\frac{U_\infty x}{\upsilon}\right)^{\frac{-1}{5}} \qquad \delta^* = \frac{\delta}{8} \qquad \theta = \frac{7}{72}\delta$$

These result in the parameter ratio values of $\delta^*/\delta = 0.125$, $\theta/\delta=0.09$ and $\delta*/\theta=1.28$. For the present set of data, the ratios were determined for each axial location and then averaged over the length for each condition due to the fluctuating nature of the parameters. The averaged values for the 0.89-mm and 2.5-mm cylinders are shown in Table 12. The ratios of the boundary layer parameters indicate that the axisymmetric boundary layer flow is fundamentally different from the flat plate flow.

Table 12: Ratio of displacement and momentum thickness to boundary layer thickness for small diameter lines.

Speed (m/s)	0.89 mm	0.89 mm	0.89 mm	2.5 mm	2.5 mm	2.5 mm
	$\delta*/\delta$	θ/δ	$\delta*/\theta$	$\delta*/\delta$	θ/δ	$\delta*/\theta$
3.7	**0.19**	**0.18**	**1.02**	**0.15**	**0.14**	1.04
7.7	0.19	0.18	1.02	0.17	0.16	1.03
12.7	0.21	0.20	1.02	0.18	0.17	1.03
15.4	0.33	0.32	1.02			

The displacement thickness to boundary layer thickness ratio for the filament boundary layers is smaller than the laminar ratio and larger than the turbulent ratios for the flat plate. The momentum thickness to boundary layer thickness ratio for the filament is larger than both the laminar flat plate boundary layer ratio and the turbulent flat plate boundary layer ratio. The shape factor ($\delta*/\theta$) for the axisymmetric boundary layer is close to 1, this indicates that the mass and momentum fluxes are affecting similar volumes. This value is significantly smaller than the Blasius solution and close to the turbulent flat plate value. Therefore, the boundary flow over a high aspect ratio filament develops a relationship between the mass and momentum fluxes similar to the turbulent flat plate boundary layer. However, these values are very different in relation to the overall boundary layer thickness.

CHAPTER 7: FLUCTUATING VELOCITY COMPONENTS

The Root-Mean-Square (RMS) velocity fluctuation values are evaluated in the wake of the strut and in the boundary layers of the flexible cylinders. The differences between the RMS velocity fluctuation levels in the strut wake and in the boundary layer of the cylinder are considered to be due to the presence of the cylinder boundary layer. These fluctuation velocities are evaluated and averaged to produce a turbulent velocity profile for each condition and axial location. One of the goals of these measurements is to determine if the boundary layer remains turbulent over the extent of the filament.

7.1 RMS Fluctuation Profiles

At each axial location, the distribution of the RMS values of the axial, radial and azimuthal velocity components (u', u'_θ, u'_r, respectively) were computed using the methods described in Chapter 5. This data was then azimuthally averaged about the cylinder using the techniques described in the previous chapter to obtain the profiles of these RMS quantities versus radial distance from the cylinder.

A sample plot of the three RMS velocity fluctuation components versus radial distance at one axial distance along the cylinder is shown in Figure 38 for the case with U= 3.8 m/s and d= 2.5-mm At each radial position, the RMS axial velocity component is consistently larger than u_r' and u_θ'. The curves of u_r' and u_θ' decrease more or less monitonically with radial distance. The curve of u' at first increases, reaches a peak at small r and then falls off monitonically with increasing r.

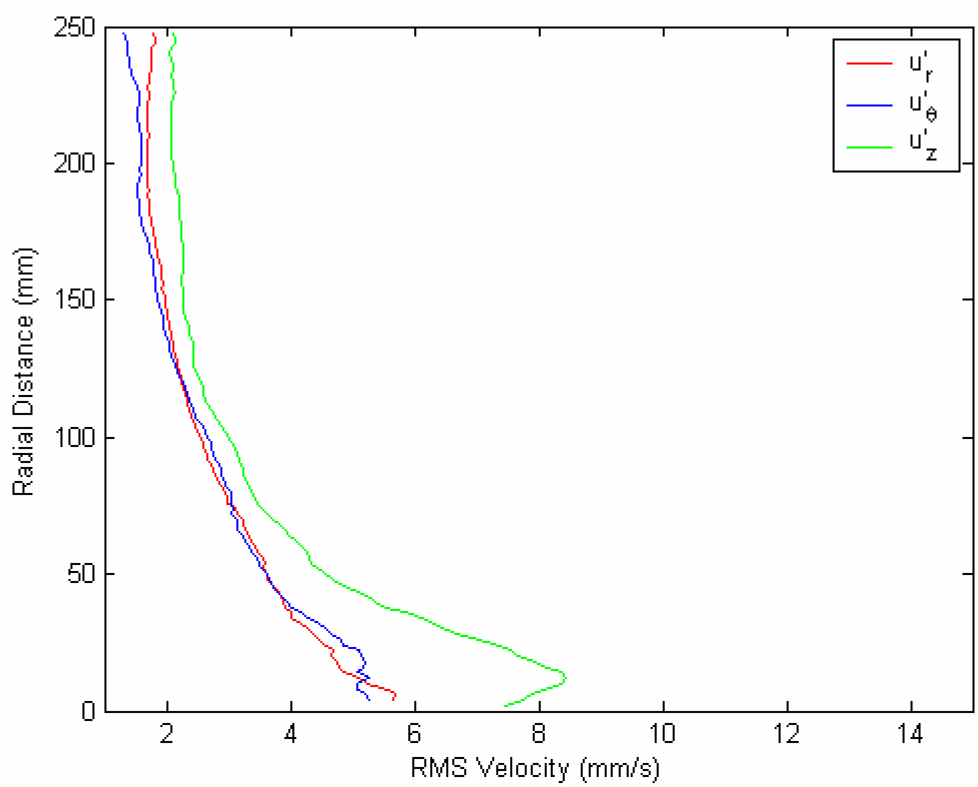

Figure 38: Velocity Fluctuation Profiles. The fluctuating velocity profiles are shown for the towing speed of 3.8 m/s and cylinder diameter of 2.5-mm. The axial, radial and azimuthal fluctuating velocity components are shown as a function of distance from the cylinder.

In the following, the axial velocity fluctuation profiles are analyzed in order to characterize and compare the turbulent boundary layers for the various run conditions. Axial fluctuating velocity profiles for the strut wake and the strut wake with the 2.5-mm cylinder are shown in Figure 39 for a towing speed of 3.8 m/s (7.5 knots). The axial fluctuating velocity magnitudes are consistently larger for the cylinder flow than for the strut wake alone.

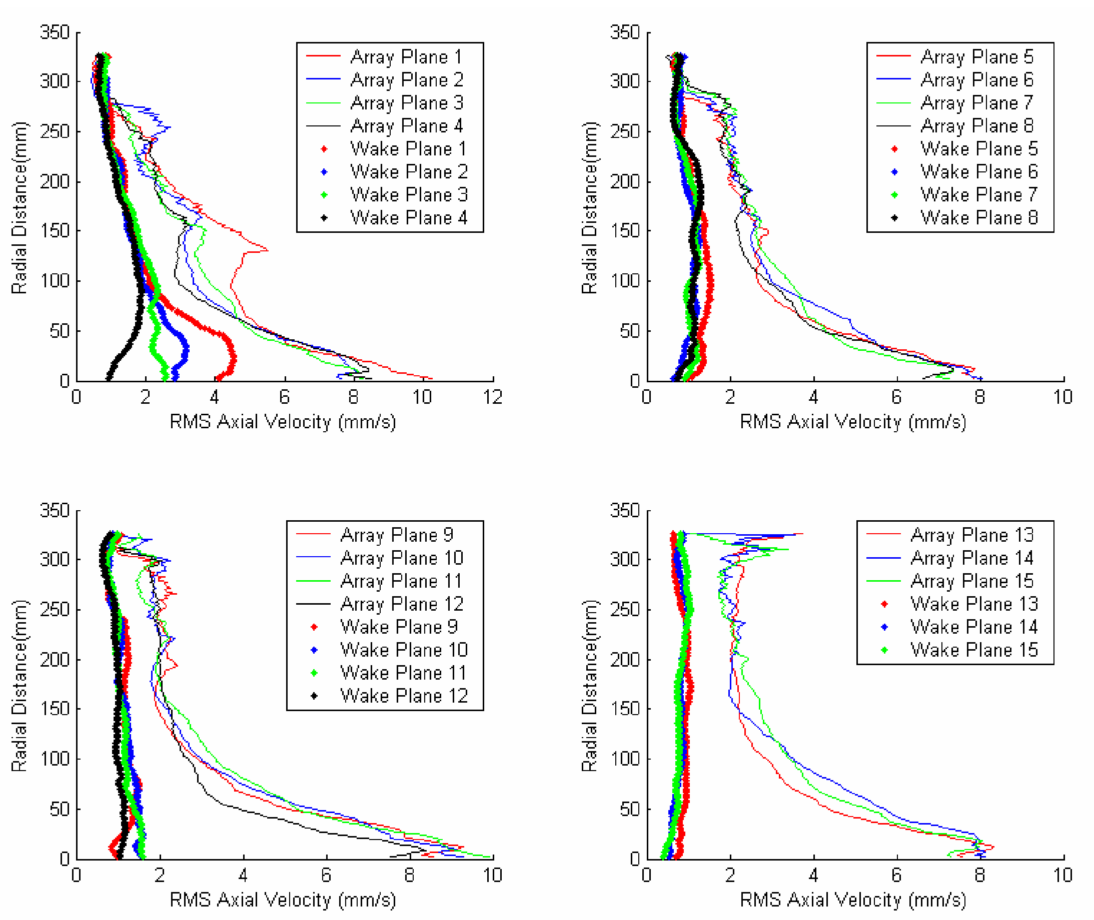

Figure 39: RMS Axial Fluctuating Velocity Profiles. The axial velocity fluctuations for the wake flow and the cylinder flow are plotted together for the averaged planes evaluated along the length of the filament. The fluctuations in the cylinder flow are significantly larger than those in the wake for all axial locations. Towing speed is 3.7 m/s and the filament diameter is 2.5-mm.

The profiles for the wake flow in planes 1 and 2 indicate that there is an increased level of axial turbulent fluctuations near the center of the wake compared to the periphery. This is considered to be due to the towpoint fairing on the bottom of the strut. For planes 3 to 15, the velocity fluctuation levels in the strut wake are relatively constant across the region of interest. For all speeds, the ratio of the maximum axial turbulent velocity fluctuation to the towing speed is on the order of or less than 0.1% throughout the wake (see Appendix H: Fluctuating Velocity Profiles). However, the ratio of the maximum axial fluctuation velocity to the shear velocity (u'/u_τ) is on the order of 0.05. For a flat plate at an equivalent distance (y+ of approximately 500) that ratio is close to 1 (23). Therefore, the fluctuations in the axisymmetric boundary layer are comparatively smaller than those in a flat plate boundary layer.

The fluctuating velocity profiles determined for the flow-fields with the filament illustrate that the fluctuations approach wake values far from the boundary. Near the cylinder, at radial distances below 50 to 100 mm, the fluctuations are significantly larger in the filament profiles than in the strut wake profiles. The turbulent velocity fluctuations in the filament boundary flow are on the order of 10 times larger than those in the strut wake. This turbulent region becomes more distinct in the downstream profiles.

As previously stated, the fluctuation velocities fall off in magnitude with distance from the filament, and the values approach wake magnitudes. However, for the majority of the results, the velocity fluctuation values in the filament profiles do not actually reach the wake values. The results from Chapter 6 for the boundary layer thickness quantities indicate that the outer most measurements are outside the boundary layer. As previously mentioned, cylinders with thick boundary layers are effective in converting mean flow energy into turbulent energy. This could account for the elevated values determined outside the boundary layer. However, it should be kept in mind that the average velocity fluctuation distributions are determined for a cylinder that is moving through the wake flow. This processing method may affect the average values utilized to evaluate the fluctuation quantities, and particularly, may effect the values in the outer edges of the boundary layer.

In summary, there is a consistent increase in the axial turbulent velocity fluctuations near the cylinder for all speeds and axial locations. This is an indication that the boundary layer flow remains turbulent over the entire length of the cylinder.

7.2 Maximum in Turbulent Velocity Profile

Several of the turbulent velocity profiles determined for the cylinder flow contain a maximum fluctuation value that occurs at a finite distance away from the filament. In Figure 39, maxima are evident in planes 2, 3, 7, 8, 9, 12, 13, and 15 at distances from the boundary ranging from 8 mm to 24 mm. When non-dimensionalized, these distances are 1000's of viscous lengths from the cylinder surface

For flat plate boundary layers, a maximum also occurs in the turbulent velocity profile at a finite distance from the boundary. However, it occurs at approximately 15 viscous lengths from the wall. The location of the peak in the velocity fluctuation profile for flat plate boundary layers is the location where turbulence production is maximum. For comparison, the location of the peak turbulence value in the present data was averaged over all the measurement planes for each condition. These values nondimensionalized by the viscous length scale are shown in Table 13.

Table 13: Location of turbulent peak

Speed (m/s)	0.89 mm		2.5 mm	
	Y (mm)	Y^+	Y (mm)	Y^+
3.8	11	1290	13	1352
7.6	5.6	1210	12	2260
12.7	11	3960	12	3780
15.2	14	5880		

As can be seen from the table the physical location is calculated to be the same for most of the conditions. In terms of the SPIV data, a distance of 12-mm from the filament corresponds to 5 measurement locations away from the cylinder. This recurring value for many of the conditions suggests that the peak location may be influenced by physical parameters or data analysis techniques in the experiment.

7.3 Normal Reynolds Stresses and Turbulent Kinetic Energy

The normal Reynolds stresses were evaluated at selected locations to investigate their distribution through the boundary layer and were used to evaluate the turbulent kinetic energy . The normal stress are, of course, the square of the RMS velocity fluctuations discussed to some degree in the previous section. The nondimensionalized normal stresses are defined as:

$$R_{ii} = \frac{\overline{u'_i u'_i}}{u_\tau^{\ 2}}$$

Equation 39

The resulting axial normal stresses are consistently larger than the in-plane (r-θ) normal stresses as shown in Figure 40. The stresses are larger for the larger diameter filament and the magnitudes decrease with increasing speed, as evident in Figure 40 a and b. and Figure 40 a, c, e, and g respectively. Far from the boundary, the three components of normal Reynolds stress approach the same value indicating the turbulence is more isotropic further from the wall.

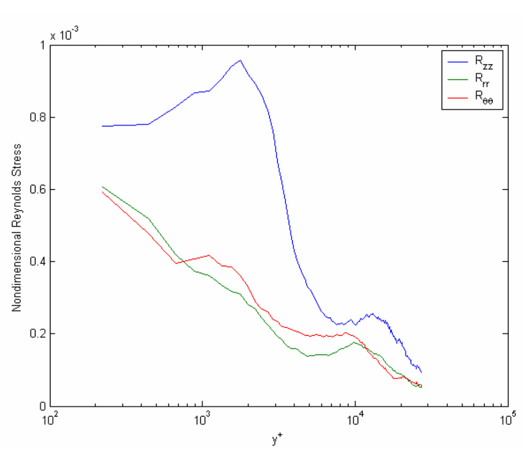

a.

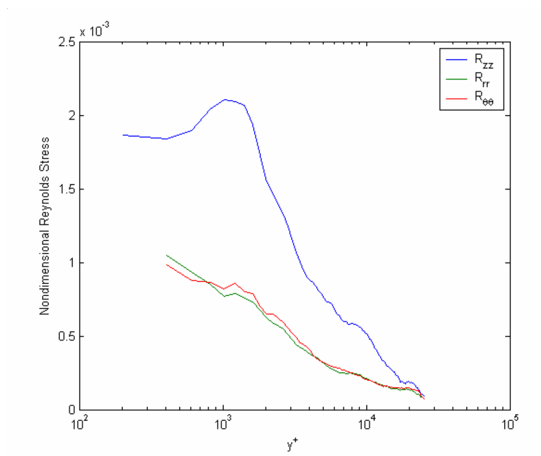

b.

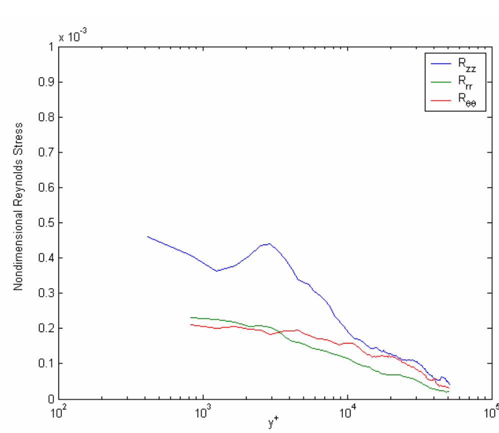

c.

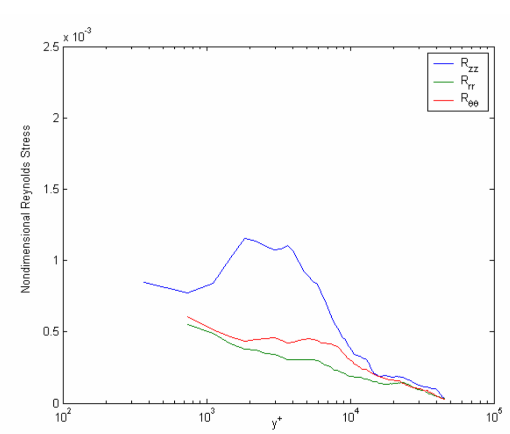

d.

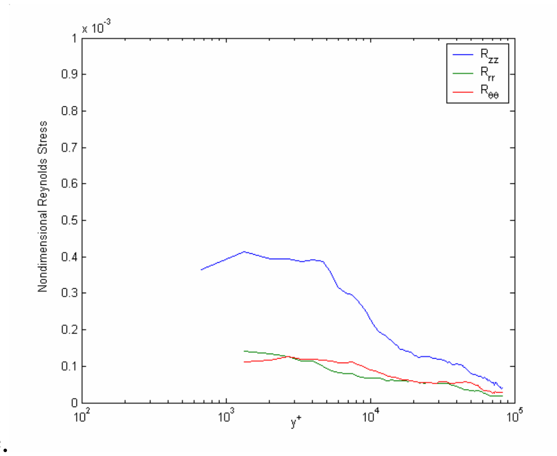

e.

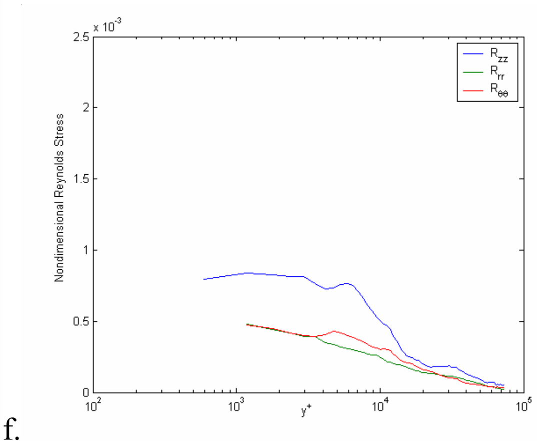

f.

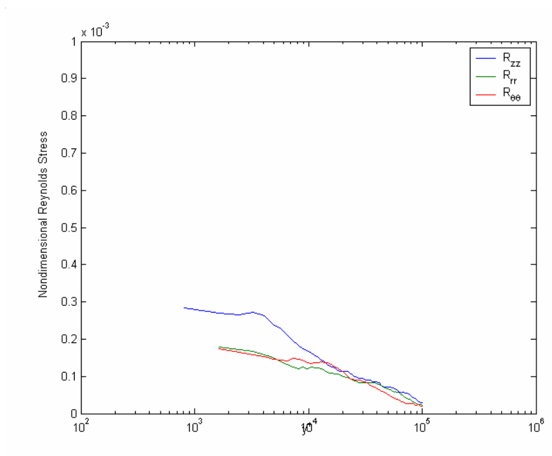

g.

Figure 40: Normal Reynolds Stress distributions. The axial normal Reynolds stress is consistently larger than the in-plane normal stresses. a. U=3.8 m/s d=0.89-mm, b. U=3.8 m/s d=2.5-mm, c. U=7.7 m/s d=0.89-mm d. U=7.7 m/s d=2.5-mm, e. U=12.7 m/s d=0.89-mm f. U=12.7 m/s d=2.5-mm, g. U=15.4 m/s d=0.89-mm.

The wall normal Reynolds stress is of the same order of magnitude as the azimuthal component throughout the measurement region. In wall bounded turbulent flows, the wall normal component is typically damped relative to the other in-plane component. However, Bernard and Wallace (23) illustrate that the in-plane (cross-stream) component values approach the same value for a channel flow at y+ of 500. Also, they indicate the three components approach the same order of magnitude with increasing distance from the wall indicating that the turbulence becomes more isotropic with distance. The current measurements are further from the boundary than the referenced channel flow but they are in agreement with the indicated trends.

Reynolds stresses contribute to the production of turbulent kinetic energy. The turbulent kinetic energy is defined at ½ times the sum of three normal stresses.

$$K^{+} = \frac{\frac{1}{2}(\overline{u_z u_z} + \overline{u_r u_r} + \overline{u_\theta u_\theta})}{u_\tau^{\,2}} = \frac{1}{2}(R_{zz} + R_{rr} + R_{\theta\theta})$$

Equation 40

The nondimensional turbulent kinetic energy (TKE) reduces in magnitude with distance from the boundary as shown in Figure 41. The magnitude increases with increasing diameter and decreases with increasing speed. As for the channel flow discussed by Bernard and Wallace, the TKE is dominated by the axial normal stress near the wall and becomes more isotropic with distance from the wall.

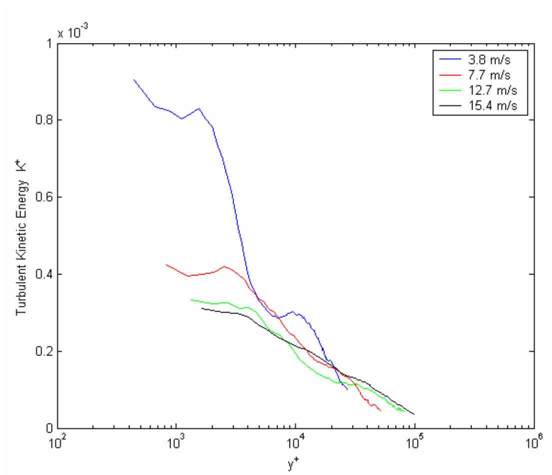

a.

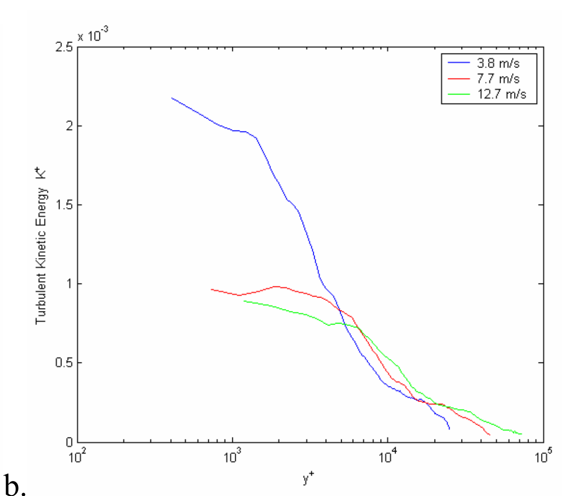

b.

Figure 41: Turbulent Kinetic Energy. The turbulent kinetic energy distribution closely follows the axial Reynolds stress distribution. The magnitude decreases with speed and diameter. a. 0.89-mm filament b. 2.5-mm filament.

7.4 Correlations and Length Scales

The two-point correlation function can be used to evaluate relevant length scales in the flow. The autocorrelation function was evaluated for this flow to characterize the development of the integral scale at each axial location. The normalized autocorrelation function is expressed:

$$F_{zz}(r) = \frac{\overline{u_z'(r_1)u_z'(r_2)}}{\overline{u_z'(r_1)u_z'(r_1)}}$$

Equation 41

where $r=r_2-r_1$. The point r_1 is the reference point about which the correlations are being evaluated. The point r_2 varies throughout the boundary layer. The fluctuations occurring at r_2 are compared to the fluctuations at the reference location r_1 and the ratio is a measure of how well the fluctuations correlate. A correlation value of 1 indicates the values are fully correlated and 0 indicates they are uncorrelated. Correlation functions were evaluated for 3 locations in the flow, r_1=2.38 mm (the innermost measurement location), 11 mm and 22 mm where $r_1 = 0$ is the surface of the cylinder. The correlation functions for U=3.8 m/s and 12.7 m/s for both d=0.89-mm and 2.5-mm evaluated for the r_1= 2.38 mm are shown in Figure 42.

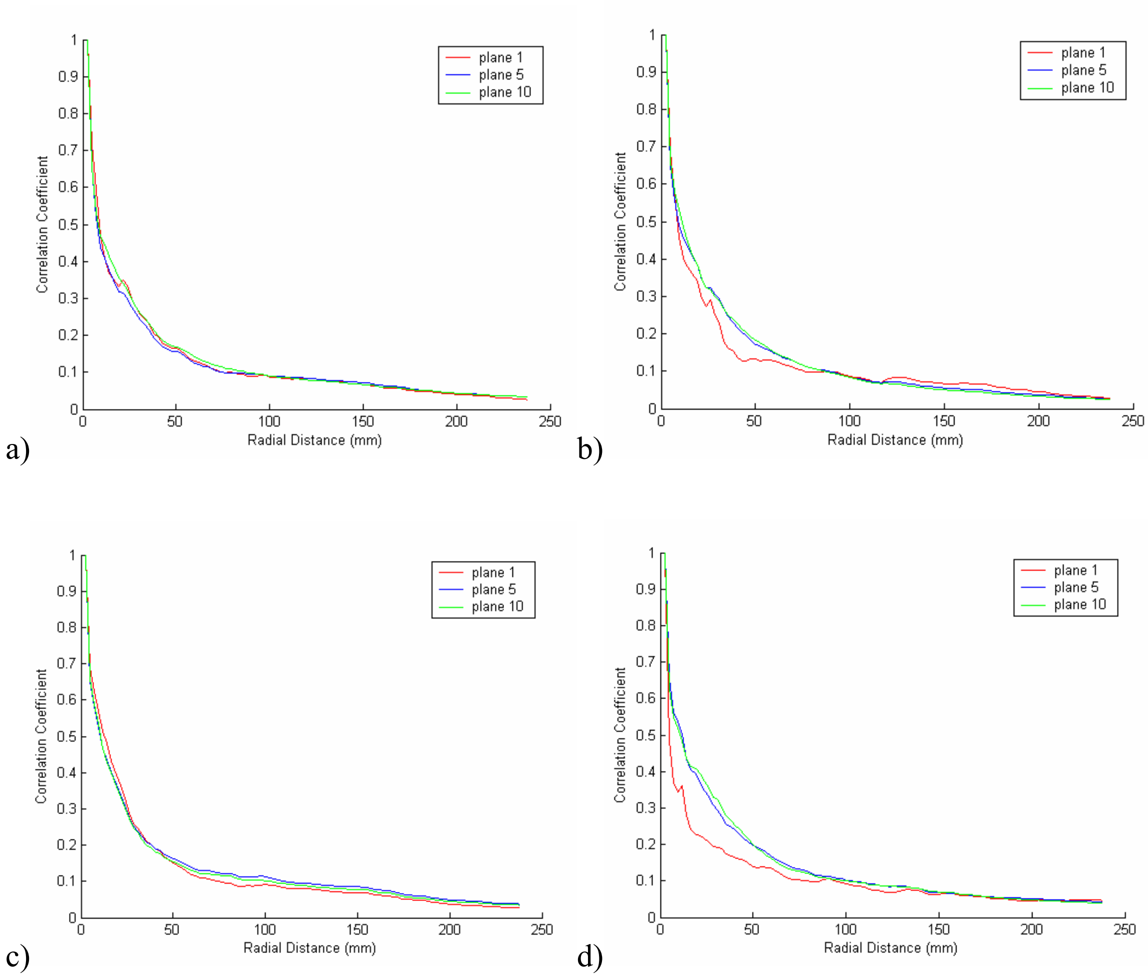

Figure 42: Normalized Correlation Functions (see Equation 41). Normalized correlation function can be used to evaluate characteristic scales in the turbulent boundary layer. A) 3.8 m/s and 0.89 mm B) 3.8 m/s 2.5 mm C) 12.7 m/s 0.89 mm d) 12.7 m/s 2.5 mm.

The corresponding macro length scales are determined by considering the distribution of the auto correlation function. The macro scale, Λ, is determined from the total integral of the correlation function.

$$\Lambda = \int f(r)dr$$

Equation 42

The macro scale is the largest length scale of turbulence occurring in the flow and is an indication of the region over which motions are correlated. Figure 43 shows the axial variation of the macro length scales for the 12.7 m/s 0.89 mm and 2.5mm conditions. The macroscale does change along the cylinder and reaches larger values for the larger diameter cylinder. The fluctuation in the macro scales along the cylinder length can be expected due to the fluctuations in the boundary layer thickness seen previously.

Table 14 shows the averaged macro scales for each run condition and for the three reference points in the flow.

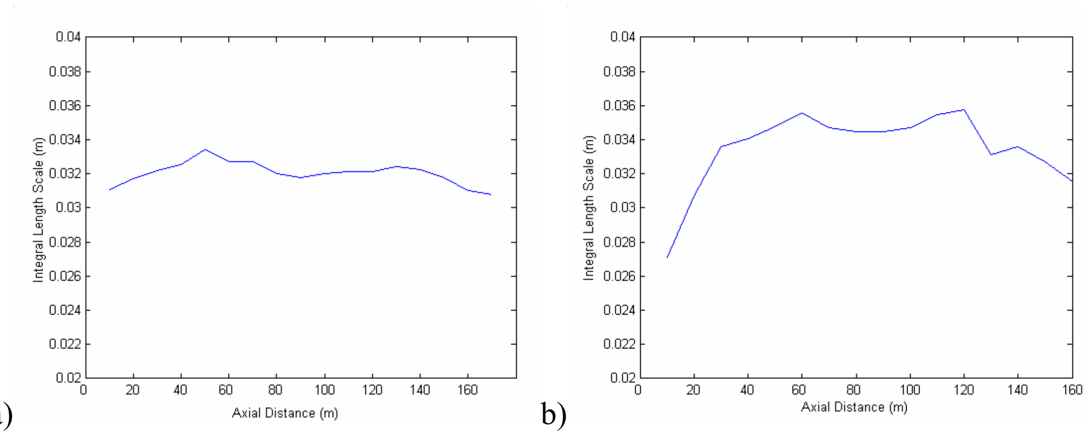

a) b)

Figure 43: Macro Scales versus Axial Location. The macro scale is plotted as a function of distance along the cylinder for the towing speed of 12.7 m/s. a) 0.89 mm b) 2.5 mm.

Table 14: Turbulent length scales determined from the axial correlation function.

Speed (m/s)	Diam (mm)	Λ_{zz} (m) r_{ref} 0mm	Λ_{zz} (m) r_{ref} 11mm	Λ_{zz} (m) r_{ref} 22mm
3.8	0.89	0.031	0.032	0.048
3.8	2.5	0.032	0.028	0.040
7.6	0.89	0.020	0.039	0.046
7.6	2.5	0.040	0.035	0.044
12.7	0.89	0.032	0.041	0.052
12.7	2.5	0.034	0.034	0.044
15.4	0.89	0.046	0.044	0.042

The macro scale tends to increase as the reference point moves further from the boundary. This may be due to the unrestricted eddy motions which occur far from the wall. The calculated macro scales are on the order of the boundary layer thickness values measured. This indicates that largest scale turbulent motions are significant over the majority of the boundary layer.

7.5 Discussion

The data show that the boundary layer remains turbulent over the length of the cylinder. The RMS velocity fluctuation profiles consistently show a high turbulence level near the boundary and a decreasing turbulence level with increasing radial distance. There is a peak in the profiles at approximately 10-14 mm from the cylinder boundary consistently for both diameters tested. This may be related to the transverse cylinder displacements which are also on the order of 14-mm.

From the correlation function analysis, the magnitudes of the macroscales are on the order of 30-40 mm. The macroscale values are influenced by the integrated effects of the hydrodynamics of the boundary layer and the transverse cylinder displacements. The cylinder displacements will be analyzed in the following Chapter.

Chapter 8: ANALYSIS OF THE TRAJECTORY OF THE FLEXIBLE CYLINDER

The experimental set up simulates the operational configuration of field deployed towed arrays. Therefore, for this experiment, the flexible filament is unrestricted other than at the tow point. As mentioned above, in the series of SPIV images for any run, the cylinders appear to move from frame to frame. This motion can be the result of three effects: inaccurate determination of the cylinder location in the images, unsteady hydrodynamic forces and cylinder geometry. This latter effect occurs because, even if the cylinder were in a fixed location and shape relative to the towing carriage, its intersection with the SPIV plane would move if the cylinder were not completely aligned with the towing direction. In the following, the apparent motion of the cylinders within the SPIV plane are presented and discussed.

8.1 XY Position Data

The data analysis routine which located the cylinder in the field of view for the velocity measurements was also used to track the motion of the cylinder within the SPIV measurement plane (x-y, where y is vertically down) . The x-y coordinates of the filament were recorded for each successive image and used to calculate the displacement between frames as well as the local axial angle of attack between the two frames. This information was used to characterize the magnitudes of the motions and to evaluate the degree of off-axis flow.

Plots of the cylinder position data for U=3.8 m/s and d=0.89 mm are shown in Figure 44. The x and y positions versus axial location are shown in Figure 44 a and b, respectively. As can be seen in the figure, over the length of the filament, it moves sideways (increasing x) about 100 mm and falls vertically about 250 mm . The x-y trajectory (Figure 44 c) illustrates the axial view of the motion history and indicates that there are no radical motions of the cylinder. The local angle of attack of the filament is plotted in Figure 44 d. As can be seen from the plot, the local angle of attack along the filament remains small (less than 5 degrees) over the entire length.

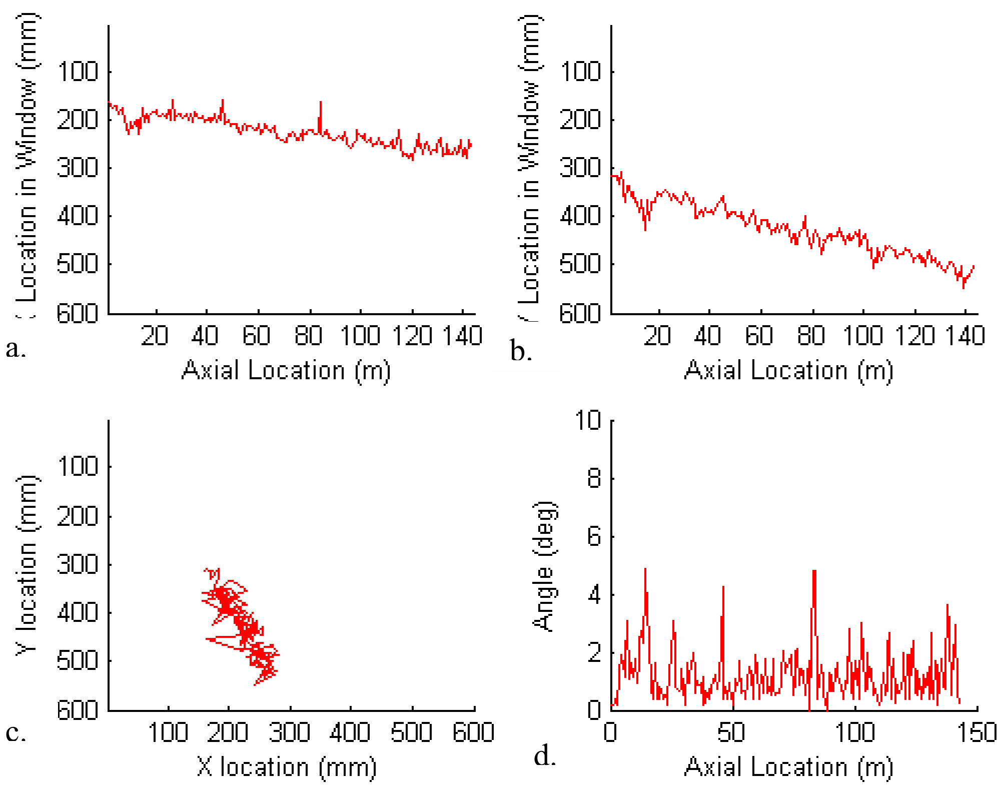

Figure 44: XY Position Data for U=3.8 m/s and d=0.89-mm. The XY position of the cylinder in the field of view is plotted as a function of distance along the filament. a. X versus axial location along the array. b. Y versus axial location c. X versus Y d. Local angle of attack versus axial location.

In order to show the run-to-run variability of the position data, results from three repeated runs for the case U=12.7 m/s and d= 2.5 mm is shown in Figure 45. For the three runs shown in the figure, there is a consistent mean trajectory along the length of the array with a superimposed high-frequency random component. It is thought that the high frequency component of the data is due to inaccuracies in determining the array position in each image. Comparison of Figure 44b and Figure 45b show a mean downward motion which is likely due to the balance of hydrodynamics and gravitational effects. As can be seen in the figures, the cylinder in the slow-speed case, Figure 44b, drops more than the one in the high-speed case, as would be expected. There is also a mean sideward motion of about 100 mm in both cases. This motion is likely due to strut-wake effects and is shown to be repeatable in Figure 45.

In summary, the XY position data for all conditions and speeds (shown in Appendix I) illustrates that the cylinder does not experience extreme motions and the angle of attack remains small over the entire length of the cylinder. Therefore, boundary layer flow can be considered to be developing in an axial manner. Also, the trajectories indicate that the vertical angle of attach is larger for the lower speed runs. This implies that the hydrodynamic drag forces are not sufficient to maintain a level towing geometry for slow speed runs.

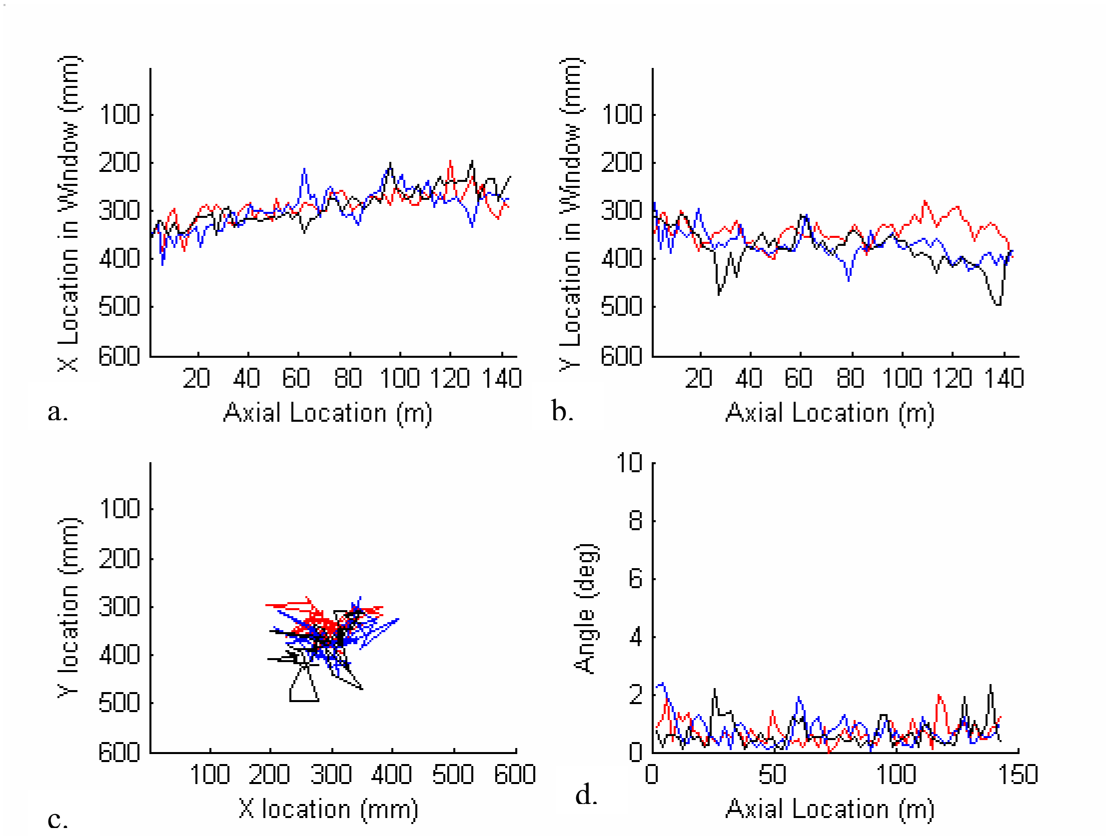

Figure 45: XY Position Data for three runs where U=12.8 m/s and d=2.5-mm. The motions of the cylinder are repeatable for successive runs. The trajectories have a consistent average with perturbation motions on top of the mean. a. X versus axial location along the array. b. Y versus axial location c. X versus Y d. Local angle of attack versus axial location.

8.2 Nondimensional High-Frequency Motion

To characterize the high-frequency motion of the cylinder within the field of view of the SPIV system, the magnitude of the vector displacement (Δs) between successive images was computed. These displacements magnify the high-frequency part of the apparent cylinder motion. As mentioned at the beginning of this chapter, while this high-frequency component is not an explicit indication of the cylinder displacement, it is an indication of the change in location of the high-speed fluid resolved in the data processing analysis. The magnitude of the displacement is determined using the XY position data discussed in the previous section. This magnitude is then scaled with the viscous length:

$$s^{+} = \frac{\Delta s}{l^{+}}$$

The nondimensional displacement, s^+, as a function of axial location for U = 3.8 m/s, d=0.89-mm and 2.5-mm is shown in Figure 46.

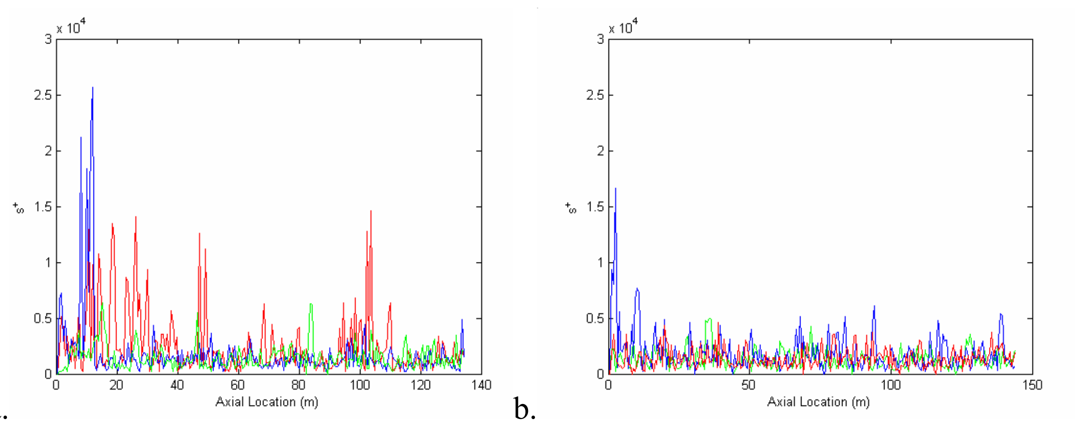

Figure 46: The displacement of the cylinder between sequential measurement planes nondimensionalized by the viscous length scale. a) 3.8 m/s 0.89mm b) 3.8 m/s 2.5mm.

Considering the large spiked values (magnitudes above 10,000 in Figure 46) as outliers, the remaining values were averaged to find a characteristic high-frequency motion magnitude for each run condition. The results are shown in Table 15.

Table 15: Nondimensionalized motion coefficient

Speed (m/s)	Diam (mm)	S^+	(mm)
3.86	0.89	1645	14.1
3.86	2.5	1523	14.2
7.8	0.89	3336	15.2
7.8	2.5	2995	15.1
12.9	0.89	5967	17.0
12.9	2.5	6581	21.0
15.4	0.89	6997	16.6

The averaged nondimensional high-frequency apparent displacements are on the order of thousands of viscous lengths. Motions of this magnitude are a large fraction of the boundary layer thickness (Figure 27). The macro scales of the turbulence calculated in Section 7.4 Correlations and Length Scales, are 2-3 times the magnitude of the mean high-frequency apparent cylinder displacements.

8.3 Mean and Standard Deviation of the Curves of Cylinder Position versus Axial Location

An analysis of the filament position versus axial position was completed to investigate the repeatability of the cylinder catenary, or shape. In this analysis, the cylinder position data for all runs with the same run conditions was averaged together at a specified set of axial locations. As mentioned previously, the axial spacing between sequential images was different depending on towing speed. The averaging procedure used for the velocity fields was also used for the position data; however, position data was averaged over 2.5-meter increments along the cylinder rather than the 10-meter increment used in the velocity analysis. This resulted in 8-10 samples every 2.5 m for all towing conditions. This averaging is justified since the flow and geometry are changing slowing with axial distance. Also, this averaging smooths out some of the high-frequency apparent displacements discussed in the previous section.

The averaged cylinder x-y location with the RMS superimposed as error bars is shown in Figure 47 the two cylinder diameters and all towing speeds. The position information for U=3.8 m/s and d=0.89-mm and d=2.5-mm (Figure 47 a. and b. respectively) indicates that for the same speed the standard deviation decreases with increasing diameter. This is evident at the higher speeds as well. As can be seen from the plots, for the same diameter cylinder the standard deviation decreases with increasing speed. Also, for most cases, the standard deviation increases with increasing distance along the cylinder. This is evident in Figure 47 a, c, d. e, f and g.

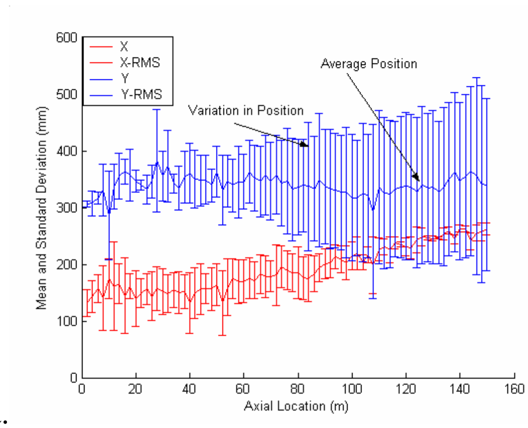

a.

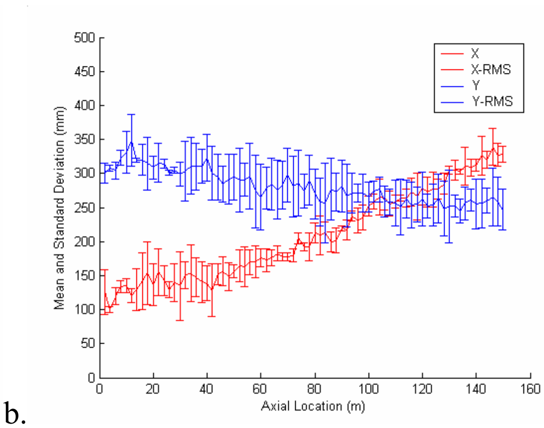

b.

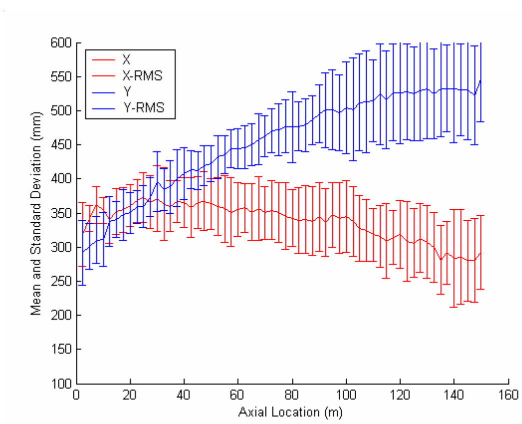

c.

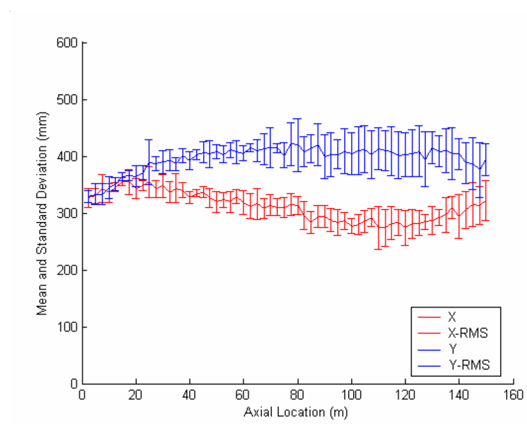

d.

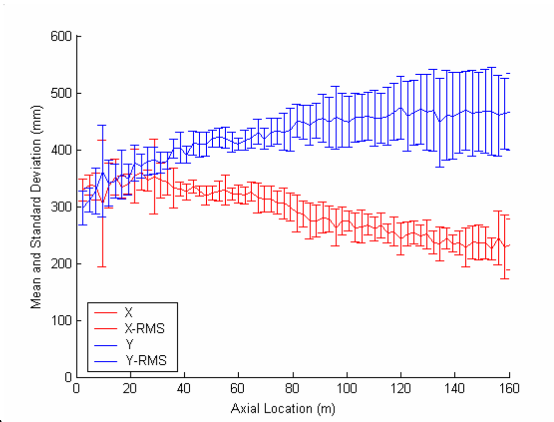

e.

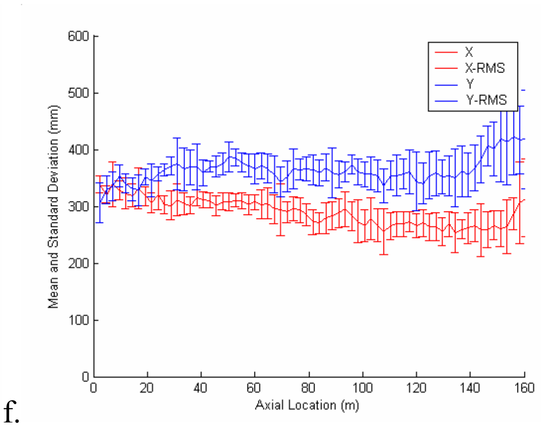

f.

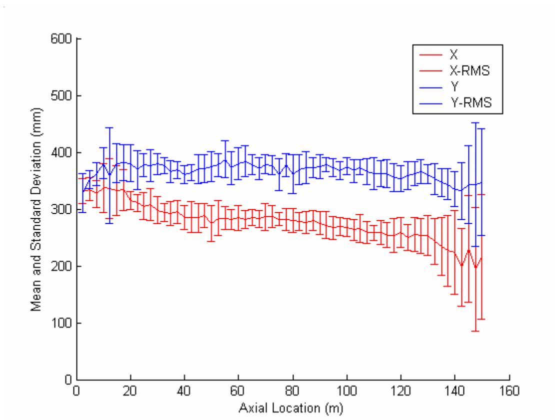

g.

Figure 47: Average and RMS x and y location of the cylinder in the field of view as a function of axial distance along the cylinder. a. U=3.8 m/s d=0.89-mm, b. U=3.8 m/s and d=2.5-mm, c. U=7.7 m/s and d=0.89-mm, d. U=7.7 m/s and d=2.5-mm, e. U=12.8 m/s and d=0.89 mm, f. U=12.8 m/s and d=2.5-mm, g. U=15.4 m/s and d=0.89-mm.

8.4 Discussion

The motion analysis results show that the filament location changes with axial distance and the variations in the filament location characteristically change with speed and diameter. However, though the position changes along the axis, the local angle of attack remains small. As shown in Figure 46, the angle is less than 5 degrees even including the frame-to-frame variation in position, which is thought to be due to inaccuracies in locating the cylinder in each image. Considering only the mean location data, the angle of attack is less than 1 degree. Based on results by Wei et. al (9), for cylinders at angles of attack below 5 degrees, the flow can be considered to develop axially. Therefore, in the present case, the flow probably remains attached over the length of the cylinder.

The motions of the cylinder in the SPIV frame are small relative to both the length of the filament and the field of view. The magnitude of the displacements ranges in value from 14 to 20 mm depending on towing speed and cylinder diameter. However, when nondimensionalized by the viscous length scale, these displacement are between 1600 to 7000 which is a significant fraction of the total boundary layer thickness. The mean and run-to-run RMS of the cylinder trajectories showed that the RMS values were larger near the trailing edge of the cylinders than at the leading edge and were larger for the smaller diameter cylinder and slower speed cases. These results are consistent with the idea that the motion of the cylinder should decrease with increasing drag, which occurs for the large diameter and higher speeds, and increasing mass and added mass, both of which increase with cylinder diameter.

It is also interesting to note that the axial length scale of the mean cylinder motion, i.e., the motion after removing the frame-to-frame high-frequency component, and the axial length scale of the boundary relaxation cycle discussed in Chapters 4 and 6 are both a similar large fraction of the total cylinder length. This may indicate that the relaxation is somehow related to this low-frequency motion.

Chapter 9: DISCUSSION OF CYLINDER MOTION AND PRESSURE SPECTRA

Experimental results support the conclusion that the axisymmetric boundary layer is characteristically different from flat plate boundary layers. The transverse curvature and flexibility of the cylinder strongly affect the resulting surface parameters and boundary layer development. Two topics for consideration will be discussed in this chapter. First, a discussion of the potential effect that the turbulent eddies which occur in the boundary layer have on the cylinder. Secondly, a discussion of how the current boundary layer data for axisymmetric cylinders may be used with scaled pressure spectra for applications to Navy towed array systems. However, no modeling is done here.

9.1 Estimate of the Motion of the Cylinder due to Turbulent Structures

Large turbulent eddies occurring in thick axisymmetric boundary layers can impose cross plane forces on the small diameter cylinder. A simplified two-dimensional model is developed here to investigate how the motions of the turbulent structures contribute to the movement of the cylinder.

Considering the macro scales calculated in Section 7.4 Correlations and Length Scales, turbulent structures can be significantly larger then the diameter of the cylinder. Therefore, when an eddy passes over the cylinder, the entire cross section of the cylinder is acted upon locally by the perturbed flow. Figure 48 illustrates the eddy to be moving as a result of the vector sum of the turbulent velocity components.

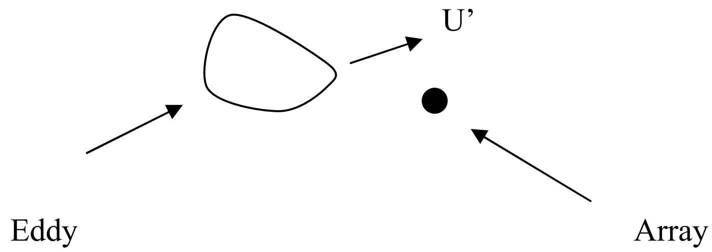

Figure 48: Eddy Model. The eddies moves relative to the cylinder and may cause cylinder motions.

The turbulent eddy causes a perturbation force to act on the cylinder that pushes it normal to its axis and enhances surface shear forces. The following expression is a simplified relationship between the local acceleration of the cylinder with its added mass on the left hand side and the perturbation force from the turbulent eddy on the right hand side.

$$(\rho_{cyl} + \rho_{fluid})\pi a^2 \frac{dU}{dt} = F' = \frac{1}{2}\rho_{fluid} u'^2 C_D (2a)$$

Equation 43

Since the cylinder is approximately neutrally buoyant ($\rho_{cyl}+\rho_{fluid}=2\rho_{fluid}$), this relationship simplifies to an expression for the resulting acceleration:

$$\frac{dU}{dt} = \frac{C_D}{2}\frac{u'^2}{a\pi}$$

Equation 44

The acceleration term is considered to act on the cylinder for the time duration required for the edge of the eddy to traverse the cylinder, $\Delta t_T = 2a/u'$. The acceleration causes a change in the filament velocity, Δu_r, which is the product of the perturbation force and the traverse time (Equation 45). The cylinder displacement is then calculated by multiplying the time increment between data images, Δt_f, and the resultant velocity change (Equation 46).

$$\Delta u_r = \frac{dU}{dt} \Delta t_T$$

Equation 45

$$\Delta r = \Delta u_r \Delta t_f$$

Equation 46

For this model, the fluctuation velocities were conservatively estimated to be approximately equal to the peak values of the measured fluctuating axial velocity profiles (The cross stream components are smaller.). Using these velocities and the cylinder diameters, the Reynolds number range from 4.3 to 60 and the corresponding C_D ranges from about 4 to 1. Thus for this order of magnitude calculation C_D is equal to 2 is used. The results are shown in Table 16.

Table 16: Displacement calculations for the cross plane fluctuations acting on the cylinder.

Speed (m/s)	Diameter (mm)	Cross flow fluctuation (mm/s)	Acceleration (mm/s^2)	Δt_T (s)	Velocity (mm/s)	Motion (mm)
3.85	0.89	5.785	23.951	0.154	3.685	0.614
3.85	2.5	7.63	14.832	0.328	4.860	0.810
7.7	0.89	10.8	83.475	0.082	6.879	1.146
7.7	2.5	19.3	94.902	0.130	12.293	2.049
12.8	0.89	23	378.587	0.039	14.650	2.442
12.8	2.5	29	214.268	0.086	18.471	3.079
15.4	0.89	26	483.790	0.034	16.561	2.760

The cylinder displacements calculated from the eddy perturbation force range from 0.6 to 2.7 mm. These displacement estimates are small compared the frame-to-frame cylinder motions reported in Chapter 8. Therefore, these results indicate that the frame-to-frame cylinder motions are not self-induced motions due to turbulent eddies. This lends further support to the previously mentioned conclusion that the apparent frame-to-frame cylinder motion is due to inaccuracies in determining the location of the cylinder.

9.2 Scaling Pressure Spectra

Pressure spectra for flat plate boundary layers are currently used for modeling near field noise associated with turbulent flow on towed arrays. Pressure spectra can be scaled using local boundary layer parameters (refer to Figure 3). However, as the present results indicate, thick axisymmetric boundary layers are characteristically different from flat plate boundary layers. Nevertheless, as an initial approach, a scaled flat plat pressure spectra will be used as a starting point for estimating the pressure spectra in a thick axisymmetric boundary layer. A set of sample pressure spectra data from Keith et. al. (27) (using data collected by Carey) was selected where the flow specifications are as follows: fully developed pipe flow, using water, Uo=55.7 ft/s, δ=1.75 in, $\delta*$=.22 in, θ=0.175 in. This data will be rescaled using the outer parameters for the axisymmetric boundary layer in this experiment. The dimensional spectra for all run conditions and diameters are shown in Figure 49 with the resulting dimensional spectra for the original data.

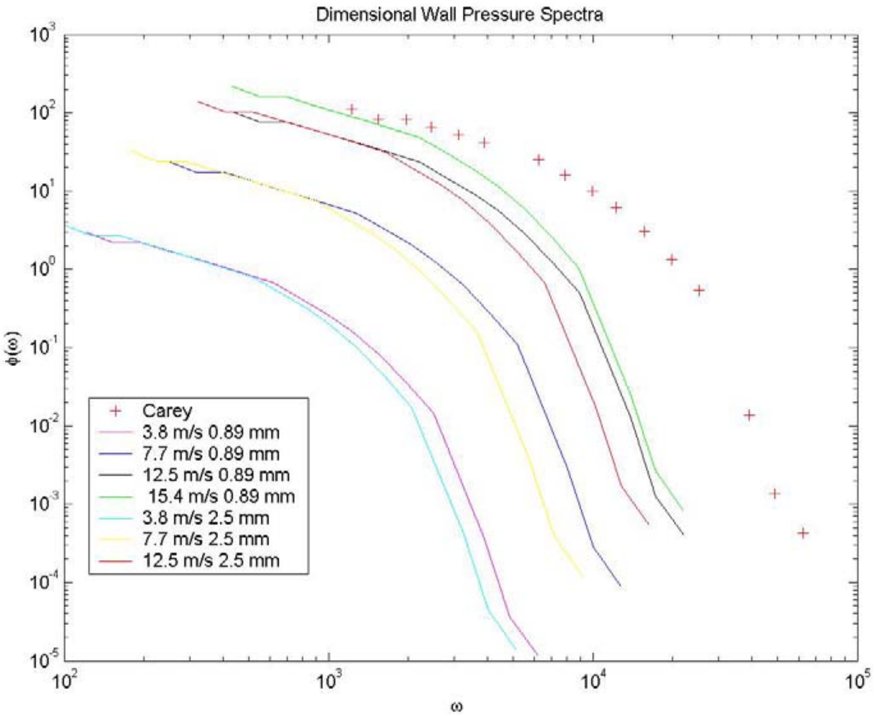

Figure 49: Dimensional Wall Pressure Spectra obtained by starting with the dimensionless spectrum (using outer boundary layer parameters) measured on a flat plate and scaled to the conditions of the present experiment using the measured boundary layer parameters.

As seen in the figure, the scaled spectra is shifted down in both frequency and amplitude compared to the sample data set. The pressure amplitude is greatest at the lower frequencies and decreases with increased frequency. The amplitudes and frequencies increase with increasing speed as would be expected. The smaller diameter has a shift up to higher frequencies when compared to the larger diameter filament at the same towspeed. This does not seem unexpected since the characteristic frequency should be on the order of U/a.

Using the dimensional results in Figure 49, the spectra is scaled using inner parameters for selected axisymmetric cases and for a flat plat boundary layer where Re_θ is equivalent to the axisymmetric cases selected. The cases selected are U= 12.7m/s and d=0.89-mm and 2.5-mm where θ is approximately 12 and 15 mm, and τ is 356 N/m^2 and 283 N/m^2 respectively. A flat plate boundary layer with the same Re_θ where U=12.7 m/s and θ=15 mm has a local wall shear value of only 100 N/m^2. The resulting spectra scaled using inner variables are shown in Figure 50. In addition, scaled spectra for the other axisymmetric boundary layers conditions are also included.

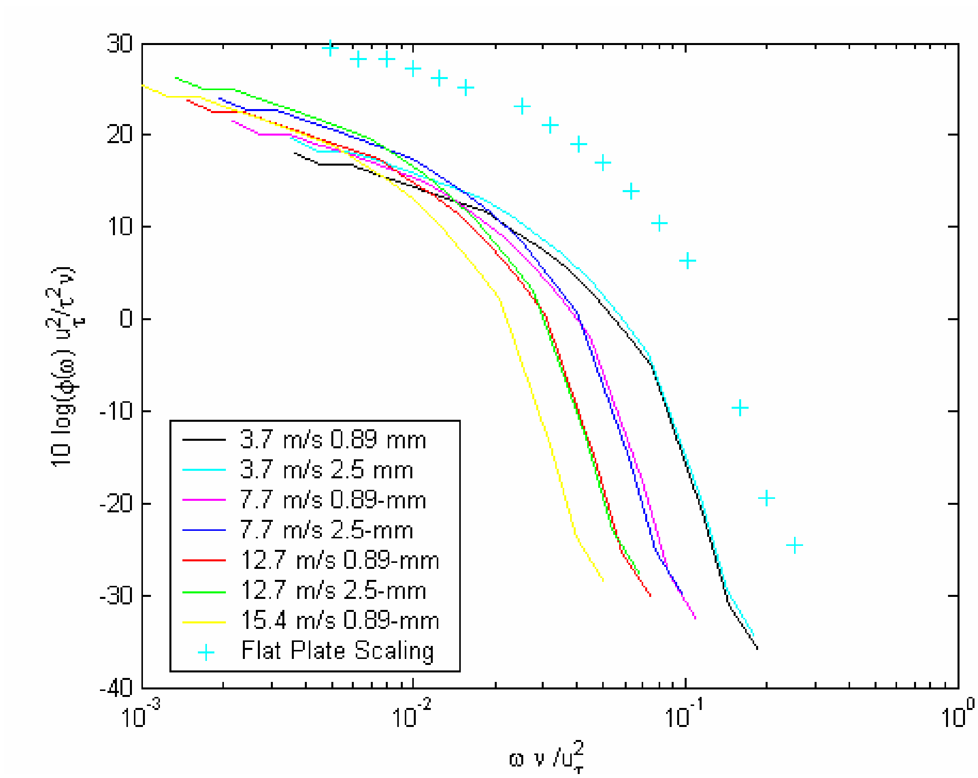

Figure 50: Pressure Spectra using Inner Scaling. The dimensional pressure spectra has been scaled using inner variables for the comparison cases where U= 12.5 m/s, d=0.89-mm and d=2.5 mm and an equivalent flat plate boundary layer with the same Req. In addition, the scaled spectra for the other axisymmetric boundary layer cases (U= 3.7 m/s d=0.89-mm and 2.5-mm, U= 7.7 m/s d=0.89-mm and 2.5-mm, and U=15.4 m/s and d=0.89-mm) are also shown.

The spectra for the filament cases fall close together. However, the spectra scaled using the flat plate parameters is significantly higher in nondimensional pressure amplitude and nondimensional frequency. This indicates that the flat plate boundary layer model does not provide representative scaling parameters for the near wall pressure spectra for an axisymmetric thick boundary layer.

Axisymmetric boundary layers are considerably different from flat plate and therefore, while this scaling provides an initial estimate, it will be necessary to make in-situ pressure measurements to establish a true spectra.

Chapter 10: CONCLUSIONS

Experimental measurements of the drag and boundary layer flow fields around high aspect-ratio flexible cylinders as they were towed axially behind a strut in a large towing tank were reported. Cylinders with diameters (2a) of 0.89 mm and 2.5 mm were used in this study. Total drag was measured for cylinders with various lengths (L) up to 150 m and towing speeds of 3.1, 5.2, 9.3 and 14.4 m/s. Boundary layer flow field measurements were collected using a Stereo Particle Image Velocimetry (SPIV) system at various locations over the 150 m long cylinders at towing speeds of 3.8, 7.7, 12.9 and 15.4 m/s. The longest 0.89-mm and 2.5-mm cylinders had aspect ratio's L/a of $1.5 * 10^5$ and $3*10^5$, respectively. The drag data was used to evaluate the momentum thicknesses at the end of the cylinder for each condition. The boundary flow velocity measurements were used to evaluate the mean and fluctuating velocity profiles as well as the boundary layer thickness, momentum thickness, displacement thickness and cylinder motions.

Due to the severe transverse curvature of these high-aspect-ratio filaments, these results were expected to be very different from those found in flat plate boundary layers. The ratio of boundary flow volume to surface area for a flat-plate geometry is δ (the boundary layer thickness), while for axisymmetric boundary layers the ratio is $\delta(1+\delta/2a)$. These ratios become significantly different as the thickness ratio, δ/a, becomes large, as is the case for high-aspect-ratio small-diameter cylinders. This experiment provides measurements which characterize this type of flow and expands the available data set for axisymmetric boundary layers to larger values of δ/a and to cases with flexible cylinders. The specific findings are presented below.

10.1 Mean Boundary Layer Parameters

The mean drag and velocity results show that the boundary flow develops slowly along the length of the cylinder and the parameters differ significantly from flat plate results. The drag data showed that the wall shear stress values were almost 3 times larger than flat plate values at similar length-based Reynolds numbers and that the average wall shear stress did not diminish in magnitude but fluctuated with increasing length of the cylinder. The boundary layer mean axial velocity profiles are similar in shape to flat plat profiles; however, the near-wall behavior exhibited intermittent relaxations in the velocity distribution. This result is consistent with the wall shear stress findings. The scaled mean velocity profiles were shown to have a significantly reduced slope and an increased offset in the log region compared to the flat plate case. This result is in agreement with existing boundary layer data on fixed cylinders where the boundary layer thickness is much larger than the radius of the cylinder.

The reduced slope of the non-dimensional logarithmic profile means that the relative shear in the log region is smaller for the axisymmetric boundary layer when compared to the flat plate boundary layer. Considering that the wall shear stress is much larger for the filament, most of the change in U occurring across the boundary layer has occurred before the log region. Therefore, the percent change in velocity occurring in the outer region is comparatively small for thick axisymmetric boundary layers.

The integrated average boundary layer flow parameters do not exhibit classic monotonic development along the filament. The boundary layer thickness, displacement thickness and momentum thickness all exhibit initial growth along the filament followed by intermittent fluctuations. This is consistent with the variations in the wall shear values and velocity profiles mentioned above. Also, the momentum thickness values determined from the velocity measurements were consistent with those values determined from the drag results for the full length filament.

10.2 Fluctuating Velocities

The fluctuating velocities occurring in the boundary layer of the filament were calculated to evaluate the extent to which the boundary layer is turbulent. The results show that the boundary layer is consistently turbulent over the entire length of the cylinder and that the RMS axial velocity component is dominant. For the upstream profiles, the strut wake turbulence was evident but the velocity fluctuations near the cylinder were large compared to the background wake turbulence levels. Downstream the turbulence levels occurring near the filament were approximately 8 to 10 times larger than those in the strut wake. The distribution of the turbulent velocity fluctuations was shown to be different from corresponding flat plate distributions in that a peak in the fluctuation value occurs at a large distance from the boundary.

The correlation functions were calculated to extract the turbulent length scales for each condition. The integral length scales were consistently on the order of the boundary layer thickness for each condition, as expected. The Taylor length scales were consistently similar for all conditions. Therefore, the Taylor length scale values are believed to be biased by the spatial resolution of the measurement system and are an indication of the minimum scale realizable for this experimental set up.

10.3 Position Analysis of Filament

The position of the filament in the fixed plane of the SPIV light sheet was analyzed to evaluate the extent of the cylinder motions and to investigate the repeatability of the position data. The trajectories demonstrated that the position information was in general repeatable and the cylinder exhibited no radical motion. The apparent distances the filament traveled between successive images were found to be 1000's of viscous lengths. However, it is thought that these frame-to-frame displacements were due to inaccuracies in locating the cylinder in each SPIV image. The average motion of the cylinder is more or less monotonic during each run, i.e. it does not oscillate. The average angle of attack over the length of the cylinder was found to be on the order of 1 degree or less. Therefore, the boundary flow is considered to develop in an axial manner.

10.4 Future Work

The Navy uses towed arrays for detection, localization and targeting of vessels. These arrays, as previously stated, are typically very long ($L/a=10^4$ to 10^5) and develop very thick boundary layers ($Re_\theta=10^4$ to 10^6) along their length. Currently, flat plate boundary layer models are used to estimate the local pressure spectra when analyzing towed array sonar data. However, the present results indicate that thick axisymmetric boundary layers are characteristically different from existing flat plate boundary layers. Due to the limited data for thick axisymmetric boundary layers, significant work can be done to contribute to the understanding of this type of flow and to contribute to the development of improved acoustic models for towed array data analysis procedures.

For towed array applications, in-situ wall pressure measurements will be necessary to evaluate the spectra for thick axisymmetric boundary layers. From the present results, there is a significant change in the relative shear distribution across the boundary layer from the flat plate case. This variation suggests that the distribution of turbulence production and local vorticity is different from the flat plate case and, therefore, so is the wall pressure spectra. In-situ pressure measurements can be used along with the boundary layer flow parameters collected here to improve acoustic models used for analyzing underwater sonar measurements and can be used to characterize the influence of transverse curvature on the resultant spectra.

Additional considerations for Navy applications include evaluating the effect of adjacent objects on the array behavior and on boundary layer flow. For the case of Littoral operations, the array is towed directly behind the submarine and is in the wake of the submarine. Characterizing the effects of this towing geometry will extend the useful envelope of towed array applications and greatly improve system reliability. For the case of volumetric apertures, configurations involving multiple arrays can be investigated to evaluate the effect of adjacent towed arrays on each other. The present results indicate that the boundary layer thickness can get very large. This consideration as well as the fluctuating character of the flow can be used to optimize volumetric array configurations and determine spacing requirements to optimize the acoustic performance of the system.

Further experiments to investigate the boundary flow around high-aspect-ratio towed cylinders will continue to enhance the boundary layer parameter set and will contribute to the understanding of this complex flow. Very high resolution measurements of the velocity fields will provide details into the near-wall velocity fluctuations and may provide data to evaluate how far the inner viscous region extends from the boundary for axisymmetric boundary layers.

Appendix A: High Speed Carriage Data at DTMB

The speed accuracy on the high speed carriage at DTMB is better than 0.5% for all speeds of interest for this experiment. Using positional triggering for the SPIV data acquisition will give a positional accuracy of .005*60 f/s*10 seconds (duration model is in the test section) or 0.3 ft. Or, if the maximum speed deviation values are used as the worst case uncertainty, at 60 f/s, the uncertainty in position would be 0.101 kts*10secs or aproximately 2 ft max. Considering the slow growth of the boundary layer and the data analysis method of averaging data every 25 feet of array, this accuracy is sufficient for this data set.

Setpoint Speed* (Knots)	Maximum Speed (Knots)	Minimum Speed (Knots)	Total Variation (Max. Speed minus Min. Speed) (Knots)	Ratio of Total Variation to Speed Setpoint (%)	Mean Speed (Knots)	Standard Deviation (Knots)	Ratio of Standard Deviation to Mean Speed (%)
1.00	1.023	0.984	0.039	3.90%	1.003	0.0087	**0.87%**
2.00	2.029	1.985	0.044	2.20%	2.006	0.0080	**0.40%**
3.00	3.020	2.991	0.029	0.97%	3.006	0.0055	**0.18%**
4.00	4.021	3.992	0.029	0.72%	4.007	0.0061	**0.15%**
5.00	5.023	4.998	0.025	0.50%	5.010	0.0049	**0.10%**
6.00	6.024	5.995	0.029	0.48%	6.010	0.0054	**0.09%**
7.00	7.035	7.001	0.034	0.49%	7.014	0.0071	**0.10%**
8.00	8.026	7.992	0.034	0.42%	8.014	0.0065	**0.08%**
9.00	9.032	8.998	0.034	0.38%	9.016	0.0069	**0.08%**
15.00	15.030	14.946	0.084	0.56%	14.990	0.0142	**0.09%**
20.00	20.020	19.938	0.082	0.41%	19.980	0.0123	**0.06%**
25.00	24.995	24.894	0.101	0.40%	24.950	0.0164	**0.07%**

*Setpoint speed is the speed programmed into the carriage control system prior to a run.

Appendix B: DTMB Small Diameter Cylinder Drag Measurements 2003

DTMB Small Diameter Cylinder Tow Test Drag Measurements (June 2003)

Config	Line Type	D (in)	L (ft)	L/a	Uo (kts)	Uo (ft/s)	Re_a	Re_L	Approx. Cd	Drag Estimate (lbs)	Number of Runs	Momentum Thick Est. (in)	Ra*a/L
1	80 lb test	0.035	500	3.4E+05	5	8.45	1.23E+03	4.23E+08	6.19E-03	1.96	10	0.79	3.6E-03
2	(PIV)	0.035	500	3.4E+05	15	25.35	3.70E+03	1.27E+09	4.50E-03	12.85	10	0.67	1.1E-02
3		0.035	500	3.4E+05	25	42.25	6.16E+03	2.11E+09	4.20E-03	33.32	10	0.65	1.8E-02
4		0.035	500	3.4E+05	35	59.15	8.63E+03	2.96E+09	4.00E-03	62.19	10	0.63	2.5E-02
5	Varying L	0.035	475	3.3E+05	6	10.14	1.48E+03	4.82E+08	5.80E-03	2.52	1	0.74	4.5E-03
6	(Drag Only)	0.035	475	3.3E+05	10	16.9	2.46E+03	8.03E+08	5.33E-03	6.43	1	0.71	7.6E-03
7		0.035	475	3.3E+05	18	30.42	4.44E+03	1.44E+09	4.40E-03	17.19	1	0.65	1.4E-02
8		0.035	475	3.3E+05	28	47.32	6.90E+03	2.25E+09	4.06E-03	38.38	1	0.62	2.1E-02
9		0.035	425	2.9E+05	6	10.14	1.48E+03	4.31E+08	5.80E-03	2.25	1	0.70	5.1E-03
10		0.035	425	2.9E+05	10	16.9	2.46E+03	7.18E+08	5.33E-03	5.75	1	0.67	8.5E-03
11		0.035	425	2.9E+05	18	30.42	4.44E+03	1.29E+09	4.40E-03	15.38	1	0.61	1.5E-02
12		0.035	425	2.9E+05	28	47.32	6.90E+03	2.01E+09	4.07E-03	34.43	1	0.59	2.4E-02
13		0.035	375	2.6E+05	6	10.14	1.48E+03	3.80E+08	5.65E-03	1.94	1	0.65	5.8E-03
14		0.035	375	2.6E+05	10	16.9	2.46E+03	6.34E+08	5.25E-03	4.99	1	0.63	9.6E-03
15		0.035	375	2.6E+05	18	30.42	4.44E+03	1.14E+09	4.44E-03	13.69	1	0.57	1.7E-02
16		0.035	375	2.6E+05	28	47.32	6.90E+03	1.77E+09	4.08E-03	30.45	1	0.55	2.7E-02
17		0.035	325	2.2E+05	6	10.14	1.48E+03	3.30E+08	5.65E-03	1.68	1	0.60	6.6E-03
18		0.035	325	2.2E+05	10	16.9	2.46E+03	5.49E+08	5.26E-03	4.34	1	0.58	1.1E-02
19		0.035	325	2.2E+05	18	30.42	4.44E+03	9.89E+08	4.47E-03	11.94	1	0.53	2.0E-02
20		0.035	325	2.2E+05	28	47.32	6.90E+03	1.54E+09	4.12E-03	26.67	1	0.51	3.1E-02
21		0.035	275	1.9E+05	6	10.14	1.48E+03	2.79E+08	6.06E-03	1.52	1	0.57	7.8E-03
22		0.035	275	1.9E+05	10	16.9	2.46E+03	4.65E+08	5.55E-03	3.87	1	0.55	1.3E-02
23		0.035	275	1.9E+05	18	30.42	4.44E+03	8.37E+08	4.53E-03	10.25	1	0.49	2.4E-02
24		0.035	275	1.9E+05	28	47.32	6.90E+03	1.30E+09	4.19E-03	22.93	1	0.47	3.7E-02
25		0.035	225	1.5E+05	6	10.14	1.48E+03	2.28E+08	6.29E-03	1.29	1	0.53	9.6E-03
26		0.035	225	1.5E+05	10	16.9	2.46E+03	3.80E+08	5.73E-03	3.27	1	0.50	1.6E-02
27		0.035	225	1.5E+05	18	30.42	4.44E+03	6.84E+08	4.61E-03	8.53	1	0.45	2.9E-02
28		0.035	225	1.5E+05	28	47.32	6.90E+03	1.06E+09	4.24E-03	18.99	1	0.43	4.5E-02
29		0.035	175	1.2E+05	6	10.14	1.48E+03	1.77E+08	6.37E-03	1.02	1	0.47	1.2E-02
30		0.035	175	1.2E+05	10	16.9	2.46E+03	2.96E+08	5.77E-03	2.56	1	0.44	2.1E-02
31		0.035	175	1.2E+05	18	30.42	4.44E+03	5.32E+08	4.57E-03	6.58	1	0.39	3.7E-02
32		0.035	175	1.2E+05	28	47.32	6.90E+03	8.28E+08	4.14E-03	14.42	1	0.37	5.8E-02
33		0.035	125	8.6E+04	6	10.14	1.48E+03	1.27E+08	6.55E-03	0.75	1	0.40	1.7E-02
34		0.035	125	8.6E+04	10	16.9	2.46E+03	2.11E+08	5.84E-03	1.85	1	0.37	2.9E-02
35		0.035	125	8.6E+04	18	30.42	4.44E+03	3.80E+08	4.41E-03	4.53	1	0.32	5.2E-02
36		0.035	125	8.6E+04	28	47.32	6.90E+03	5.92E+08	3.89E-03	9.68	1	0.30	8.1E-02
37		0.035	75	5.1E+04	6	10.14	1.48E+03	7.61E+07	7.09E-03	0.49	1	0.32	2.9E-02
38		0.035	75	5.1E+04	10	16.9	2.46E+03	1.27E+08	6.11E-03	1.16	1	0.29	4.8E-02
39		0.035	75	5.1E+04	18	30.42	4.44E+03	2.28E+08	4.16E-03	2.57	1	0.24	8.6E-02
40		0.035	75	5.1E+04	28	47.32	6.90E+03	3.55E+08	3.55E-03	5.30	1	0.22	1.3E-01
41	fiber optic	0.1	500	1.2E+05	5	8.45	3.52E+03	4.23E+08	5.00E-03	4.53	10	1.18	2.9E-02
42	cable	0.1	500	1.2E+05	10	16.9	7.04E+03	8.45E+08	4.5E-03	16.32	10	1.11	5.9E-02
43	(PIV)	0.1	500	1.2E+05	25	42.25	1.76E+04	2.11E+09	3.50E-03	79.33	10	0.98	1.5E-01
44		0.1	500	1.2E+05	35	59.15	2.46E+04	2.96E+09	3.20E-03	142.16	10	0.93	2.1E-01
45	fiber optic	0.1	400	9.6E+04	6	10.14	4.23E+03	5.07E+08	4.90E-03	6.40	1	1.04	3.5E-02
46	cable	0.1	400	9.6E+04	10	16.9	7.04E+03	8.45E+08	4.50E-03	16.32	1	0.99	5.9E-02
47		0.1	400	9.6E+04	18	30.42	1.27E+04	1.52E+09	3.97E-03	46.65	1	0.93	1.1E-01
48		0.1	400	9.6E+04	28	47.32	1.97E+04	2.37E+09	3.40E-03	96.67	1	0.85	1.6E-01
49		0.1	300	7.2E+04	6	10.14	4.23E+03	4.06E+08	4.90E-03	5.12	1	0.89	5.9E-02
50		0.1	300	7.2E+04	10	16.9	7.04E+03	6.76E+08	4.50E-03	13.06	1	0.85	9.8E-02
51		0.1	300	7.2E+04	18	30.42	1.27E+04	1.22E+09	3.97E-03	37.32	1	0.80	1.8E-01
52		0.1	300	7.2E+04	28	47.32	1.97E+04	1.89E+09	3.40E-03	77.33	1	0.73	2.1E-01
53		0.1	200	4.8E+04	6	10.14	4.23E+03	3.04E+08	4.90E-03	3.84	1	0.72	8.8E-02
54		0.1	200	4.8E+04	10	16.9	7.04E+03	5.07E+08	4.50E-03	9.79	1	0.69	1.5E-01
55		0.1	200	4.8E+04	18	30.42	1.27E+04	9.13E+08	3.97E-03	27.99	1	0.64	2.6E-01
56		0.1	200	4.8E+04	28	47.32	1.97E+04	1.42E+09	3.40E-03	58.00	1	0.59	2.7E-01
57		0.1	100	2.4E+04	6	10.14	4.23E+03	2.03E+08	4.90E-03	2.56	1	0.49	1.8E-01
58		0.1	100	2.4E+04	10	16.9	7.04E+03	3.38E+08	4.50E-03	6.53	1	0.47	2.9E-01
59		0.1	100	2.4E+04	18	30.42	1.27E+04	6.08E+08	3.97E-03	18.66	1	0.44	5.3E-01
60		0.1	100	2.4E+04	28	47.32	1.97E+04	9.46E+08	3.40E-03	38.67	1	0.40	4.1E-01
61	Leader Line	0.1	57.17		5	8.45			5.00E-03	0.82	1		
62		0.1	57.17		6	10.14			5.00E-03	1.16	1		
63		0.1	57.17		10	16.9			4.50E-03	2.64	1		
64		0.1	57.17		15	25.35			4.30E-03	5.52	1		
65		0.1	57.17		18	30.42			4.30E-03	7.18	1		
66		0.1	57.17		25	42.25			3.60E-03	12.90	1		
67		0.1	57.17		28	47.32			3.40E-03	16.30	1		
68		0.1	57.17		35	59.15			3.20E-03	26.00	1		
MIN				2.4E+04			1.2E+03	7.6E+07	3.20E-03	0.49		0.22	3.6E-03
MAX				3.4E+05			2.5E+04	3.0E+09	7.09E-03	142.16		0.79	5.3E-01

Appendix C: Leading Edge Boundary Condition for Small Diameter Cylinder Tow Tests in Water

Dr. K. Cipolla and Dr. W. Keith

<u>Description of Setup:</u>

A leader line of 0.1” diameter and 57’2” length was attached to a load cell at the tow point. The purpose of the leader is to separate the cylinder under test from any effects of vortex shedding from the tow strut. The uncertainty due to this effect is potentially much larger than uncertainties due to any other flow field effects. At the end of the leader line was a large fishing snap swivel, which is approximately 3.125” long and 7/16” across at its widest point. A picture is included below. The cylinder under test was tied with a small knot to the snap end of the swivel.

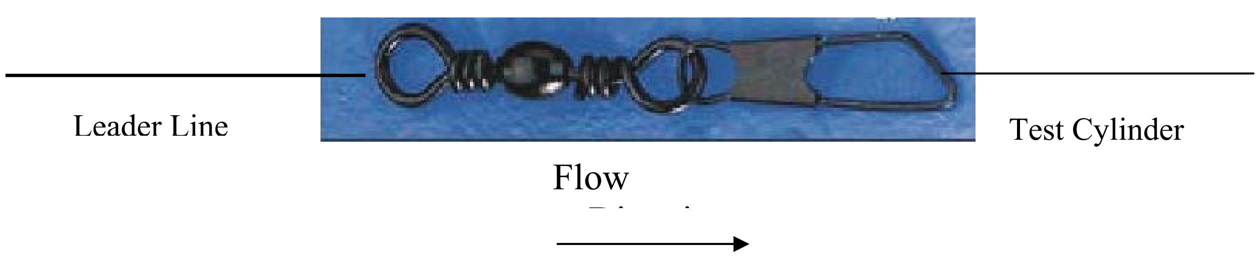

During testing, a turbulent boundary layer grows on the leader line. Based on previous measurements using 116 ft of the same line, we estimate that the momentum thickness θ at the end of the leader line at 17 kts is approximately 0.25” (diameter is approx. 0.5”). At this location, there will be a momentum deficit due to the presence of the boundary layer.

Effect on the Boundary Layer:

A fundamental issue is whether the snap swivel acts as a large enough disturbance to annihilate the upstream boundary layer. If this is the case, the momentum deficit due to the boundary layer is eliminated, and the inflow to the forward end, or leading edge, of the cylinder can be considered uniform flow. For the control volume analysis of a cylinder with an axisymmetric boundary layer, the total measured drag is due to the shear stress at the cylinder wall, and there are no pressure gradient or pressure drag contributions (e.g. the form drag at the end of the cylinder is negligible in comparison to the skin friction drag). Therefore, we are interested in the difference between the momentum thicknesses at the forward and aft ends of the cylinder. This is exactly balanced by the wall shear stress, and allows determination of the momentum thickness at the aft end assuming that there is negligible momentum deficit at the forward end.

The swivel can be treated as a step whose height h is on the order of the boundary layer thickness δ, assuming $\delta/\theta \approx 10$. According to Farabee (1986), if $h/\delta \approx 1$, then the discontinuity will act as a strong perturbation to the boundary layer, causing it to separate and reattach a short distance downstream. For this configuration, since h is not much greater than δ, any separation bubble that forms is expected to be small. However, previous tests have shown that the drag due to the swivel is measurable, and therefore we feel it is appropriate to treat the swivel as a bluff body. If the upstream boundary layer remained attached over the swivel, the added drag due to the surface of the swivel would be negligible. This bluff body, or step, will create a highly turbulent shear layer which will convect over the leading edge of the cylinder. At the reattachment location, downstream from the leading edge, a new boundary layer will start to grow from the surface of the cylinder.

Therefore, the only uncertainty is in the exact origin of the boundary layer. The control volume analysis ensures that the calculated value of the momentum thickness at the end of the line is correct, as long as the momentum deficit at the leading edge is negligible. Further, effectively we are referencing the momentum thickness at the end of the cylinder to the arc length from the leading edge, rather than from the exact origin of the boundary layer. Farabee states that reattachment occurs at a location approximately 6h downstream of separation, and the boundary layer returns to an equilibrium state approximately 10h downstream. For the geometry considered here, that distance will be approximately 4.5", or less than 1% for all lengths tested. The effect of the uncertainty in the origin of the boundary layer is therefore negligible.

Experimental Evaluation:

From a practical standpoint, if the momentum deficit at the aft end of the leader had a significant effect on the boundary layer development on the test cylinder, then a variation in the leader line configuration (and therefore the momentum deficit) would lead to different results. However, data obtained during tow tests using a much shorter leader (18 ft) agrees with the results from tests with a 57' leaderline. For the 18' leaderline, the momentum thickness would be approximately 30% of the value for the 57 ft leader. In addition, a small amount of data was obtained during a test when no leader line was used, and these results agree as well.

Reference:

Farabee, T., “An Experimental Investigation of Wall Pressure Fluctuations Beneath Non-Equilibrium Turbulent Flows,” DTNSRDC-86/047, May 1986.

Appendix D: Stereo Particle Image Velocimetry System Specifications

1. Spatial Resolution

   a. For the 2’ x 2’ FOV, the spatial resolution is:

   $$\frac{2048\,pixels}{24inches} = 85.33\,pixels/inch = 3.36\,pixels/mm \quad or \quad 0.29mm/\,pixel$$

   b. f 2048 x 2048 which is imaging a 60 cm x 60 cm. The resulting spatial resolution is 60cm/2048 pixels or 0.3 mm/pixel.

2. Sheet thickness

   a. An axial displacement on the order of 15 pixels is desired. For a freestream velocity of 18 m/s and a 60cm FOV, the axial displacement of 20 pixels would correspond to:

   $$\frac{60cm}{2048\,pixels} * 15\,pixel\ displacement = 0.45cm\ displacement$$

   b. To ensure particles remain in the light sheet for cameras set at 30 degrees relative to the sheet, the required thickness is 2 times the displacement/cos(60)

   $$0.45cm * \frac{2}{\cos\left(\frac{\pi}{3}\right)} = 1.8cm$$

Equation 47

3. Dynamic Range

    a. The reduction technique can determine particle displacements to a 1/10 of a pixel.

    b. At towspeed, a particle will displace 100 pixel. Therefore, the resolution capability of the SPIV system is 0.1pix/100 pix or 1/1000. The velocity resolution is 1/1000 of towspeed.

    c. Considering particle displacements expected are on the order of 6-10 pixels, the largest velocity measured will be 10 pix/100 pix or 1/10 towspeed.

4. Spatial measurement resolution: 16x16 pix interrrogation regions with 50% overlap gives measurement every 8 pixels, or every 2.38 mm.

5. Particle size: 40 µm (approximately 4 pixels).

Appendix E: Calibration grids

PVC plate: 1.5 inches thick

CNC machined to have precise grid locations and line widths. The calibration crosses are machined to have a line width of 0.022″ which will be approximately 3 pixels wide when imaged by the SPIV system.

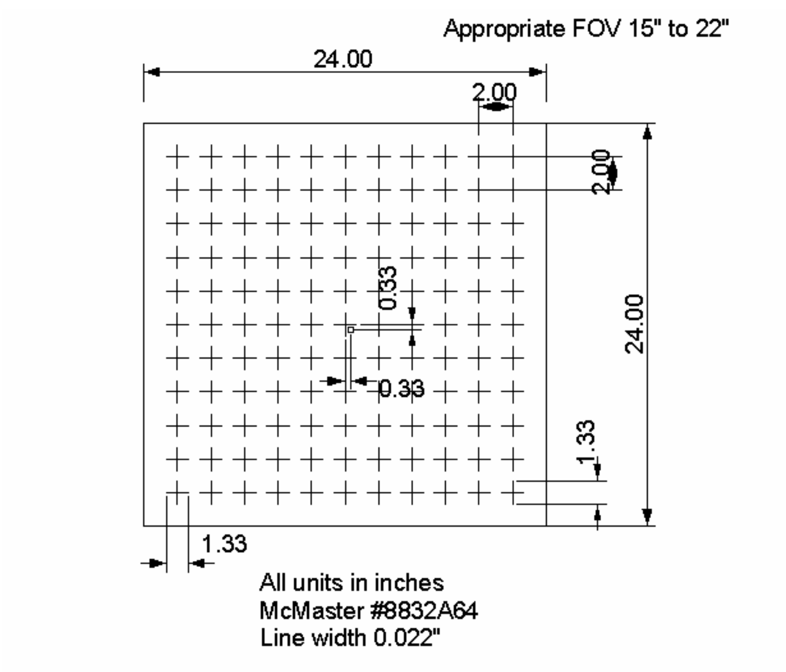

Appendix F: Stereo Particle Image Velocimetry Calibration and Mapping Information

Mapping the field of view (Plane of interest) to the camera image plane involves a 3 dimensional calibration procedure to allow for the extraction of the 3 components of velocity. The mapping function is composed of the image gradients, or pixel displacements corresponding to spatial displacements.

The mapping matrix,. M(x), is developed from the displacements of the grid marks in the calibration as follows.

From the lens equations, the magnification is expressed:

$$M = \frac{d_i}{d_0 - z}$$

where d_i is the distance from the lens to the image plane, d_o-z is the distance from the lens to the nominal plane of interest minus any displacement normal to the plane by the particle. Through ray tracing type approach, it can be understood that each location in the plane of interest will map to a pixel location on the camera CCD. Each grid mark is directly mapped to particular pixels;

$$\bar{X} = F(\bar{x})$$

where x is the 3-D object space and X is position in 2-D image space on the CCD image plane. When the particle moves from location x to x +Δx, the displacement on the image plane can be expressed as:

$$\Delta \bar{X} = F(\bar{x} + \Delta \bar{x}) - F(\bar{x})$$

Using a Taylor series expansion, it can be expressed in terms of image gradients:

$$\Delta \bar{X} \cong \nabla F(\bar{x}) \Delta \bar{x} \text{ where } \nabla F = \frac{-d_i}{d_o} \begin{bmatrix} 1 & 0 & \dfrac{x}{d_o - z} \\ 0 & 1 & \dfrac{y}{d_0 - z} \\ & & \end{bmatrix}$$

Column 3 represents the effect of perspective and is related to the magnification effects and nonlinear effects of the imaging system. These expressions represent the mapping expressions for one camera. For SPIV, two cameras are used and therefore there are four equations available to resolve the displacement Δx.

$$\Delta \bar{X}^{c} \cong \nabla F^{c}(\bar{x}) \Delta \bar{x} \text{ where system looks like}$$

$$\begin{pmatrix} \Delta X_1^1 \\ \Delta X_2^1 \\ \Delta X_1^2 \\ \Delta X_2^2 \end{pmatrix} = \begin{bmatrix} F_{11}^1 & F_{12}^1 & F_{13}^1 \\ F_{21}^1 & F_{22}^1 & F_{23}^1 \\ F_{11}^2 & F_{12}^2 & F_{13}^2 \\ F_{21}^2 & F_{22}^2 & F_{23}^2 \end{bmatrix} \begin{pmatrix} \Delta x_1 \\ \Delta x_2 \\ \Delta x_3 \end{pmatrix}$$

The system is redundant, two of the resulting equations will be dependent. Different methods are used to reduce the equations to a 3x3 system which can then be solved for $\Delta \bar{x}$, object space and used to reduce the particle velocity in 3 dimensions.

Appendix G: Dimensional Boundary Layer Profiles

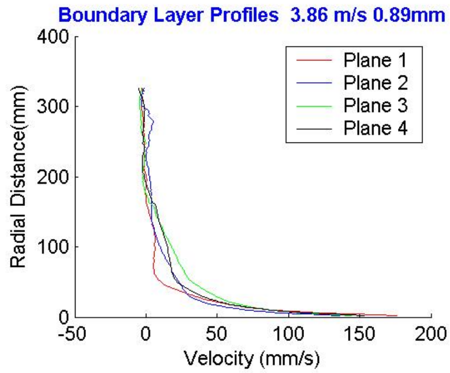

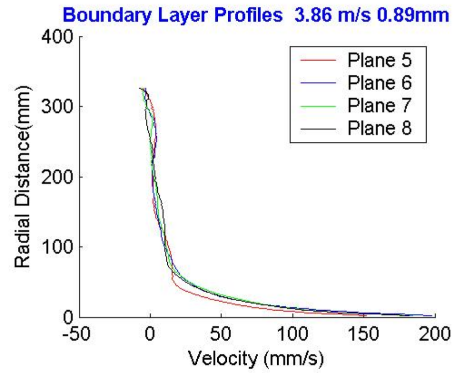

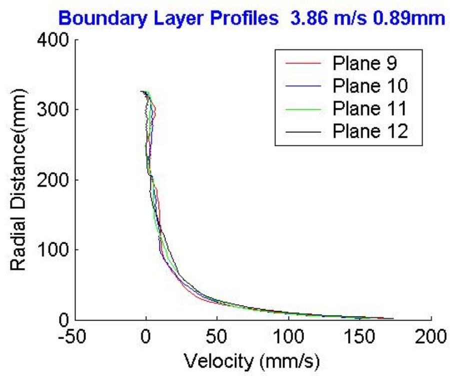

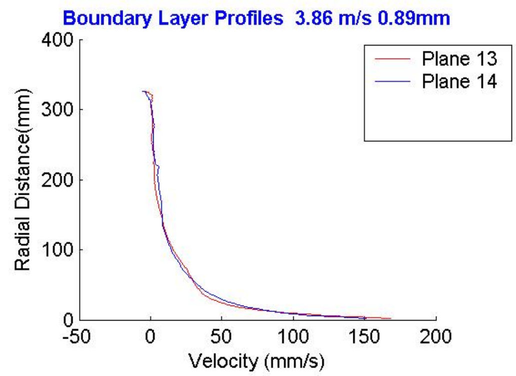

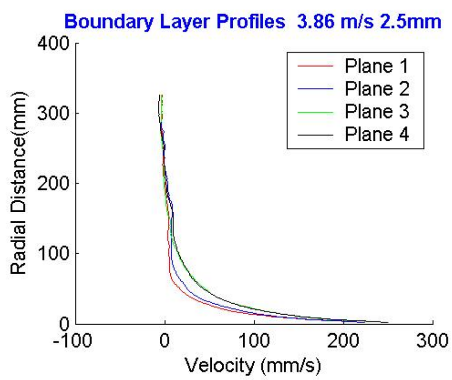

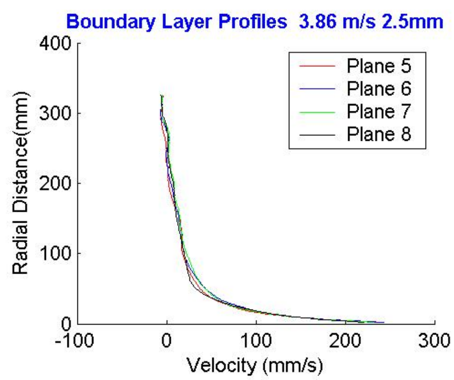

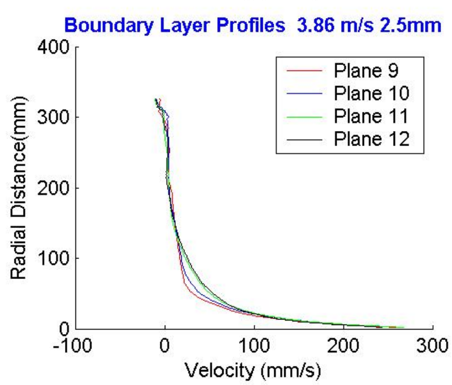

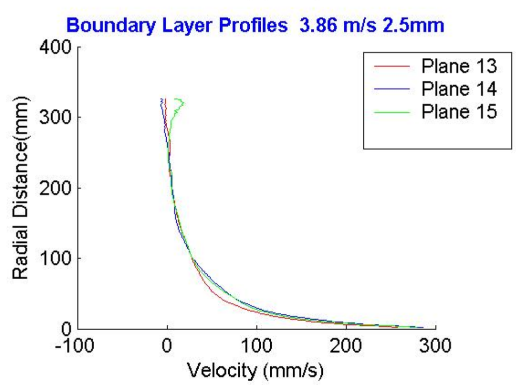

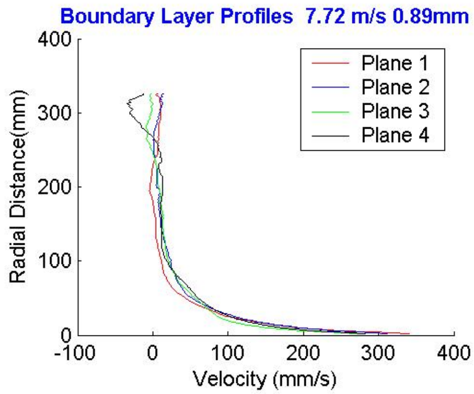
Boundary Layer Profiles 7.72 m/s 0.89mm
Plane 1
Plane 2
Plane 3
Plane 4
Radial Distance(mm)
Velocity (mm/s)

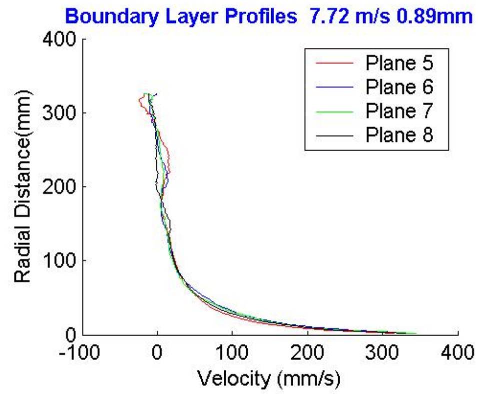
Boundary Layer Profiles 7.72 m/s 0.89mm
Plane 5
Plane 6
Plane 7
Plane 8
Radial Distance(mm)
Velocity (mm/s)

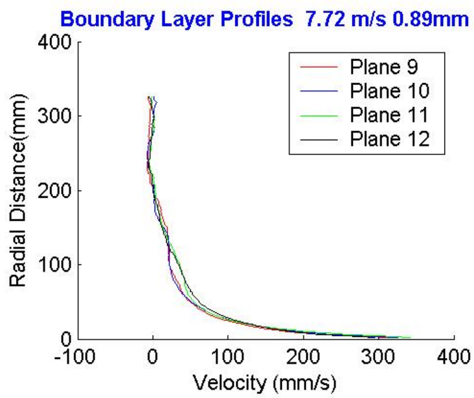
Boundary Layer Profiles 7.72 m/s 0.89mm
Plane 9
Plane 10
Plane 11
Plane 12
Radial Distance(mm)
Velocity (mm/s)

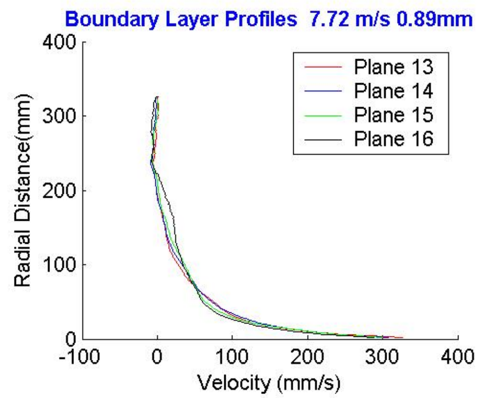
Boundary Layer Profiles 7.72 m/s 0.89mm
Plane 13
Plane 14
Plane 15
Plane 16
Radial Distance(mm)
Velocity (mm/s)

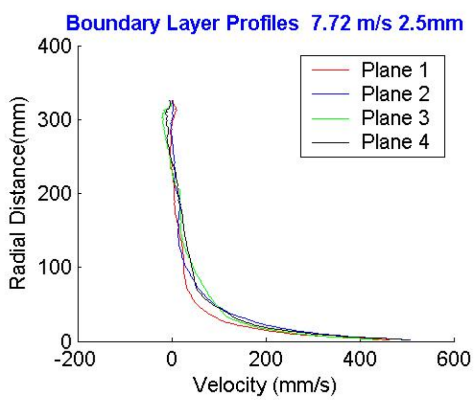
Boundary Layer Profiles 7.72 m/s 2.5mm
Plane 1
Plane 2
Plane 3
Plane 4
Radial Distance(mm)
Velocity (mm/s)

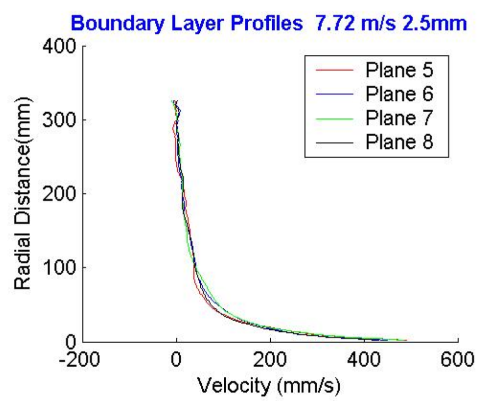
Boundary Layer Profiles 7.72 m/s 2.5mm
Plane 5
Plane 6
Plane 7
Plane 8
Radial Distance(mm)
Velocity (mm/s)

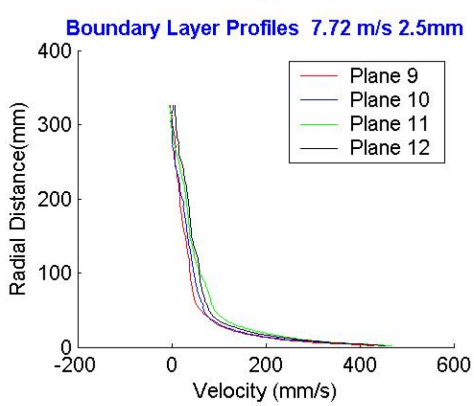
Boundary Layer Profiles 7.72 m/s 2.5mm
Plane 9
Plane 10
Plane 11
Plane 12
Radial Distance(mm)
Velocity (mm/s)

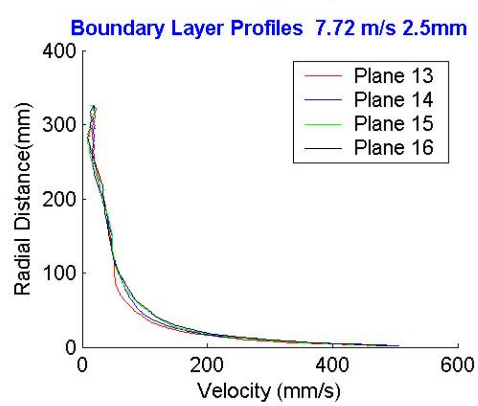
Boundary Layer Profiles 7.72 m/s 2.5mm
Plane 13
Plane 14
Plane 15
Plane 16
Radial Distance(mm)
Velocity (mm/s)

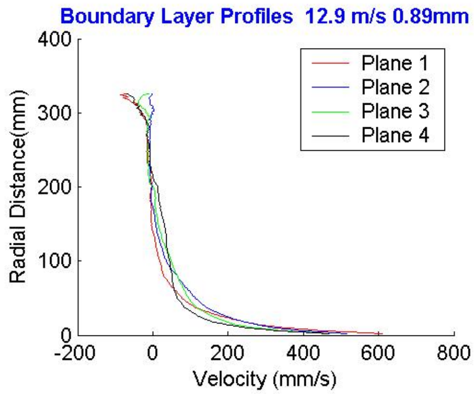
Boundary Layer Profiles 12.9 m/s 0.89mm
Radial Distance(mm)
Velocity (mm/s)
Plane 1
Plane 2
Plane 3
Plane 4

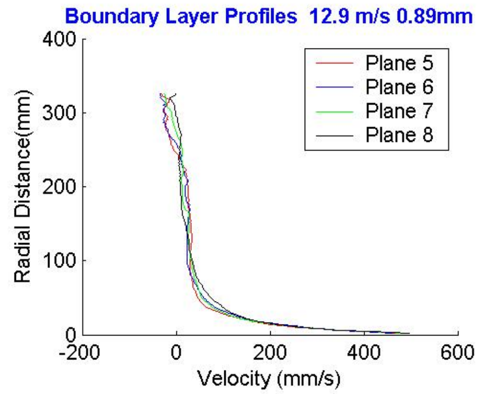
Boundary Layer Profiles 12.9 m/s 0.89mm
Radial Distance(mm)
Velocity (mm/s)
Plane 5
Plane 6
Plane 7
Plane 8

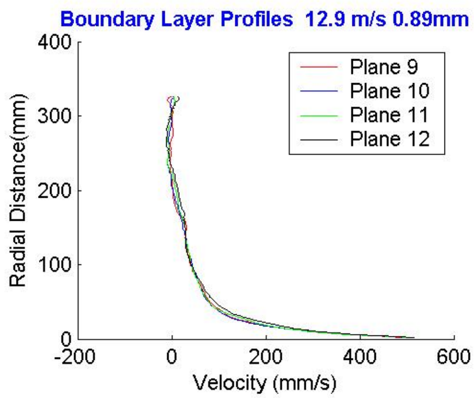
Boundary Layer Profiles 12.9 m/s 0.89mm
Radial Distance(mm)
Velocity (mm/s)
Plane 9
Plane 10
Plane 11
Plane 12

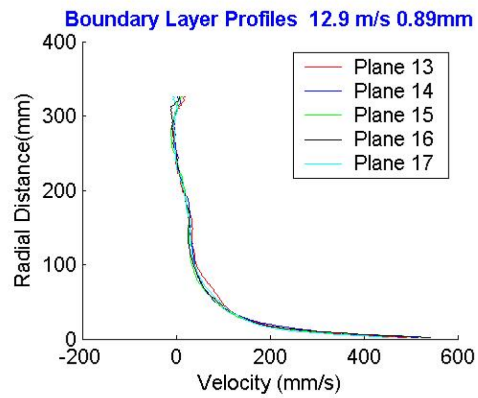
Boundary Layer Profiles 12.9 m/s 0.89mm
Radial Distance(mm)
Velocity (mm/s)
Plane 13
Plane 14
Plane 15
Plane 16
Plane 17

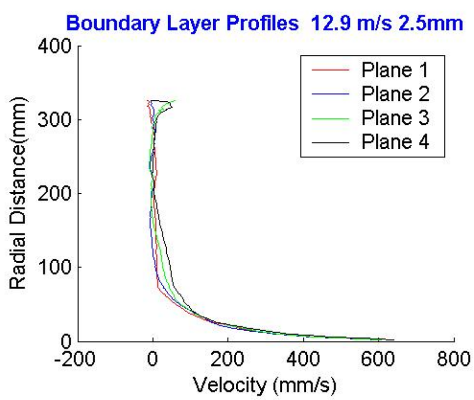
Boundary Layer Profiles 12.9 m/s 2.5mm
Radial Distance(mm)
Velocity (mm/s)
Plane 1
Plane 2
Plane 3
Plane 4

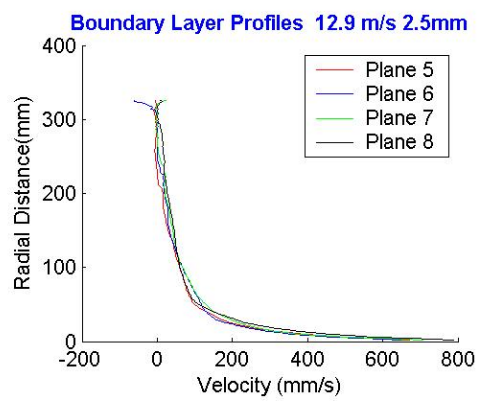
Boundary Layer Profiles 12.9 m/s 2.5mm
Radial Distance(mm)
Velocity (mm/s)
Plane 5
Plane 6
Plane 7
Plane 8

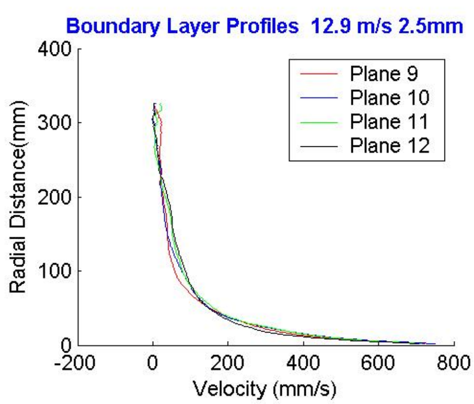
Boundary Layer Profiles 12.9 m/s 2.5mm
Radial Distance(mm)
Velocity (mm/s)
Plane 9
Plane 10
Plane 11
Plane 12

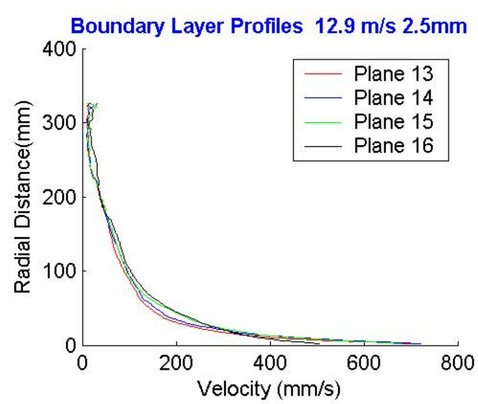
Boundary Layer Profiles 12.9 m/s 2.5mm
Radial Distance(mm)
Velocity (mm/s)
Plane 13
Plane 14
Plane 15
Plane 16

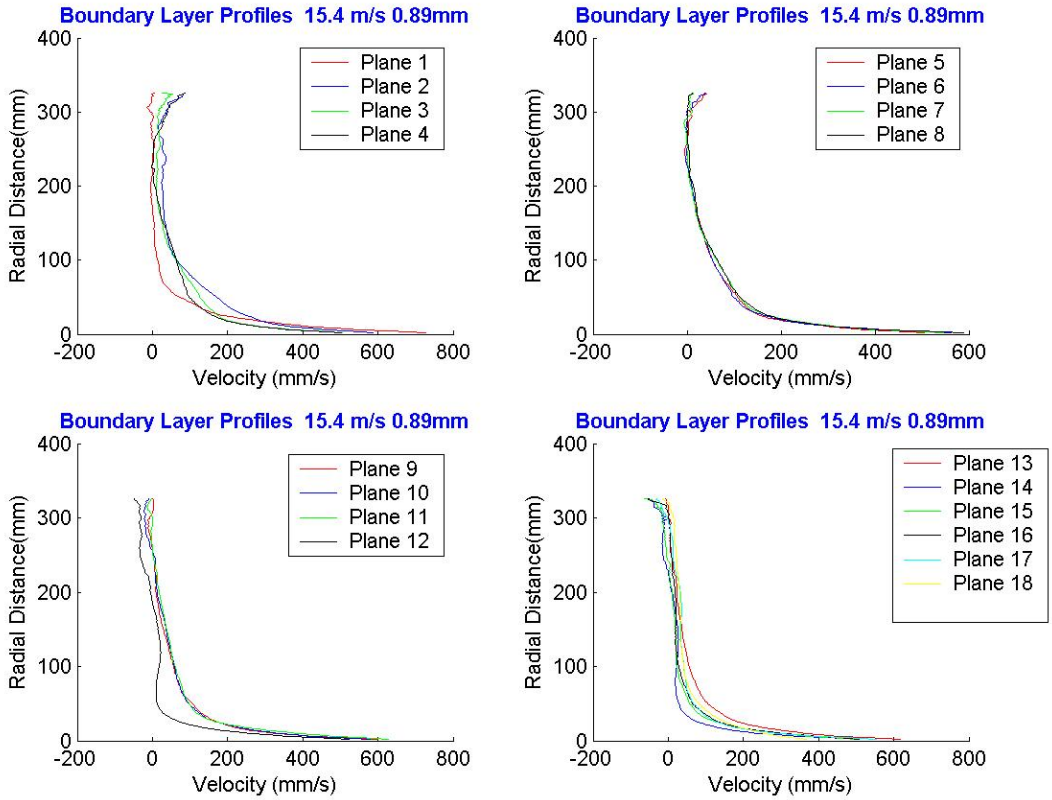
Boundary Layer Profiles 15.4 m/s 0.89mm
Radial Distance(mm)
Velocity (mm/s)
Plane 1
Plane 2
Plane 3
Plane 4
Boundary Layer Profiles 15.4 m/s 0.89mm
Radial Distance(mm)
Velocity (mm/s)
Plane 5
Plane 6
Plane 7
Plane 8
Boundary Layer Profiles 15.4 m/s 0.89mm
Radial Distance(mm)
Velocity (mm/s)
Plane 9
Plane 10
Plane 11
Plane 12
Boundary Layer Profiles 15.4 m/s 0.89mm
Radial Distance(mm)
Velocity (mm/s)
Plane 13
Plane 14
Plane 15
Plane 16
Plane 17
Plane 18

Appendix H: Fluctuating Velocity Profiles

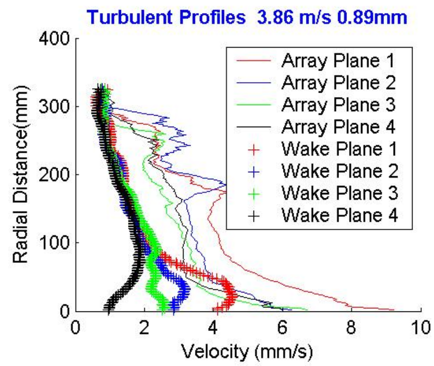

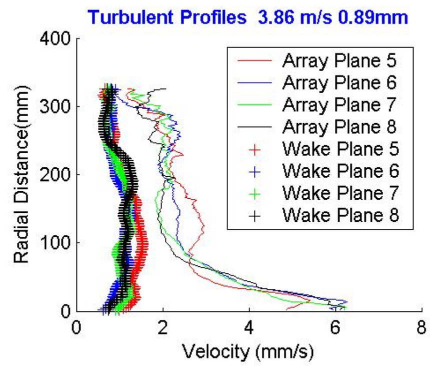

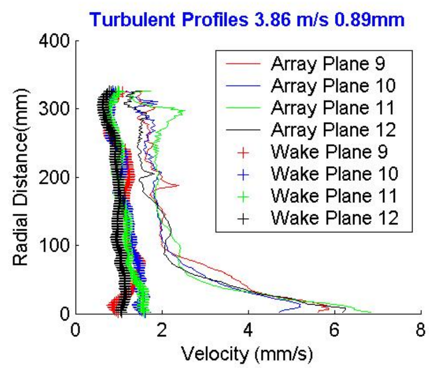

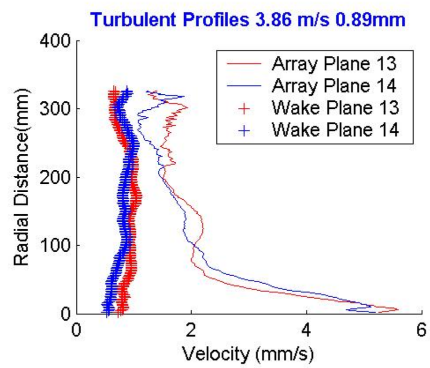

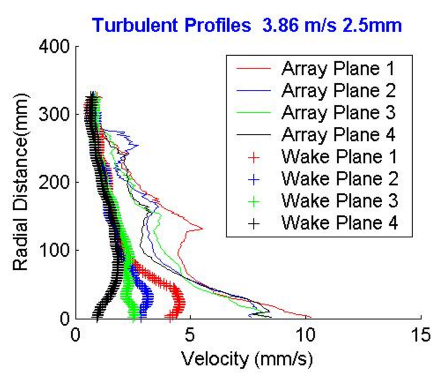

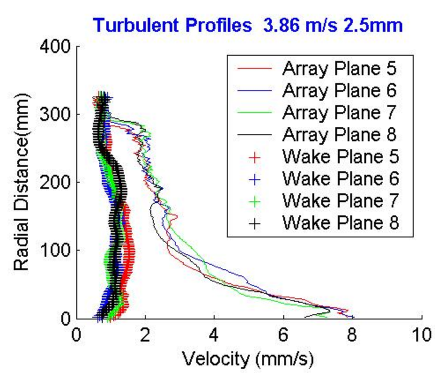

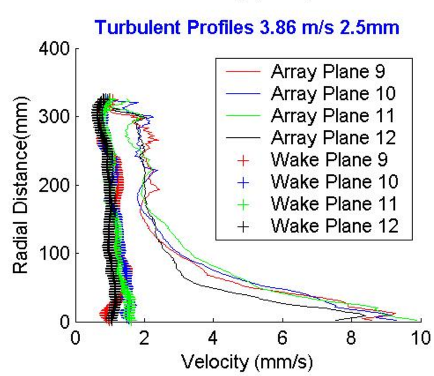

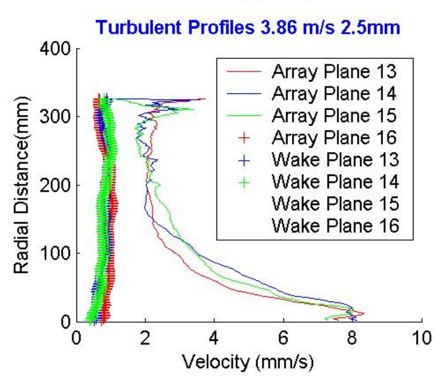

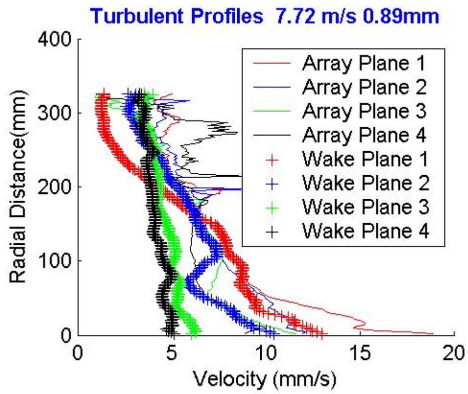
Turbulent Profiles 7.72 m/s 0.89mm
Radial Distance(mm)
Velocity (mm/s)
Array Plane 1
Array Plane 2
Array Plane 3
Array Plane 4
Wake Plane 1
Wake Plane 2
Wake Plane 3
Wake Plane 4
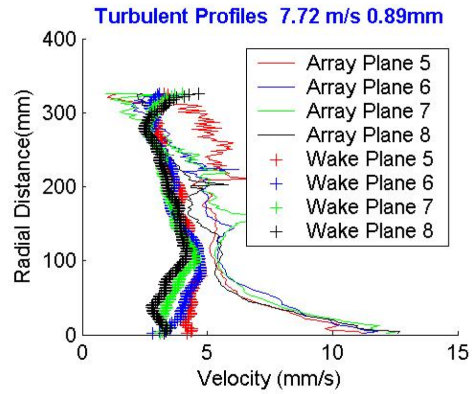
Turbulent Profiles 7.72 m/s 0.89mm
Radial Distance(mm)
Velocity (mm/s)
Array Plane 5
Array Plane 6
Array Plane 7
Array Plane 8
Wake Plane 5
Wake Plane 6
Wake Plane 7
Wake Plane 8
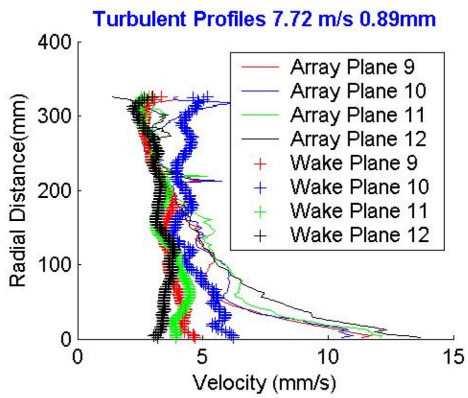
Turbulent Profiles 7.72 m/s 0.89mm
Radial Distance(mm)
Velocity (mm/s)
Array Plane 9
Array Plane 10
Array Plane 11
Array Plane 12
Wake Plane 9
Wake Plane 10
Wake Plane 11
Wake Plane 12
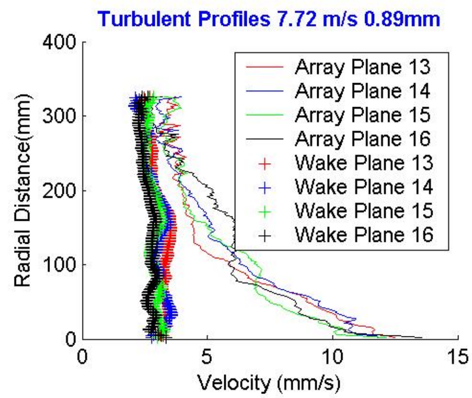
Turbulent Profiles 7.72 m/s 0.89mm
Radial Distance(mm)
Velocity (mm/s)
Array Plane 13
Array Plane 14
Array Plane 15
Array Plane 16
Wake Plane 13
Wake Plane 14
Wake Plane 15
Wake Plane 16
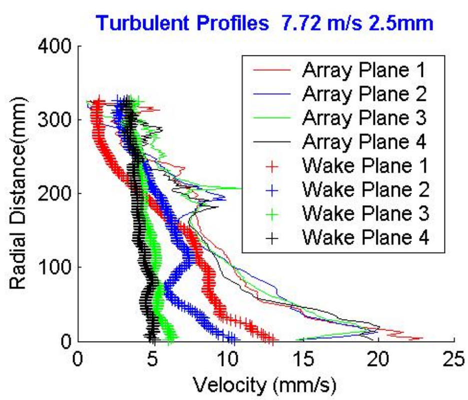
Turbulent Profiles 7.72 m/s 2.5mm
Radial Distance(mm)
Velocity (mm/s)
Array Plane 1
Array Plane 2
Array Plane 3
Array Plane 4
Wake Plane 1
Wake Plane 2
Wake Plane 3
Wake Plane 4
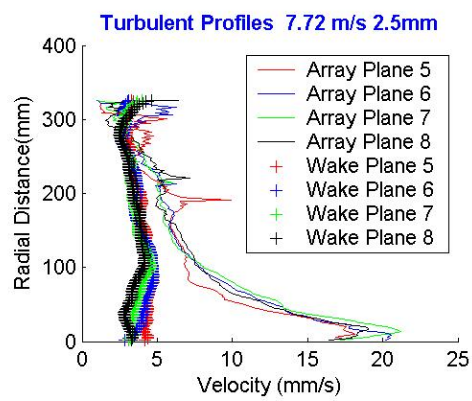
Turbulent Profiles 7.72 m/s 2.5mm
Radial Distance(mm)
Velocity (mm/s)
Array Plane 5
Array Plane 6
Array Plane 7
Array Plane 8
Wake Plane 5
Wake Plane 6
Wake Plane 7
Wake Plane 8
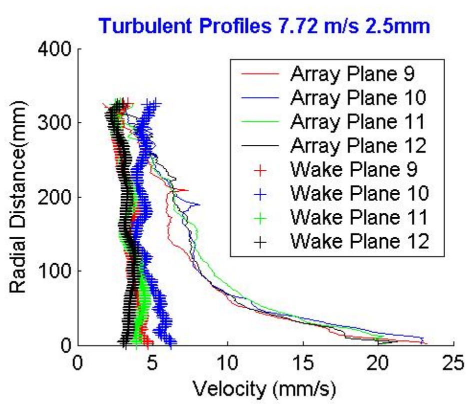
Turbulent Profiles 7.72 m/s 2.5mm
Radial Distance(mm)
Velocity (mm/s)
Array Plane 9
Array Plane 10
Array Plane 11
Array Plane 12
Wake Plane 9
Wake Plane 10
Wake Plane 11
Wake Plane 12
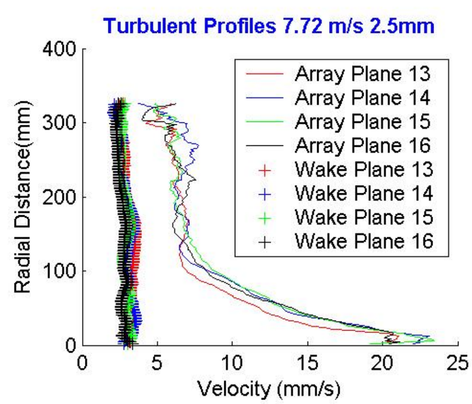
Turbulent Profiles 7.72 m/s 2.5mm
Radial Distance(mm)
Velocity (mm/s)
Array Plane 13
Array Plane 14
Array Plane 15
Array Plane 16
Wake Plane 13
Wake Plane 14
Wake Plane 15
Wake Plane 16

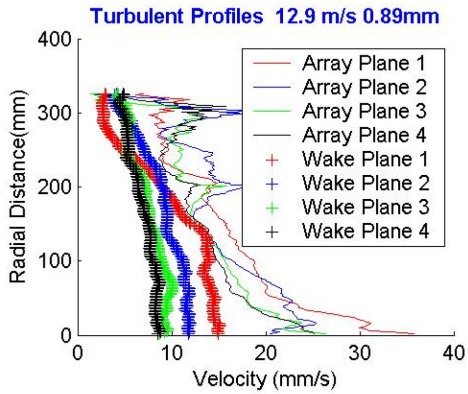
Turbulent Profiles 12.9 m/s 0.89mm
Radial Distance(mm)
Velocity (mm/s)
Array Plane 1
Array Plane 2
Array Plane 3
Array Plane 4
Wake Plane 1
Wake Plane 2
Wake Plane 3
Wake Plane 4

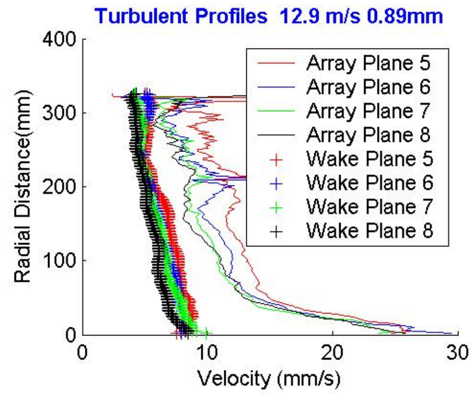
Turbulent Profiles 12.9 m/s 0.89mm
Radial Distance(mm)
Velocity (mm/s)
Array Plane 5
Array Plane 6
Array Plane 7
Array Plane 8
Wake Plane 5
Wake Plane 6
Wake Plane 7
Wake Plane 8

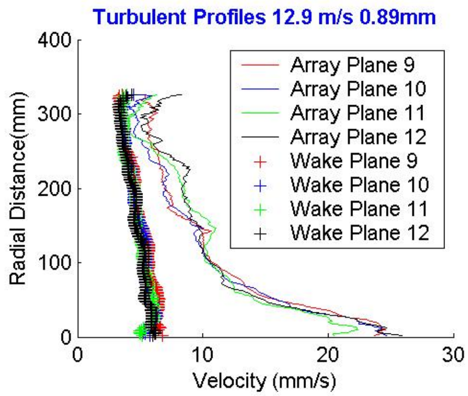
Turbulent Profiles 12.9 m/s 0.89mm
Radial Distance(mm)
Velocity (mm/s)
Array Plane 9
Array Plane 10
Array Plane 11
Array Plane 12
Wake Plane 9
Wake Plane 10
Wake Plane 11
Wake Plane 12

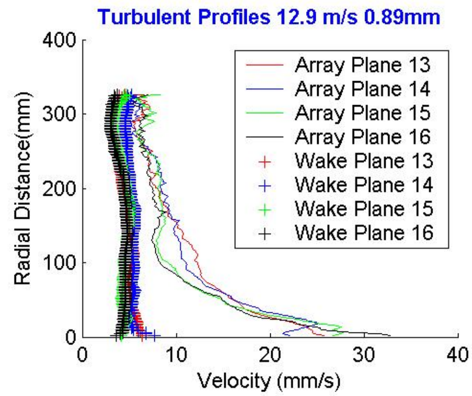
Turbulent Profiles 12.9 m/s 0.89mm
Radial Distance(mm)
Velocity (mm/s)
Array Plane 13
Array Plane 14
Array Plane 15
Array Plane 16
Wake Plane 13
Wake Plane 14
Wake Plane 15
Wake Plane 16

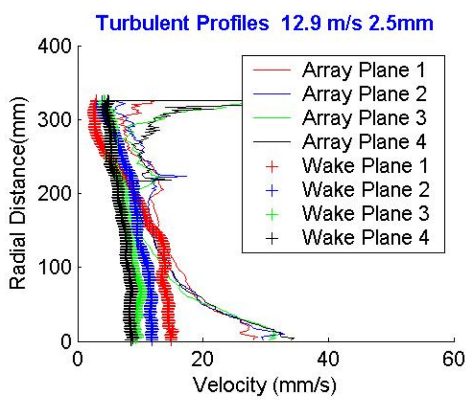
Turbulent Profiles 12.9 m/s 2.5mm
Radial Distance(mm)
Velocity (mm/s)
Array Plane 1
Array Plane 2
Array Plane 3
Array Plane 4
Wake Plane 1
Wake Plane 2
Wake Plane 3
Wake Plane 4

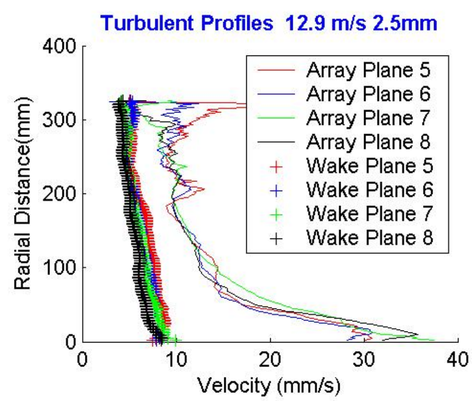
Turbulent Profiles 12.9 m/s 2.5mm
Radial Distance(mm)
Velocity (mm/s)
Array Plane 5
Array Plane 6
Array Plane 7
Array Plane 8
Wake Plane 5
Wake Plane 6
Wake Plane 7
Wake Plane 8

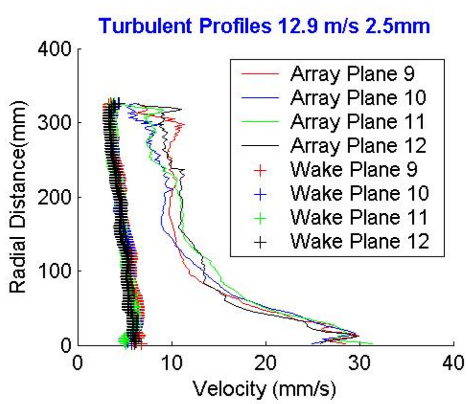
Turbulent Profiles 12.9 m/s 2.5mm
Radial Distance(mm)
Velocity (mm/s)
Array Plane 9
Array Plane 10
Array Plane 11
Array Plane 12
Wake Plane 9
Wake Plane 10
Wake Plane 11
Wake Plane 12

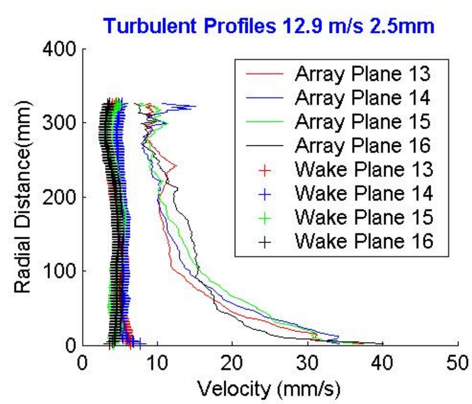
Turbulent Profiles 12.9 m/s 2.5mm
Radial Distance(mm)
Velocity (mm/s)
Array Plane 13
Array Plane 14
Array Plane 15
Array Plane 16
Wake Plane 13
Wake Plane 14
Wake Plane 15
Wake Plane 16

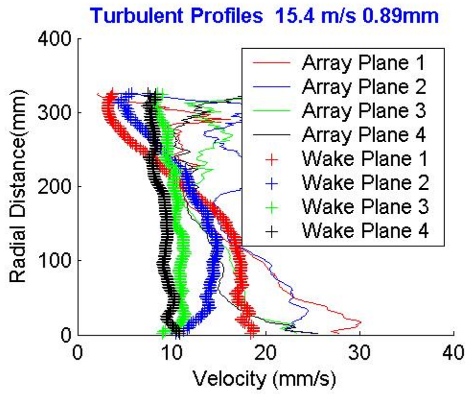
Turbulent Profiles 15.4 m/s 0.89mm
Radial Distance(mm)
Velocity (mm/s)
Array Plane 1
Array Plane 2
Array Plane 3
Array Plane 4
Wake Plane 1
Wake Plane 2
Wake Plane 3
Wake Plane 4

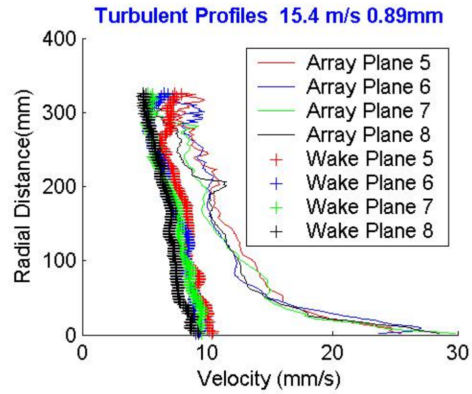
Turbulent Profiles 15.4 m/s 0.89mm
Radial Distance(mm)
Velocity (mm/s)
Array Plane 5
Array Plane 6
Array Plane 7
Array Plane 8
Wake Plane 5
Wake Plane 6
Wake Plane 7
Wake Plane 8

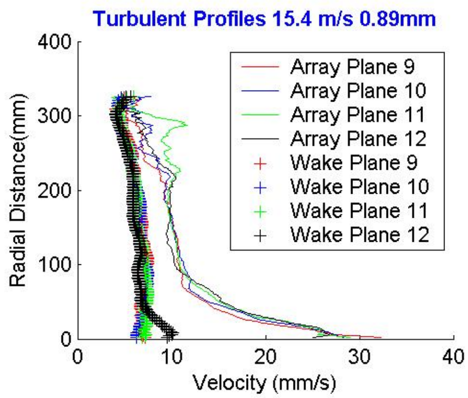
Turbulent Profiles 15.4 m/s 0.89mm
Radial Distance(mm)
Velocity (mm/s)
Array Plane 9
Array Plane 10
Array Plane 11
Array Plane 12
Wake Plane 9
Wake Plane 10
Wake Plane 11
Wake Plane 12

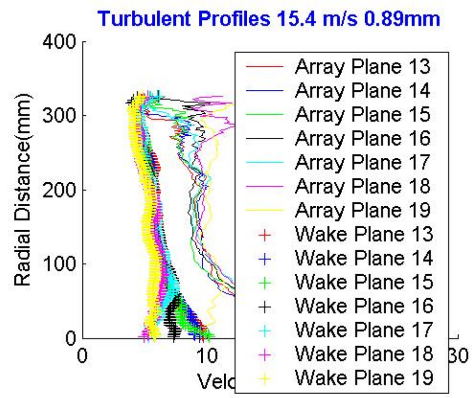
Turbulent Profiles 15.4 m/s 0.89mm
Radial Distance(mm)
Array Plane 13
Array Plane 14
Array Plane 15
Array Plane 16
Array Plane 17
Array Plane 18
Array Plane 19
Wake Plane 13
Wake Plane 14
Wake Plane 15
Wake Plane 16
Wake Plane 17
Wake Plane 18
Wake Plane 19

Appendix I: XY Position Data

XY Tracking 3.8 m/s 0.89 mm

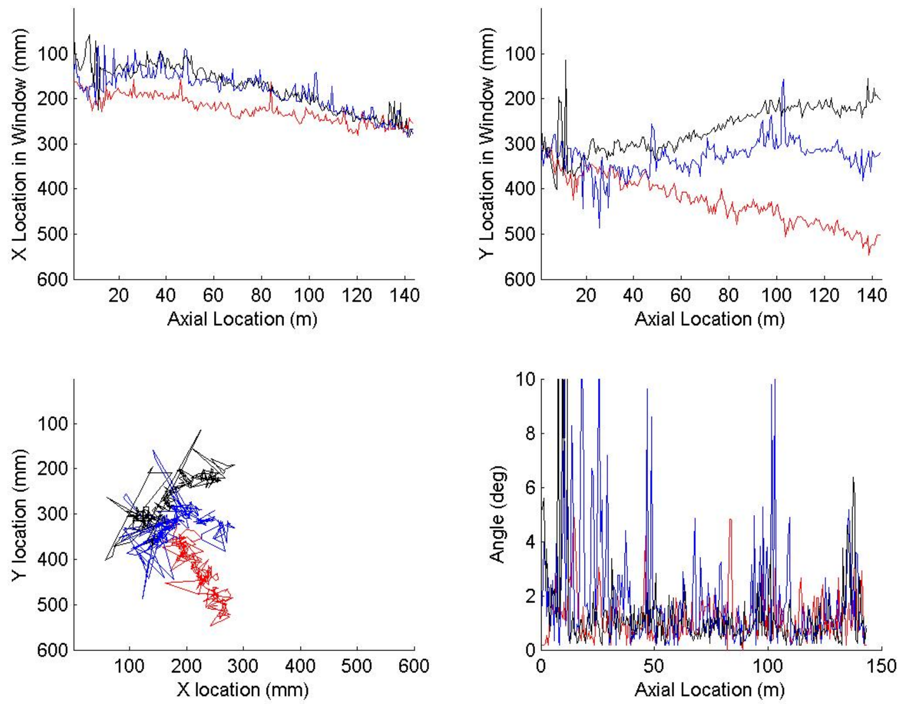

XY Tracking 3.8 m/s 2.5 mm

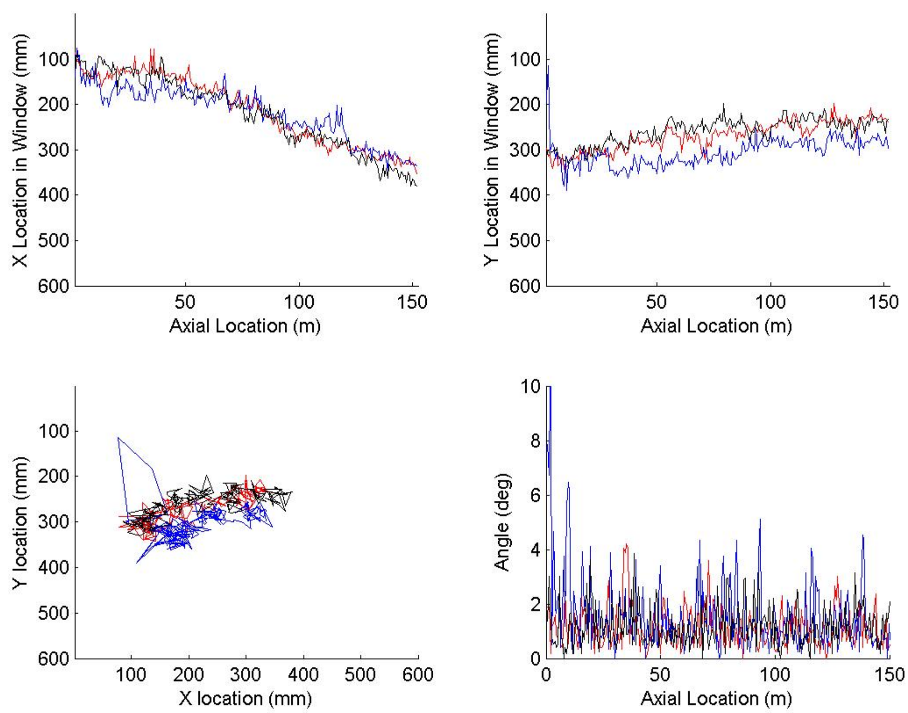

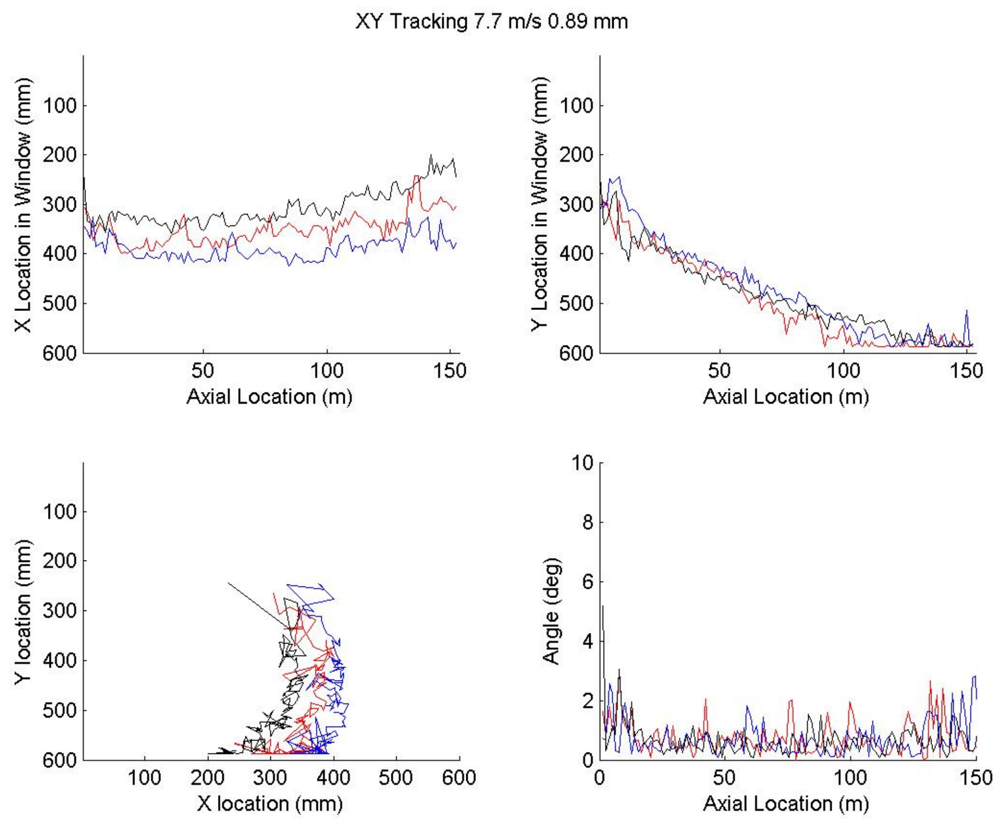
XY Tracking 7.7 m/s 0.89 mm
X Location in Window (mm)
Axial Location (m)
Y Location in Window (mm)
Axial Location (m)
Y location (mm)
X location (mm)
Angle (deg)
Axial Location (m)

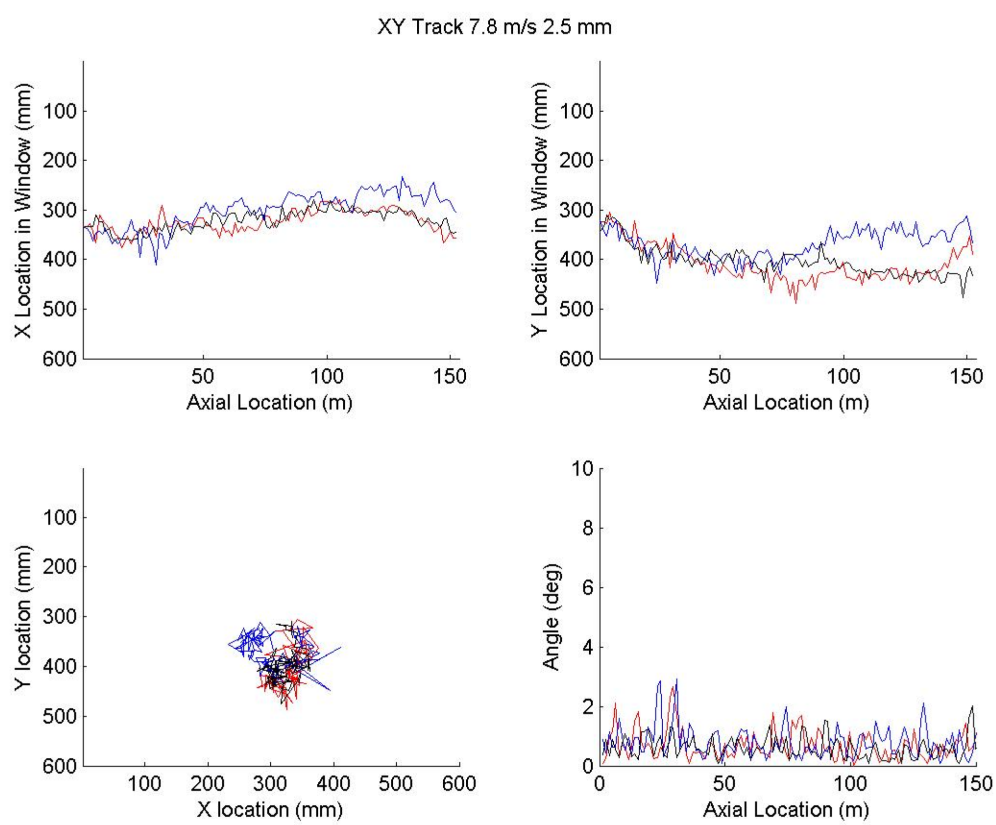
XY Track 7.8 m/s 2.5 mm
X Location in Window (mm)
Axial Location (m)
Y Location in Window (mm)
Axial Location (m)
Y location (mm)
X location (mm)
Angle (deg)
Axial Location (m)

XY Track 12.8 m/s 0.89 mm

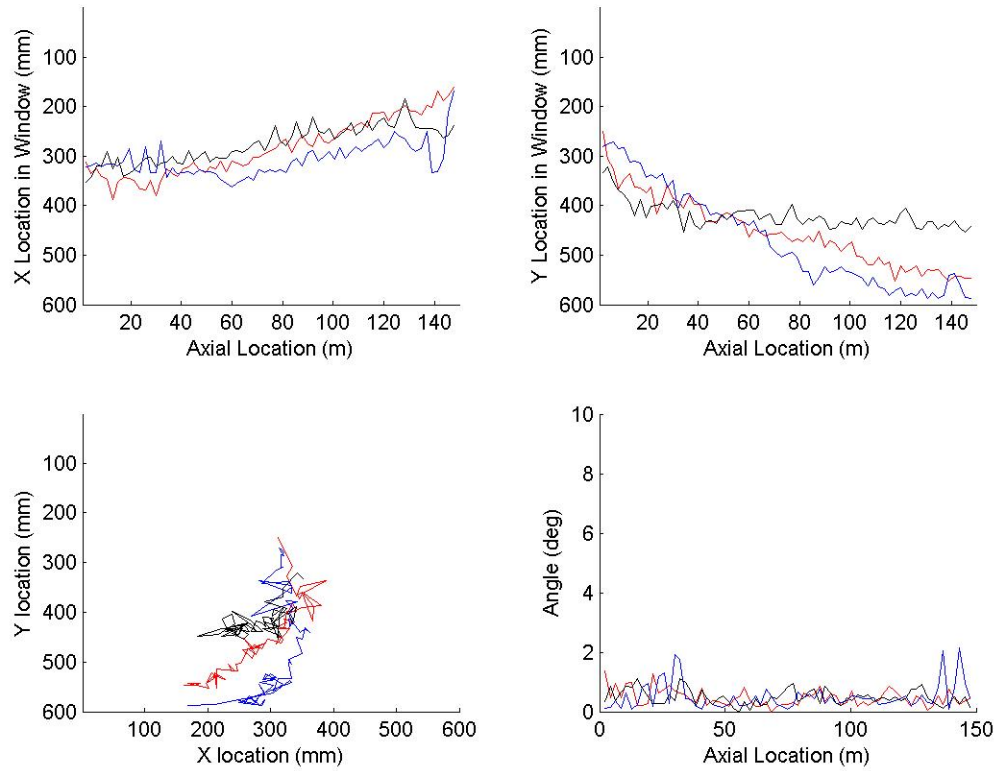

XY Tracking 12.8 m/s 2.5 mm

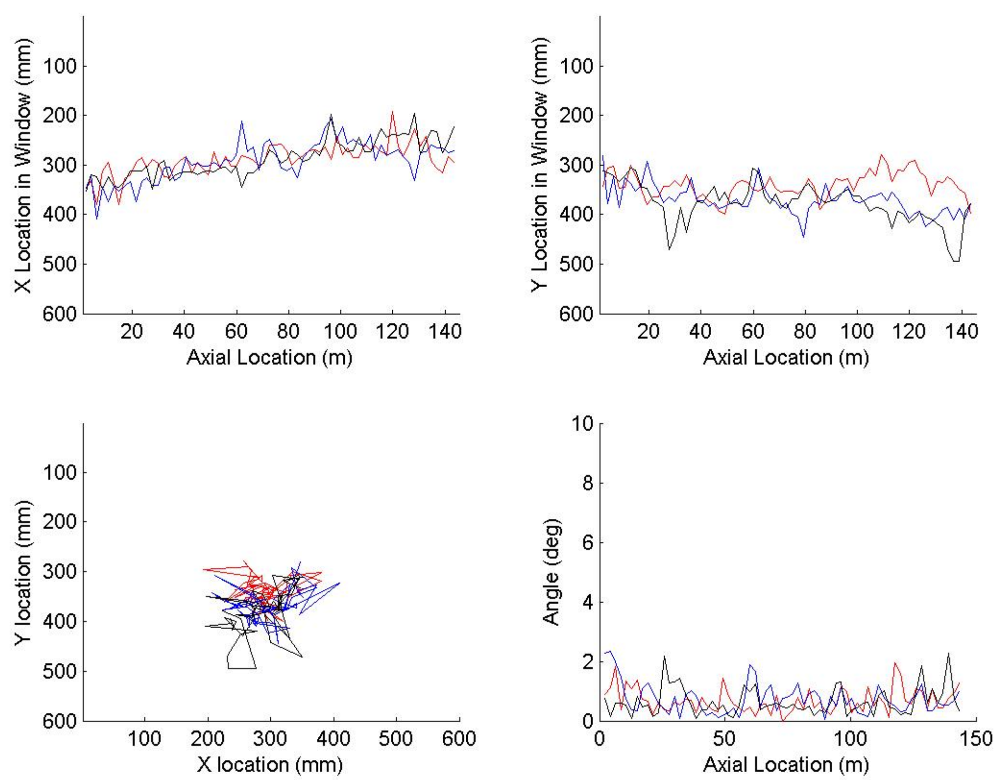

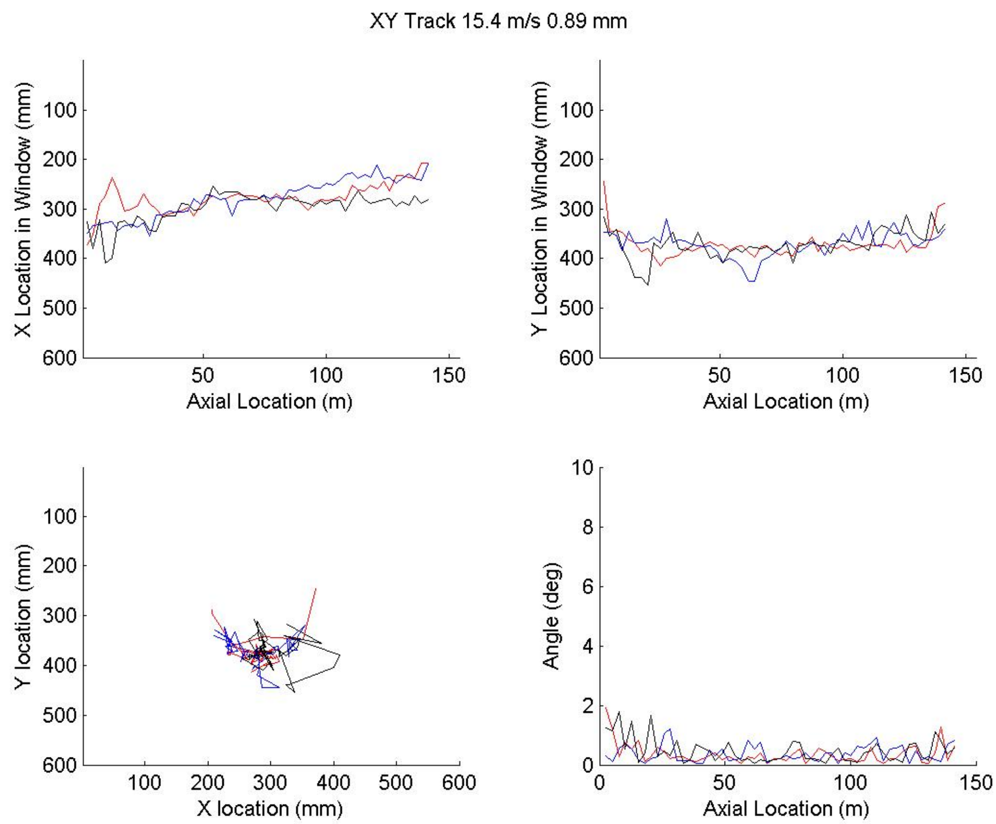
XY Track 15.4 m/s 0.89 mm
X Location in Window (mm)
Axial Location (m)
Y Location in Window (mm)
Axial Location (m)
Y location (mm)
X location (mm)
Angle (deg)
Axial Location (m)

Appendix J: Uncertainty and Convergence

Uncertainty in the measurements are due to both systematic errors and precision errors. A detailed uncertainty analysis for this SPIV system can be found in "   ", Atsavapranee et. al. Here, a brief discussion and analysis will be presented for this experimental set up.

The total uncertainty in the velocity measurements is the Euclidean norm of the sum of the system bias errors, B, and the measurement precision limit, P.

$$U = \sqrt{B^2 + P^2}$$

Equation 48

The bias limit for this experiment is determined by the inaccuracies inherent in the system, i.e. errors in the curve fitting for the data analysis, camera alignment errors (calibration grid and camera setting), timing errors, and positioning errors. As an estimate, the pixel displacements calculated on an image where the velocity of the flow is zero will be used as an estimate of the SPIV system bias errors.

For every run of SPIV data collected, the initial data image is sufficiently upstream of the towing strut that there is no disturbance of the flow. This data image was evaluated and the mean axial velocity calculated as an estimate of the system bias error. Because the flow was not completely at rest due to the agitation of the control volume, the standard deviation was not selected as the indicator of the bias error. However, the mean value would indicate a directional bias for the overall measurement since the settling flow can be considered random.

The mean value was evaluated for images taken for each speed condition and Δt. For the 3.7 m/s, 7.7 m/s, 12.8 m/s, and 15.4 m/s, the nominal pixel displacement was 0.015 to 0.04 with standard deviations on the order of 0.02 to 0.04. For a few of the cases, the average was larger (0.1), but this occurred where the time between runs was short compared to the majority of the other runs. The consistency in the mean pixel displacement for the zero velocity case (approximately 0.025 pixels) for all Δt values (different speeds) justifies using this value as a reasonable systematic bias.

The precision limit is the error associated with an averaged measurement due to limited sampling of that value. The precision limit, P, is evaluated using the standard deviation in a measurement evaluated at a given point and the number of samples at that point. The precision limit is calculated using Equation 49 where t is the coverage factor. For cases where $N>9$, t takes on the value 2.

$$P = \frac{t\,\sigma}{\sqrt{N}}$$

Equation 49

The precision limit for this experiment will be estimated from the tare data. Each image is considered to be an independent sample as is each measurement occurring within that image. The averaged velocity fields were determined by averaging together approximately 40 images per averaged plane. However, since the profile data is azimuthally averaged, the total number of samples at each radial location changes with distance from the center. Therefore, averaged plane 1 is being analyzed for all speeds at three locations in the flow, 5-mm, 60-mm and 120- mm from the center of the measurement field. The number of samples in a single image at each of these radial locations is 16, 168, and 336 respectively. Therefore, the total number of samples at each location when averaging all 40 images is effectively 40*16, 40*168, and 40*336, or 640, 6720, and 13440. As an estimate, the standard deviation at each location will be determined from the 40 images. These values will be taken to be the representative standard deviation quantity used in the precision limit. The precision limit is calculated at the inner most location (5-mm) for a sample size of 40 images and at the chosen radial locations using the effective sample size created by azimuthally averaging over the images. The results are shown in Table 17 .

Table 17: Precision limits for the SPIV data. The precision limits are calculated for several radial locations across the field of view.

Speed m/s (kts)	Standard Deviation (pixels)			Precision Error N=40	Precision Error (total N)		
	5-mm	60-mm	120-mm	5-mm	5-mm	60-mm	120-mm
3.7(7.5)	0.21	0.15	0.08	0.066	0.017	0.004	0.002
7.7(15)	0.25	0.2	0.18	0.079	0.02	0.005	0.003
12.8(25)	0.17	0.18	0.19	0.054	0.014	0.005	0.003
15.4(30)	0.2	0.22	0.18	0.063	0.016	0.005	0.003

The results indicate that for the initial 40 images, the precision error is below 0.08 pixel. For the azimuthally averaged data, the precision error is significantly reduced due to the large number of samples. Using the largest value as the worst case estimate for the precision error, the overall uncertainty in the measurement is estimated to be:

$$U = \sqrt{B^2 + P^2} = \sqrt{0.025^2 + 0.08^2} = 0.084\, pixel$$

Equation 50

This value is in close agreement with the estimate used by Ganapathisubramani, et. al. in a 3-D SPIV set up using cameras pointing with a 30 deg angle relative to the normal to the light sheet. The data reduction method also used a Gaussian peak finding algorithm as does Davis. For their experiment they evaluated a uncertainty of 0.1 pixels in the high speed region of their flow with increasing uncertainties where seeding became less uniform and the shear became very high (0.6 pixels). For the current experiment, the entire measured flow field is low shear since the measurements occur outside the high shear region of the boundary layer. Therefore, the estimate for the uncertainty can be considered to be less than 0.1 pixel for all conditions.

The convergence of the average and turbulence data were analyzed for select conditions to evaluate the confidence level of the measurements. For the average profiles, this procedure was conducted during the azimuthal averaging process, not during the initial averaging. Each radial location has a different number of samples to be averaged together and therefore, the convergence changed with radius. The convergence ratio is evaluated by taking the ratio of the change in the average divided by the average,

$$R_i = \frac{(\overline{u_i} - \overline{u_{i-1}})}{\overline{u_i}}$$

Equation 51

The convergence ratio for the 2nd measurement location, the 25th measurement location and the 50th measurement location (r=5 mm, 60 mm, 120 mm) for selected averaged image planes are plotted against the number of samples being used in the average in Figure 51.

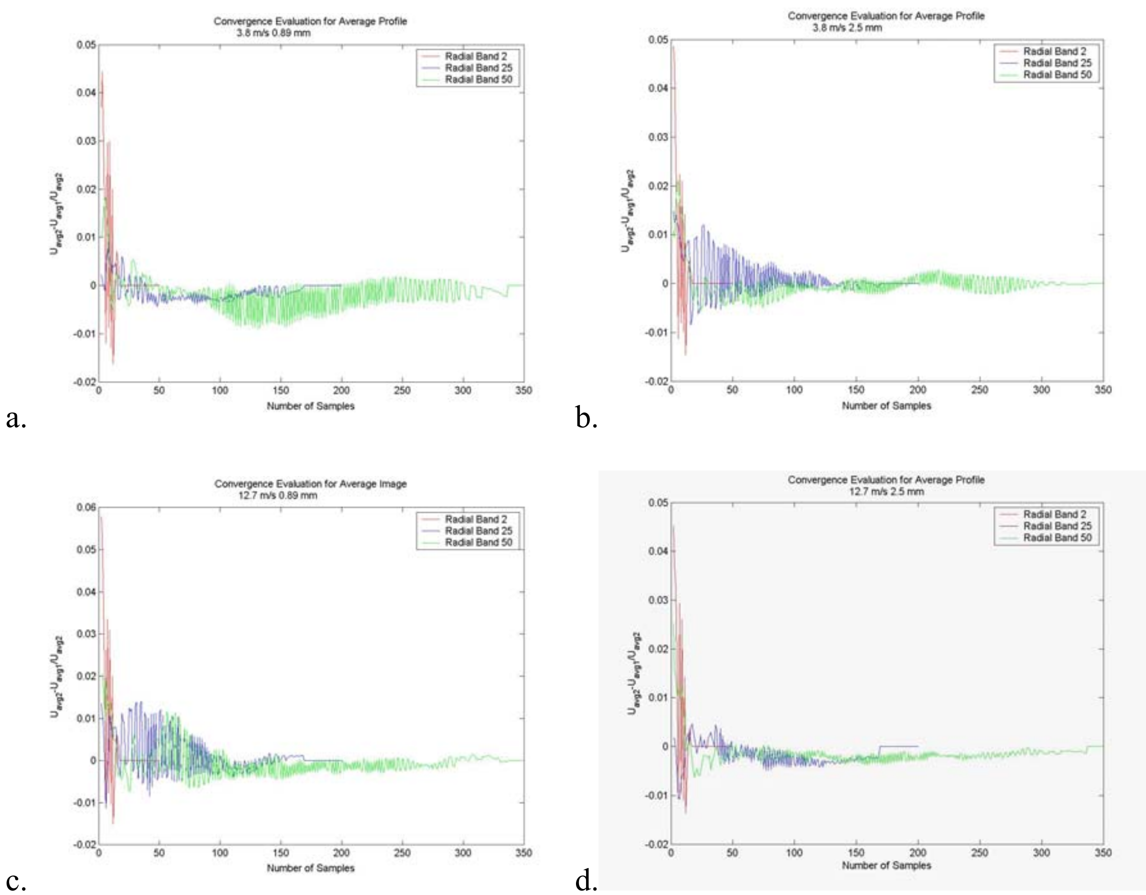

Figure 51: Convergence for Averaged Profiles. The convergence for all radial locations reached values with 0.01 of the final average. The outer locations had better convergence ratios than the inner locations. a. U=3.8 m/s d=0.89-mm, b. U=3.8 m/s d=2.5-mm, c. U=12.7 m/s d=0.89-mm, d. U=12.7 m/s d=2.5-mm.

The turbulence convergence study was required to be done in a two step process. Initial converge evaluation was done during the initial evaluation of the RMS values within the turbulence images evaluated at each plane location. Then, using the turbulence images established from RMS evaluation, a radial convergence was done similar to above. The convergence ratio, Ri, is plotted against the number of samples for the U=3.8 m/s and d=0.89-mm in Figure 52. The convergence ratio value is calculated at points 5 mm, 60 mm and 120 mm away from the filament.

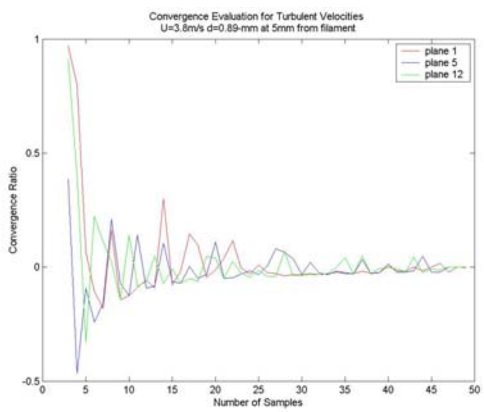

a.

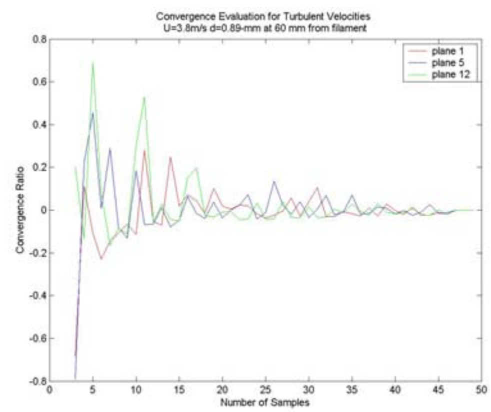

b

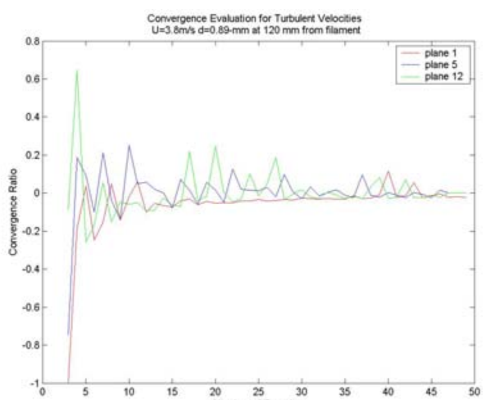

c.

Figure 52: Convergence ratios for turbulence data. The convergence ratios were evaluated at select points 2mm, 60 mm and 120 mm away from the filament for U=7.5 m/s and d=0.89-mm. The final convergence values at each location were below 0.05 for all locations and below 0.02 for most locations.

The convergence ratios at each location reached values below 0.05 for all locations and to below 0.02 for most locations after averaging the individual values from each image.

There were 49 images at each location. After the turbulence image was evaluated, the turbulence values were azimuthally averaged to establish an average fluctuation quantity at each radial location. The convergence ratios for the azimuthal averaging are shown in Figure 53.

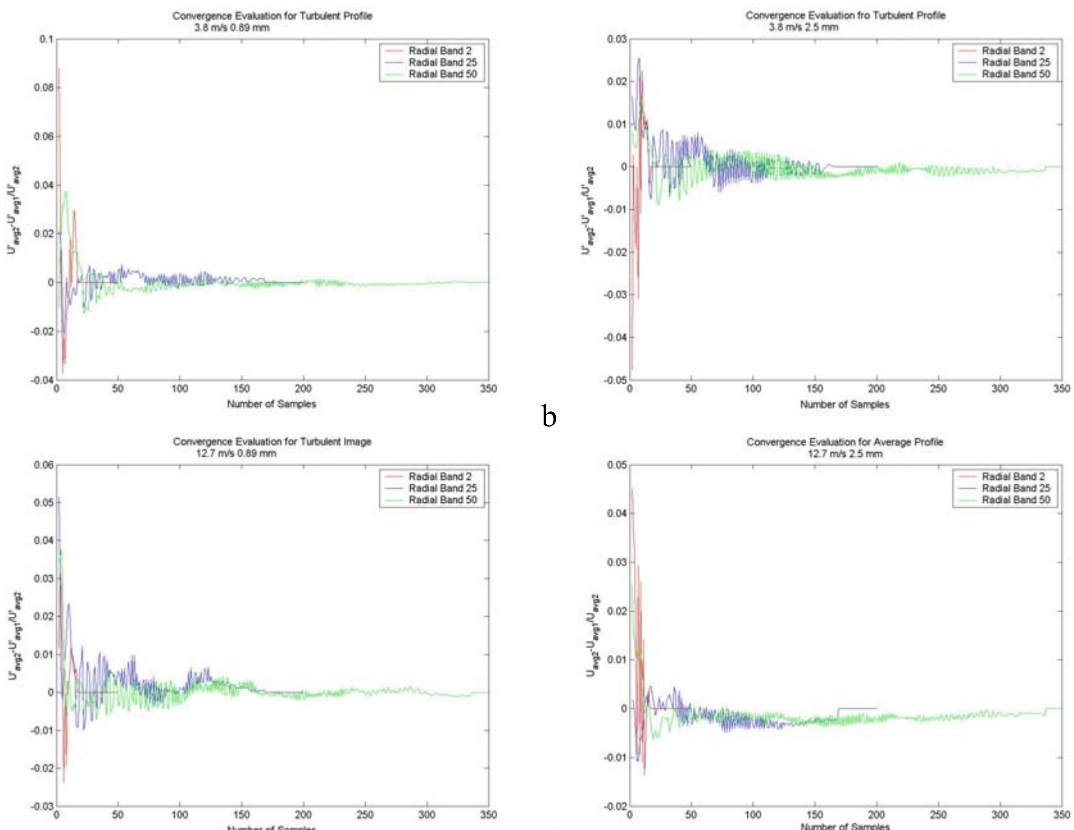

a. b c. d

Figure 53: Convergence ratio for the turbulence images. The convergence for all radial locations reached values with 0.01 of the final average. The outer locations had better convergence ratios than the inner locations. a. U=3.8 m/s d=0.89-mm, b. U=3.8 m/s d=2.5-mm, c. U=12.7 m/s d=0.89-mm, d. U=12.7 m/s d=2.5-mm.

NUWCDIVNPT 01EDD 14018828751 10/18/05 08:00P P.001

Deborah Furey
Marine and Aviation Dept.
9500 MacArthur Blvd
West Bethesda, Maryland 20817

Naval Undersea Warfare Center
1176 Howell Street
Newport, Rhode Island 02841

Public Affairs Office:
I writing to you to request permission to reprint the following material from the publication entitled:

Lueptow, R., "Turbuent Boundary Layer on a Cylinder in Axial Flow", NUSC Technical Report 8389, Sept. 1988

1. Figure 2: Representative Velocity Defect Profiles showing he Influence of Transverse Curvature (Page 28).
2. Figure 3: Representative velocity Profiles in Wall Coordinates Showing the Influence of Transverse Curvature (Page 29).

I have enclosed a copy of the material for your convenience.

This material will be reprinted in my dissertation, entitled "The Turbulent Boundary Layer on a Small Diameter Flexible Cylinder in the Wake of a Streamlined Towing Apparatus" which I anticipate will be published December 2005.

If you have any questions or would like to reach me, my phone and FAX numbers are below.

Sincerely,

Deborah Furey
Mechanical Engineering Department
University of Maryland
Phone: (301)227-5410
FAX: (301)227-4615

Permission to Reprint the above-referenced material granted by:
Name/Title: David Sanders, Public Affairs Officer, NUWC Div Npt
Conditions: For use in your dissertation, as outlined above.

Signature:

Deborah Furey
Marine and Aviation Dept.
9500 MacArthur Blvd
West Bethesda, Maryland 20817

Alice Essenpreis
Rights Sales, Acquisitions, and Permissions
Springer-Verlag, GmbH
Rights and Permissions
Tiergartenstr. 17
69121 Heidelberg
Germany

Ms. Essenpreis:

I am writing to you to request permission to reprint the following material from the publication entitled:

Cipolla, K. and Keith, W., "High Reynolds number thick axisymmetric turbulent boundary layer measurements", Experiments in Fluids, Experimental Methods and their Applications to Fluid Flow, copyright Springer-Verlag 2003, 10.1007/s00348-003-0706-x.

Item to reprint:
Figure. 6 Momentum thickness measurements for the 0.89 mm diameter cylinder at discrete locations

I have enclosed a copy of the material for your convenience.

This material will be reprinted in my dissertation, entitled "The Turbulent Boundary Layer on a Small Diameter Flexible Cylinder in the Wake of a Streamlined Towing Apparatus" which I anticipate will be published December 2005 through the University of Maryland. I expect on the order of 10-20 copies to be printed.

If you have any questions or would like to reach me, my phone and FAX numbers are below.

Sincerely,

Deborah Furey,
Email: deborah.furey@navy.mil
Mechanical Engineering Department
University of Maryland
Phone: (301)227-5410
FAX: (301)227-4615

Permission to Reprint the above-referenced material granted by:
Name/Title:
Conditions:

Signature:

From: Essenpreis, Alice, Springer DE <Alice.Essenpreis@springer.com>

To: fureyda@gmail.com
Date: Oct 31, 2005 8:35 AM
Subject: WG: Requesting permission for reprinting material
Reply | Reply to all | Forward | Print | Add sender to Contacts list | Trash this message |
Report phishing | Show original | Message text garbled?
Dear Ms. Furey,

With reference to your request (copy herewith) to re-use material
on which Springer controls the copyright, our permission is granted free of charge,
on the following conditions:
* it concerns original material which does not carry references to other sources,
* if material in question appears with credit to another source, authorization
from and reference to that source is required as well, and
permission is also obtained from the author (address is given on the imprint page or with the article);
* allows you non-exclusive reproduction rights throughout the world,
* permission includes use in an electronic form, on the condition that content is
- password protected,
- at Intranet or
- in CD-ROM/E-book;
* full credit (book/journal title, volume, year of publication, page,
chapter/article title, name(s) of author(s), figure number(s), original copyright notice)
is given to the publication in which the material was originally published by adding:
With kind permission of Springer Science and Business Media.
Permission free of charge does not prejudice any rights we might have
to charge for reproduction of our copyrighted material in the future.

With best regards,

_

Alice Essenpreis
Springer
Rights and Permissions

_
Tiergartenstrasse 17 | 69121 Heidelberg GERMANY
FAX: +49 6221 487 8223
Alice.Essenpreis@springer.com
www.springeronline.com/rights

Deborah Furey
Marine and Aviation Dept.
9500 MacArthur Blvd
West Bethesda, Maryland 20817

Beth Darchi
Copyrights and Permissions
Journal of Fluids Engineering
ASME
Three Park Avenue
New York, New York 10016

Ms. Darchi

I request permission to reprint the following material from the publication entitled:

Keith, W., Hurdis, D, and Abraham, B., "A Comparison of Turbulent Boundary Layer Wall-Pressure Spectra", Journal of Fluids Engineering, September 1992, Vol 114, pp. 338-347.

Figure 3: Nondimensional wall pressure spectra scaled on mixed variables (Page 343).

I have enclosed a copy of the material for your convenience.

This material will be reprinted in my dissertation, entitled "The Turbulent Boundary Layer on a Small Diameter Flexible Cylinder in the Wake of a Streamlined Towing Apparatus" which I anticipate will be published December 2005.

If you have any questions or would like to reach me, my phone and FAX numbers are below.

Sincerely,

Deborah Furey
Mechanical Engineering Department
University of Maryland
Phone: (301)227-5410
FAX: (301)227-4615

Permission to Reprint the above-referenced material granted by:
Name/Title:
Conditions:

Signature:

-----Original Message-----
From: Beth Darchi [mailto:DarchiB@asme.org]
Sent: Wednesday, November 09, 2005 12:36
To: Furey, Deborah A CIV NSWCCD W. Bethesda, 5300
Cc: Philip DiVietro; Gina Faller
Subject: RE: request permission to reprint graphic from an article

Dear Ms. Furey,
It is our pleasure to grant you permission to publish the ASME Figure 3 from "A Comparison of Turbulent Boundary Layer Wall-Pressure Spectra", by Keith, W., Hurdis, D, and Abraham, B., Journal of Fluids Engineering, September 1992, Vol 114, pp. 338-347, cited in your letter for inclusion in your dissertation titled "The Turbulent Boundary Layer on a Small Diameter Flexible Cylinder in the Wake of a Streamlined Towing Apparatus" submitted to the University of Maryland, December 2005. As is customary, we request that you ensure proper acknowledgment of the exact sources of this material, the authors, and ASME as original publisher.

In accordance with ASME policy, this permission is contingent upon payment of a royalty fee of US$20 for 1 figure ($20.00 for the first figure/table, $10 thereafter). This is solely charged to non-authors of the requested works. We accept payments on all major credit cards such as: Visa, MasterCard, American Express, Discover, and Diners Club, or by check payable to ASME. Please send payment to the attention Gina Faller, ASME Accounting, 22 Law Drive, Fairfield, NJ 07007, and indicate A/C# 1-1150-0000-4303. Should you have any questions regarding payment form or transfer, please contact Ms. Faller; P: 973-244-2267, F: 973-882-4924; E:fallerg@asme.org.

Thank you for your interest in ASME publications.
Sincerely,
Beth Darchi
Copyrights & Permissions
ASME International
Three Park Avenue
New York, NY 10016
P: 212-591-7700
F: 212-591-7292
E: darchib@asme.org

REFERENCES

1. Rao, G., “The Law of the Wall in a Thick Axisymmetric Turbulent Boundary Layer”, Journal of Applied Mechanics, March 1967, pp.237-238
2. Patel, V.C., “A Unified View of the Law of the Wall Using Mixing Length Theory”, Aero Quarterly, 1970, Vol 24, pp. 55-70.
3. Rao, G. and Keshavan, N., “Axisymmetric Turbulent Boundary Layers in Zero Pressure Gradient Flows”, Journal of Applied Mechanics, March 1972, pp. 25-32.
4. Afzal, N. and Singh, K, “Measurements in an Axisymmetric Turbulent Boundary Layer Along a Circular Cylinder”, Aero Quarterly, 1976, vol 27, pp. 217-228
5. Willmarth, W.W., Winkel, R.E., Sharma, L.K. and Bogar, T.J., “Axially Symmetric Turbulent Boundary Layers on Cylinders: Mean Velocity Profiles and Wall Pressure Fluctuations,” *J. Fluid Mech.*, Vol. 76, part 1, 1976, pp. 35-64.
6. Willmarth, W., Sharma, Lalit, and Inglis, S., “ The Effect of Cross Flow and Isolated Roughness Elements on the Boudnary Layer and Wall Pressure Fluctuations on Circular Cylinders”, University of Michigan, Department of Aerospace Engineering, Gas Dynamics Laboratories, Jan. 1977
7. Denli, N. and Landweber, L., “Thick Axisymmetric Turbulent Boundary Layer on a Circular Cylinder”, Journal Hydronautics, Vol 13, No. 3, Article No. 79-4108, pp. 92-104.
8. Ackroyd, J.A.D., “On the Analysis of Turbulent Boundary Layers on Slender Cylinders,” *J. Fluids Eng.*, Vol. 104, 1982, pp. 185-190.

9. Wei, T., “Static Pressure Distribution on Long Cylinders as a function of Angle of Yaw and Reynolds Number”, Department of Aerospace Engineering, University of Michigan, July 1983.
10. Luxton, R.E., Bull, M.K., Rajagopalan, S., “The Thick Turbulent Boundary Layer on a Long Fine Cylinder in Axial Flow”, Aeronautical Journal, Volume 88, May 1984, p. 186-199.
11. Lueptow, R., Leehey, P., and Stellinger, T., “The Thick , Turbulent Boundary layer on a Cylinder: Mean and Fluctuating Velocities”, Physics of Fluids 28 (12), December 1985, pp. 3495-3505.
12. Lueptow, R., “Turbuent Boundary Layer on a Cylinder in Axial Flow”, NUSC Technical Report 8389, Sept. 1988.
13. Neves, J.C., Moin, P., and Moser, R.D., “Effects of Convex Transverse Curvature on Wall-Bounded Turbulence. Part 1. The velocity and Vorticity,” *J. Fluid Mech.*, Vol. 272, 1994, pp. 349-381.
14. Youssef, F., Kassab, S., and Al-Fahed, S., “Low Reynolds Number Axisymmetric Turbulent Boundary Layer on a Cylinder”, Mechanics Research Communications, Vol. 25, No. 1, 1998, pp. 33-48.
15. Piquet, J. and Patel, V.C., “Transverse Curvature Effects in Turbulent Boundary Layer’, Progress in Aerospace Sciences 35 (1999) 661-672.
16. Cipolla, K, Keith, W. and Abraham, B., “Axisymmetric Turbulent Boundary Layer Measurements on Long, Thin Lines Towed at Moderate Reynolds Numbers”, NUWC-NPT Technical Report 11,273, March 2001.

17. Cipolla, K., and Keith, W., "Momentum Thickness Measurements for Thick Axisymmetric Turbulent Boundary Layers," American Society of Mechanical Engineers Fluids Engineering Summer Meeting, 14-18 July, 2002, Montreal, Canada.
18. Cipolla, K., "Direct Measurments of Wall Shear Stress on Small Diameter Towed Arrays", NUWC Program Element 0601152N, September 2002.
19. Soloff, S.M, Adrian, R.J, and Liu, Z. C., "Distortion Compensation for Generalized Stereoscopic Particle Image Velocimetry", http://ltch.tam.uiuc.edu/Research/Soloff/Calibraton/index.html
20. "Stereoscopic Digital Particle Image Velocimetry", von Karmon Institute for Fluid Dynamics, http://www.vki.ac.be/research/themes/mt/stereo.html
21. Tennekes and Lumley, "A First Course in Turbulence", MIT Press, Cambridge, Massachusetts, 1972.
22. Schlichting, H., Boundary Layer Theory, McGraw Hill Book Company, New York, 1979.
23. Bernard, P. and Wallace, J., Turbulent Flow, Analysis, Measurement and Prediction, John Wiley and Sons, Hoboken, New Jersey, 2002.
24. Hoerner, Fluid Dynamic Drag, Hoerner Fluid Dynamics, June 1993.
25. M.J. Lighthill, "On Displacement Thickness", Journal of Fluid Mechanics, Vol. 3 pp 383 – 392.
26. Farabee, T.M. and Casarella, M.J., "Spectral features of wall pressure fluctuations beneath turbulent boundary layers", Physics of Fluids, Volume 3, No. 10, October 1991, pp. 2410-2420.

27. Keith, W., Hurdis, D., and Abraham, B., "Comparison of Turbulent Boundary Layer Wall-Pressure Spectra", Transactions of the ASME, September 1992, Vol. 114, p. 338-347.
28. Farabee, T.M, "An Experimental Investigation of Wall Pressure Fluctuations Beneath Non-Equilibrium Turbulent Flows", DTNSRDC-86/047, May 1986.
29. Prasad, A.K., "Particle Image Velocimetry", Current Science, Vol. 79, No1, 10 July 2000.
30. Snarski, S., "Wall Pressure Field of Transitional Boundary Layer", NUWC Award Number: N0001401WX20459.
31. Cipolla, K. and Keith, W., "Momentum Thickness Measurements for Thick Axisymmetric Turbulent Boundary Layers", Journal of Fluids Engineering, Vol. 125, pp. 569-575, May 2003.
32. Chevray, R., "The Turbulent Wake of a Body of Revolution", Journal of Basic Engineering, Transactions of ASME, June 1968, p. 275-284.
33. Irvine, M., "Towing Tank Tests for Surface Combatant for Free Roll Decay and Coupled Pitch and Heave Motions", PhD Dissertation, University of Iowa, Iowa City, December 2004.
34. Keith, W., Cipolla, K., Hart, D. and Furey, D., "Drag Measurements on Long Thin Cylinders at Small Angles and High Reynolds Numbers", Experiments in Fluids, 2005. Vol. 38, pages. 759-769.